



저작자표시-비영리-변경금지 2.0 대한민국

이용자는 아래의 조건을 따르는 경우에 한하여 자유롭게

- 이 저작물을 복제, 배포, 전송, 전시, 공연 및 방송할 수 있습니다.

다음과 같은 조건을 따라야 합니다:



저작자표시. 귀하는 원저작자를 표시하여야 합니다.



비영리. 귀하는 이 저작물을 영리 목적으로 이용할 수 없습니다.



변경금지. 귀하는 이 저작물을 개작, 변형 또는 가공할 수 없습니다.

- 귀하는, 이 저작물의 재이용이나 배포의 경우, 이 저작물에 적용된 이용허락조건을 명확하게 나타내어야 합니다.
- 저작권자로부터 별도의 허가를 받으면 이러한 조건들은 적용되지 않습니다.

저작권법에 따른 이용자의 권리는 위의 내용에 의하여 영향을 받지 않습니다.

이것은 [이용허락규약\(Legal Code\)](#)을 이해하기 쉽게 요약한 것입니다.

[Disclaimer](#)

Doctoral Thesis

# Numerical Analysis on Rheological and Mechanical Properties of Polymeric Materials

Soowon Cho

School of Energy and Chemical Engineering  
(Chemical Engineering)

Ulsan National Institute of Science and Technology

2021

# Numerical Analysis on Rheological and Mechanical Properties of Polymeric Materials

Soowon Cho

School of Energy and Chemical Engineering  
(Chemical Engineering)

Ulsan National Institute of Science and Technology

# Numerical Analysis on Rheological and Mechanical Properties of Polymeric Materials

A thesis/dissertation submitted to  
Ulsan National Institute of Science and Technology  
in partial fulfillment of the  
requirements for the degree of  
Doctor of Philosophy

Soowon Cho

06.02.2021 of submission

Approved by



Advisor

Chunggi Baig

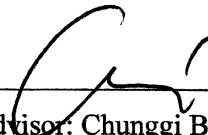
# Numerical Analysis on Rheological and Mechanical Properties of Polymeric Materials

Soowon Cho

This certifies that the thesis/dissertation of Soowon Cho is approved.

06.02.2021 of submission

Signature



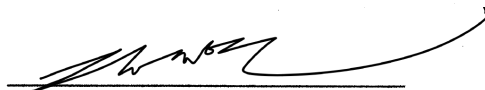
Advisor: Chunggi Baig

Signature



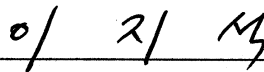
Hyunhyub Ko

Signature



So Youn Kim

Signature



Jiseok Lee

Signature



Jun Mo Kim

## Abstract

Nowadays, there has been demand for advanced composite materials due to their outstanding characteristics in wide ranges of academic and industrial fields. Composite materials usually possess improved properties not being observed in pure material itself. Particularly, polymer composite materials composed of constituents based on polymer matrix have been widely researched due to their highly enhanced capabilities (e.g., elasticity, flexibility, conductivity, hardness, stretchable, scalable, and so on) in various fields. Polymers, which are composed of structural repeat units with covalent bonds, have been gradually becoming essential and indispensable materials in the recent world owing to their high flexibility, elasticity, ease of processing, low cost, light weight, and other unique properties. Therefore, to utilize polymers more effectively for advanced composite materials, many fundamental studies have been researched to discover fundamental reasons (i.e., molecular origins) for their intrinsic characteristics corresponding to the polymer physics and rheology.

Recent experimental techniques offer some microscopic information. Nevertheless, it is still challenging issue to conduct a full atomic level analysis through only experimental approach. As such, depending on the rapid increase in computing power, multi-scale computer simulation methods have been developed to reveal the fundamental origin for some unique phenomena observed at the macroscopic level. Therefore, we conducted a detailed numerical analysis on rheological and mechanical properties of polymeric materials via mainly nonequilibrium molecular dynamics (NEMD) simulations and finite-element-method (FEM) simulations (Abaqus CAE and COMSOL Multiphysics).

In this dissertation, we first present comprehensive analysis on the shear rheology of polymers for various molecular architectures (linear, ring, and short-chain branched) in the bulk and confined systems using atomistic NEMD simulations. In comparison to bulk polymeric system, the interfacial chain dynamics near the boundary solid walls in the confined system are interesting. Detailed molecular-level analysis of the individual chain motions for various molecular architectures are carried out to characterize the intrinsic molecular mechanisms for interfacial chains in three characteristic flow regimes (weak, intermediate, and strong) regarding to the interfacial slip behavior (i.e., degree of slip).

Based on fundamental studies for polymers, we additionally modeled and analyzed polymer nanocomposites to fabricate versatile sensor devices using FEM simulations collaborated with experimental approach. Through a precise modeling in consideration to (particularly) mechanical properties, we found the most optimized construction of the nanostructured polymeric materials with highly improved sensing performances (ultrahigh sensitivity, linear sensing capability, and broad sensing range). Finally, we demonstrated highly sensitive triboelectric, ferroelectric, mechanochromic, and piezoresistive sensors with a proper physical (fundamental) mechanism to improve sensing ability.



## Contents

**Abstract**

**Contents**

**List of Figures**

<b>I. Research Background</b>	1
1.1 Polymer physics	1
1.2 Polymer rheology	5
1.3 Polymer nanocomposite materials	6
1.4 Computer simulation	7
<b>II. Shear Rheology of Polymers</b>	8
2.1 Introduction	8
2.2 Methods	12
2.3 Results and Discussion	17
2.3.1 Shear rheology of bulk polymers	17
2.3.2 Shear rheology of interfacial polymers	32
2.4 Conclusion	39
2.5 References	42
<b>III. Mechanical Properties of Polymer Nanocomposites</b>	47
3.1 Introduction	47
3.2 Methods	50
3.3 Results and Discussion	51
3.4 Conclusion	71
3.5 References	73
<b>IV. Summary</b>	81
<b>Acknowledgements</b>	84
<b>List of Publications</b>	85



## List of Figures

**Figure 1.1.1.** Schematic illustration of polymer.

**Figure 1.1.2.** Multi-scale simulation methods with respect to various time and length scales.

**Figure 2.2.1.** The probability distribution of C-C bond length for  $C_{78}H_{158}$  and  $C_{400}H_{802}$  linear PE melts under shear flow.

**Figure 2.3.1.1.** Shear stress and material functions. Plots of (a) the shear stress  $\sigma_{xy}$ , (c) the shear viscosity  $\eta$ , and (d) the first normal stress coefficient  $\Psi_1$  for the simulated unentangled ( $C_{78}H_{158}$ ) and entangled ( $C_{400}H_{802}$  and  $C_{600}H_{1202}$ ) PE melts as a function of  $Wi$  number. The vertical dotted lines (black for  $C_{78}H_{158}$ , green for  $C_{400}H_{802}$ , and blue for  $C_{600}H_{1202}$ ) distinguish the distinctive scaling behaviors of the three characteristic (weak, intermediate, and strong) flow regimes. A schematic description in (b) illustrates the general trend of  $\sigma_{xy}$  for unentangled and entangled linear polymer melts under shear for the respective flow regime.

**Figure 2.3.1.2.** The variation of the intermolecular part of shear stress  $\sigma_{xy}$  as a function of  $Wi$  number for the simulated unentangled ( $C_{78}H_{158}$ ) and entangled ( $C_{400}H_{802}$  and  $C_{600}H_{1202}$ ) PE melts. The vertical dotted lines represent the same as with Figure 2.3.1.1.

**Figure 2.3.1.3.** Representative molecular scaling variables. Plots of (a) the average chain orientation angle  $\theta$  with respect to the flow ( $x$ -)direction, (b) the mean-square chain end-to-end distance, and (c) the intermolecular Lennard-Jones (LJ) potential energy as a function of  $Wi$  number for the unentangled ( $C_{78}H_{158}$ ) and entangled ( $C_{400}H_{802}$  and  $C_{600}H_{1202}$ ) PE melts. Variations of (d) the average number  $Z$  of chain entanglements, (e) the average length  $d_{es}$  of an entanglement strand, and (f) the probability distribution of entanglements  $P(Z)$  along the normalized chain primitive path (PP) contour segment  $s$  ranging from 0 to 1, as a function of  $Wi$  number for the entangled ( $C_{400}H_{802}$  and  $C_{600}H_{1202}$ ) systems. The vertical dotted lines represent the same as with Figure 2.3.1.1. All the properties from (a) to (e) are the statistical ensemble averaged ones for which the standard angular bracket marks (i.e.,  $\langle \rangle$ ) have been removed for notational simplicity in the main text.

**Figure 2.3.1.4.** Variations of the whole chain rotation (tumbling) time  $\tau_{rot}$  with respect to the applied flow strength for  $C_{78}H_{158}$ ,  $C_{400}H_{802}$ , and  $C_{600}H_{1202}$  PE melts. Here,  $\tau_{rot}$  is directly computed by measuring the accumulated orientational angle of the chain end-to-end vector in the flow-gradient ( $xy$ ) plane as a function of time.  $\tau_{rot}$  is practically identical to the time scale extracted from the power spectral density analysis through Fourier transformation of the time autocorrelation function  $\langle \mathbf{u}(t) \cdot \mathbf{u}(0) \rangle$  of the unit chain end-to-end vector  $\mathbf{u}(t)$ . We further note that the complete results for  $C_{600}H_{1202}$  melt could not be obtained in this work because a very long simulation trajectory (i.e., over 10 times longer than the longest relaxation time of the system especially in the intermediate flow regime) is required to obtain statistically reliable data for each state point. However, our preliminary results for

$C_{600}H_{1202}$  melt in the strong flow regime exhibit consistent scaling behaviors for  $\tau_{rot}$  in comparison with those of the  $C_{78}H_{158}$  and  $C_{400}H_{802}$  melts. The vertical dotted lines represent the same as with Figure 2.3.1.1.

**Figure 2.3.1.5.** (a) Schematic description of the numerical algorithm for constructing intrinsic ring surface. (b) Area projected from the intrinsic surface of the ring into three  $xy$ - (circles and dashed line),  $xz$ - (squares and solid line), and  $yz$ - (triangles and dotted line) planes for melt (orange symbols), dilute (black symbols), and toy model (dark green lines) as a function of Weissenberg number ( $Wi$ ). Note that these projected areas were normalized by the total area of the intrinsic ring surface  $A_t$ . (c) The ratio between  $A_{xy}$  and  $A_{xz}$  vs.  $Wi$  for melt (orange circles), dilute (black circles), and toy model (dark green line). (d) The  $zz$ -component of the gyration tensor  $\mathbf{G}$  normalized by the equilibrium value for linear (triangles) and ring (circles) polymers with respect to  $Wi$ .

**Figure 2.3.1.6.** (a) The steady state shear viscosity  $\eta$  and (b) the first normal stress coefficient  $\Psi_1$  as a function of the Weissenberg number  $Wi$  for the  $C_{128}H_{258}$  linear (Linear; black triangles),  $C_{400}H_{800}$  ring (Ring; black circles),  $C_{178}H_{358}$  SCB linear (SCB\_L; orange triangles), and  $C_{565}H_{1130}$  SCB ring (SCB\_R; orange circles) PE melt systems. The error bars are smaller than the size of the symbols unless otherwise specified. The slopes in (a) and (b) were calculated by fitting the  $\eta$  and  $\Psi_1$  in the shear-thinning regime through simple power-law expression of the forms  $\eta \sim Wi^{-b_1}$  and  $\Psi_1 \sim Wi^{-b_2}$  with slopes  $b_1$  and  $b_2$  (Linear; black solid line, Ring; black dotted line, SCB\_L; orange solid line, and SCB\_R; orange dotted line).

**Figure 2.3.2.1.** Degree of slip ( $d_s$ ) as a function of the reduced shear rate  $\dot{\gamma}^* \equiv \dot{\gamma} \sqrt{m\sigma^2 / \epsilon}$  for the simulated  $C_{128}H_{258}$  linear (Linear; black triangles),  $C_{128}H_{256}$  ring (Ring; black circles),  $C_{178}H_{358}$  SCB linear (SCB\_L; orange triangles), and  $C_{178}H_{356}$  SCB ring (SCB\_R; orange circles) PE melt systems. The vertical black dashed lines (Linear), black dash-dotted lines (Ring), and orange dashed line (SCB\_L and SCB\_R) separate the characteristic flow regimes with respect to  $d_s$  for each system. It is noted that while the linear and ring polymers exhibit three distinct characteristic  $d_s$  regimes (increasing, decreasing, and increasing) as a function of shear rate, the SCB systems show almost constant behavior of  $d_s$  in the weak and intermediate flow regimes and increasing behavior of  $d_s$  in the strong flow regime. The error bars are smaller than the size of the symbols unless otherwise indicated.

**Figure 2.3.2.2.** Schematic description of the characteristic molecular mechanisms for the interfacial linear, ring, SCB linear, and SCB ring polymers in the three representative (weak, intermediate, and strong) flow regimes. These mechanisms underlie the general behavior of the interfacial slip ( $d_s$ ) for each system.  $\zeta_w$  denotes the polymer-wall friction coefficient.

**Figure 2.3.2.3.** Streaming velocity profiles (normalized by the applied wall velocity  $V_w$ ) along the velocity gradient direction at a certain intermediate shear rate for the simulated  $C_{128}H_{258}$  linear (black triangles),  $C_{128}H_{256}$  ring (black circles),  $C_{178}H_{358}$  SCB linear (orange triangles), and  $C_{178}H_{356}$  SCB ring

(orange circles) PE melts. The solid line represents the ideal streaming velocity profile assuming the no-slip boundary condition.

**Figure 2.3.2.4.** The  $xx$ ,  $yy$ , and  $zz$  components of the gyration tensor  $G$  for the interfacial chains whose center-of-mass is located within a distance of  $2.5 \sigma$  from the wall for the (a)  $C_{128}H_{258}$  linear (black triangles) and  $C_{178}H_{358}$  SCB linear (orange triangles) and (b)  $C_{128}H_{256}$  ring (black circles) and  $C_{178}H_{356}$  SCB ring (orange circles) systems as a function of the applied shear rate. To allow comparison with the pure ring and linear systems, only the chain backbone, excluding the short branches, was considered in the calculation of  $G$  for the SCB systems. The symbols and vertical lines have the same meaning as in Figure 2.3.2.1. The error bars are smaller than the size of the symbols unless otherwise indicated.

**Figure 3.2.1.** Schematic illustration of the Finite Element Method (FEM) simulation.

**Figure 3.3.1.** Structural characteristics of highly-sensitive triboelectric sensors.

**Figure 3.3.2.** Theoretical analysis of the gap distance change in the interlocked films. The finite element simulations by using ABAQUS software for the gap distance change ( $\Delta d$ ) from the initial gap in the interlocked microdome-structured and planar films with respect to the applied vertical pressure. Note that while the elastic modulus of P(VDF-TrFE) is constant as 1 GPa for all sizes of microdome arrays, that of PDMS decreases with the larger width/pitch size of microdome arrays due to the effect of nanoporous structure.

**Figure 1.3.3.** Theoretical analysis of the stress distribution in the interlocked films under the vertical pressure. The finite element simulations of the stress distribution depending on the elastic modulus of interlocked and microdome-structured polymers by using ABAQUS software. The elastic modulus of P(VDF-TrFE) and PDMS is 1 GPa and 3 MPa, respectively. Left and right panels show the result for the contact interaction for the interlocked PDMS-PDMS and the P(VDF-TrFE)-PDMS layers, respectively.

**Figure 3.3.4.** The finite element simulations for the comparison of vertical stress concentration with the different width/pitch size of interlocked and microdome-structured polymers by using Abaqus software under the applied vertical pressure (40 kPa). The elastic modulus of P(VDF-TrFE) is 1 GPa, and that of PDMS is varied depending on the width/pitch size of microdome arrays.

**Figure 3.3.5.** The finite element simulations for the comparison of the numerical calculation of (a) contact area and (b) relative contact areal change with the different width/pitch size of interlocked and microdome-structured polymers by using Abaqus software under the applied vertical pressure. The elastic modulus of P(VDF-TrFE) is 1 GPa, and that of PDMS is varied depending on the width/pitch size of microdome.

**Figure 3.3.6.** (a) Schematic illustration of gap distance change of TESs under vertical pressure and theoretically calculated electric field distribution and (b) density of point contact between interlocked

microridges under bending strain and coincident theoretically calculated electric field distribution by COMSOL simulations depending on the width ( $w$ ) and pitch ( $p$ ) size of interlocked microdome arrays ( $w/p = 25/30, 50/60, \text{ and } 100/120 \mu\text{m}$ ) and planar structures.

**Figure 3.3.7.** Structural characteristics of highly-sensitive ferroelectric sensors.

**Figure 3.3.8.** The finite element simulations of (a) the contact area change as a function of pressure for different numbers of stacked layers and (b) the local stress distribution for different numbers of interlocked layers showing the concentrated and amplified stress at the small spot between interlocked microdomes under a pressure of 100 kPa.

**Figure 3.3.9.** Structural characteristics of highly-sensitive mechanochromic sensors.

**Figure 3.3.10.** The finite element simulations of (a) stress distributions of mechanochromic polymers with different pore sizes (left) and with 300-nm SNPs and a 5- $\mu\text{m}$  pore size (right) under a tensile strain of 50% and maximum localized stress near the pore surface in porous mechanochromic polymers with (b) different pore sizes and (c) different SNP sizes and a pore size of 5  $\mu\text{m}$  as a function of strain (see Figure 3.3.11 for the initial system configuration).

**Figure 3.3.11.** Simulated surface areas of porous mechanochromic composites with different pore sizes based on face-centered cubic (FCC) unit cell arrays. The porous structures are modelled according to average pore sizes of 50, 25, 10 and 5  $\mu\text{m}$  with the same porosity (26%) based on FCC unit cell arrays. Volume is determined as the total material volume, excluding the pore volume. Area is the total surface area of the porous structure.

**Figure 3.3.12.** The finite element simulations of stress distributions of porous PDMS/SP composites with different pore sizes (25, 10 and 5  $\mu\text{m}$ ) placed under 50% tensile strain calculated numerically using Abaqus software. For simplicity, the elastic modulus is set to 1 MPa with the same porosity (26%) for all porous composites (see Figure 3.3.11 for the initial system configuration).

**Figure 3.3.13.** The finite element simulations of stress distribution of porous PDMS/SP composites (pore size = 5  $\mu\text{m}$ ) decorated with SNPs with different sizes (300, 100 and 20 nm) placed under 50% tensile strain calculated numerically using Abaqus software. For simplicity, to understand the role of the SNPs at the pore walls, the elastic modulus of the porous matrix is set to 0.24 MPa (consistent with the experimental data). The elastic modulus of the SNPs is set to a general value of 180 GPa for all sizes.

**Figure 3.3.14.** (a) Relative color changes of porous PDMS/SP composites with different pore sizes in response to applied normal pressure. (b) The finite element simulations of stress distributions in porous PDMS/SP composites with different pore sizes under applied normal pressure. The simulation conditions are identical to those in Figure 3.3.12.

**Figure 3.3.15.** (a) Relative color intensities of porous PDMS/SP composites (pore size = 5  $\mu\text{m}$ ) decorated with SNPs of different sizes (20, 100, and 300 nm) as functions of vertical pressure. (b) The finite element simulations of stress distributions at the surfaces of pores in porous PDMS/SP composites with SNPs under applied pressure. The simulation conditions are identical to those in Figure 3.3.13.

**Figure 3.3.16.** Structural characteristics of highly-sensitive piezoresistive sensors.

**Figure 3.3.17.** Comparison of pressure sensors with sandwiched electrode and coplanar electrode. (a) Working mechanism of the pressure sensor with sandwiched electrode. The total resistance ( $R_T$ ) depends on both contact resistance ( $R_c$ ) and bulk resistance ( $R_f$ ). (b) Pressure-sensing mechanism of the pressure sensor with coplanar electrode. The total resistance depends on sheet resistance ( $R_s$ ) and contact resistance, but mainly on contact resistance.

**Figure 3.3.18.** The finite element simulations of the local stress distribution for piezoelectric sensors with (a) top and bottom PDMS layers and (b) the stiffness-gradient interlocked structure with top PDMS layer and bottom TPU layer using Abaqus software. The simulated top and bottom layers were composed of PDMS or TPU materials corresponding to each condition, with interlocked microdome structures with a diameter of 10  $\mu\text{m}$  and a pitch of 12  $\mu\text{m}$  (i.e., unit cell of hexagonal arrays). The elastic modulus of PDMS and TPU materials were 1.98 MPa and 65 MPa, respectively, which were consistent with the experimental values.

**Figure 3.3.19.** Schematic illustration and pressure-sensing trends of multi-layered e-skin under (a) low pressure range, (b) medium pressure range, and (c) high pressure range. The red line represents the relative current change of the triple-layered pressure sensor based on the superposition of pressure-dependent electrical current of each layer in multi-layers.

**Figure 3.3.20.** Experimental results (symbol) and numerical results (solid line) of the electric current for single-layered pressure sensors with different sheet resistance; (a) 300  $\text{k}\Omega/\text{sq}$ , (b) 60  $\text{k}\Omega/\text{sq}$ , and (c) 226  $\Omega/\text{sq}$ .

**Figure 3.3.21.** Simple numerical analysis of ideal electrical behaviors on (a,b) double-layered and (c,d) triple-layered sensors. The lower index ( $I_{1,\text{single}}$ ,  $I_{2,\text{single}}$ , and  $I_{3,\text{single}}$ ) represents the inner layer for both double- and triple-layered sensors. We adopt a form of the Heaviside step function,

$H(\Delta P - \Delta P_0)$ , with the associated threshold pressure,  $\Delta P_0$ , which is an ideal way to describe the delayed conductive behavior of the inner layer for multi-layered sensors. Note that the overall electrical behavior of the double ( $I_{\text{double}}$ ) and triple ( $I_{\text{triple}}$ ) layers are obtained *via* the linear

superposition of each single layer as  $I_{\text{double}} = I_{2,\text{single}} + H(\Delta P - \Delta P_0)I_{1,\text{single}}$  and

$I_{\text{triple}} = I_{3,\text{single}} + H(\Delta P - \Delta P_0)I_{2,\text{single}} + H(\Delta P - \Delta P_1)I_{1,\text{single}}$ .

**Figure 3.3.22.** Numerical analysis of realistic electrical behaviors in (a) single-layered, (b) double-layered, and (c) triple-layered sensors. The lower index ( $I_{1,\text{single}}$ ,  $I_{2,\text{single}}$ , and  $I_{3,\text{single}}$ ) represents the inner layer for both double- and triple-layered sensors. We adopt a more physical form of the Boltzmann-type exponential function ( $1 - e^{-(\beta\Delta P)^\gamma}$ ) to describe the delayed conductive behavior of inner layer for multi-layered sensors. Note that the overall electrical behavior of double ( $I_{\text{double}}$ ) and triple ( $I_{\text{triple}}$ ) layers are obtained *via* the linear superposition of each single layer as

$$I_{\text{double}} = I_{2,\text{single}} + [1 - e^{-(\beta_2\Delta P)^{\gamma_2}}] I_{1,\text{single}} \quad \text{and}$$

$$I_{\text{triple}} = I_{3,\text{single}} + [1 - e^{-(\beta_3\Delta P)^{\gamma_3}}] I_{2,\text{single}} + [1 - e^{-(\beta_3\Delta P)^{\gamma_3}}] [1 - e^{-(\beta_2\Delta P)^{\gamma_2}}] I_{1,\text{single}} .$$

**Figure 3.3.23.** Schematic illustration and pressure-sensing trends of (a) single-layered sensor, (b) double-layered sensor, and (c) triple-layered sensor. (d) Experimental results (symbol) and numerical results (solid line) of the electric current for single layered sensors (60 k $\Omega$ /sq and 226  $\Omega$ /sq, respectively), and double-layered sensor (226  $\Omega$ /sq and 60 k $\Omega$ /sq). (e) Experimental results (symbol) and numerical results (solid line) of the electric current for single-layered sensors (300 k $\Omega$ /sq, 60 k $\Omega$ /sq and 226  $\Omega$ /sq, respectively), and triple-layered sensor (226  $\Omega$ /sq, 60 k $\Omega$ /sq, and 300 k $\Omega$ /sq). (f) Experimental results (symbol) and numerical results (solid line) of single-layered sensor (226  $\Omega$ /sq), double-layered sensor (226  $\Omega$ /sq and 60 k $\Omega$ /sq), and triple-layered sensor (226  $\Omega$ /sq, 60 k $\Omega$ /sq, and 300 k $\Omega$ /sq). Here, the higher resistive layer represents the outer layer for multi-layered sensors.

**Figure 3.3.24.** Experimental results (symbol) and numerical results (line) of the ideal model (226  $\Omega$ /sq, 2 k $\Omega$ /sq, and 20 k $\Omega$ /sq); single-layered sensor (226  $\Omega$ /sq), double-layered sensor (226  $\Omega$ /sq and 2 k $\Omega$ /sq), and triple-layered sensor (226  $\Omega$ /sq, 2 k $\Omega$ /sq, and 20 k $\Omega$ /sq). The numerical results of electrical behavior for the double and triple layers were obtained via equations 3.1.3 and 3.1.5.

# I. Research Background

## 1.1 Polymer physics

Polymer is composed of many repeating subunits called monomers as described in Figure 1.1.1. As a result, it has numerous connectivities inside their microstructure. From these connectivities, polymeric materials show different behavior in comparison with simple fluid such as argon. Bond connectivity induces the increase of internal structural entropy (microstructure), which makes interesting properties for polymeric materials. Actually, the pure liquid is viscous, and pure solid has elastic mechanical properties. However, due to the variation of polymer microstructures, polymeric materials are not only viscous also elastic. This is called viscoelastic properties, which makes polymeric materials to be promising versatile materials. Regardless of polymer chemistry, just focusing on this polymer microstructure is important in polymer physics. Therefore, entropic effects are mainly dominant in polymer physics rather than energetic effects. Based on these perspectives, there are two main models to describe polymer dynamics, Rouse and Reptation (tube) model, in polymer physics. Rouse model describes the polymer behavior by dividing polymer chain with a Brownian motion of bead and Gaussian spring. Therefore, it is also called as bead-spring model. This model was first proposed by Rouse and effectively has been the basis of the unentangled polymer dynamics (dilute solutions). Here, unentangled polymer corresponds to short-chain length (under entanglement molecular weights,  $M_e$ ) polymer. However, the molecular weight is long enough, polymer chain starts to feel significant topological constraints. Therefore, a polymer chain is almost confined in a tube-like region due to the surrounding chains. As a result, a polymer chain shows reptation motion in imaginary tube. This is well-known reptation (tube) model for entangled polymer dynamics. Based on the statistical mechanics, these models effectively describe the scaling behavior of polymers in a view of correlation length scale. With this aspect, unentangled and entangled models will be carefully discussed in detail.

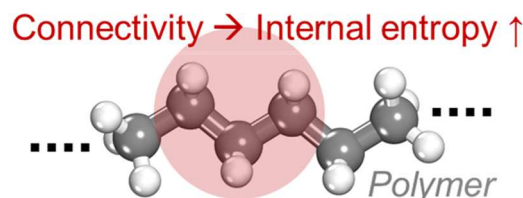


**Figure 2.1.1.** Schematic illustration of polymer.

*Unentangled polymer dynamics (Rouse model)*

Unentangled polymer dynamics model, called Rouse model (also bead-entropic spring model), describes the conformational dynamics of polymer chain in a microscopic molecular level. In this model, the single chain is represented by a Brownian motion of beads connected by harmonic springs. Actually, this model develops from the dilute polymer solutions, however there is no hydrodynamic interaction (HI) and excluded volume (EV) effects. Therefore, it effectively describes polymeric melts system rather than dilute solutions. Although there are some assumptions (i) macroscopic time scale (consider only steady-states), (ii) Gaussian chain model, (iii) no HI, and (iv) no EV effects, Rouse model is analytically solved without any empirical parameters. Specifically, Rouse model describes the unentangled polymer dynamics by dividing a polymer chain with  $N$  beads (1 bead size corresponds to 1 Kuhn length) and  $N-1$  Gaussian springs (Gaussian spring constant  $k = 3k_B T / b^2$ , where  $k_B$ ,  $T$ , and  $b$  denote a Boltzmann constant, temperature, and Kuhn length). Spring constant  $k$  can be derived from the Gaussian distribution function  $\Psi(\vec{r}) \sim \exp(-\frac{3r^2}{2b^2}) / r^2$  with a probability density function  $\Psi(\vec{r})$  and position vector  $\vec{r}$ . Here, a normalized factor  $1/r^2$  comes from this analytical feature  $\int \Psi(\vec{r}) r^2 dr d\theta d\phi = 1$ . Then, a free energy and entropy of a polymer chain can be expressed as following expressions  $A(\vec{r}) = E(\vec{r}) - TS(\vec{r})$  and  $S(\vec{r}) = c + k_B \ln \Psi(\vec{r})$ , respectively, with energy term of polymer chain  $E(\vec{r})$ . For conformational dynamics of polymer chains, an entropic effect is significantly dominant than an energetic effect in polymer. Therefore, we can consider only an entropic effect in a free energy expression excluding energetic effect and represent with a following expression:

$$A(\vec{r}) = E(\vec{r}) - TS(\vec{r}) \approx -TS(\vec{r}) = -k_B T \ln \Psi(\vec{r}) = \frac{3k_B T}{2b^2} r^2. \quad (1.1.1)$$

In addition, a spring force can be expressed as:

$$F(\vec{r}) = -\frac{\partial A(\vec{r})}{\partial \vec{r}} = -\frac{3k_B T}{b^2} \vec{r} = -k\vec{r}. \quad (1.1.2)$$

Likewise, a Gaussian spring constant  $k$  can be derived with this expression  $k = 3k_B T / b^2$ . Here, the Kuhn length  $b$  depends on polymeric materials. If the value of  $b$  increase, a polymer chain could be more flexible. On the contrary to this, if  $b$  decrease, a polymer chain would be more stiff and rigid. Based on these observations, Rouse model can be called with a bead-(entropic) spring model. Since we generally ignore energetic effect on polymer chains, we carefully adopt a bead-spring model to avoid these systems (i) highly short chain length polymers, (ii) rigid polymers, and (iii) under high flow field corresponding to less conformational change in polymer dynamics.



Now, we can further extend our analysis on the equations of motion for beads of polymer chains with following equation:

$$m \frac{d^2 \vec{R}_i}{dt^2} = F_i = -\frac{\partial U^{\text{Spring}}}{\partial \vec{R}_i} + F^{\text{B}} + F^{\text{F}} + F^{\text{E}}, \quad (1.1.3)$$

where  $m$  and  $\vec{R}_i$  denote a mass and position vector of bead  $i$ , respectively.  $F_i$ ,  $U^{\text{Spring}}$ ,  $F^{\text{B}}$ ,  $F^{\text{F}}$ ,  $F^{\text{E}}$  indicate a inertial force of bead  $i$ , interaction potential, Brownian (thermal) random force for each bead at certain temperature  $T$ , frictional force, and external force, respectively. For Rouse model, there are some assumption, (i) time scale ( $m \frac{d^2 \vec{R}_i}{dt^2} \rightarrow 0$  due to steady-state), (ii) Gaussian chain approximation (if high flow field is applied, this assumption would be not allowed), (iii) hydrodynamic interaction is neglected, (iv) excluded volume effect is neglected, and (v) under equilibrium condition ( $F^{\text{E}} \rightarrow 0$ ). Following with these assumptions for Rouse model, equation (1.1.3) can be finally organized as follows:

$$-F^{\text{F}} = \xi \frac{\partial \vec{R}_i}{\partial t} = -\frac{\partial U^{\text{Spring}}}{\partial \vec{R}_i} + F^{\text{B}}. \quad (1.1.4)$$

This expression (1.1.4) is widely well-known theoretical equation of Rouse model, where  $\xi$  denotes friction coefficient. Using Fourier transform, we can analytically obtain  $\vec{R}_i(t)$  and time correlation information  $\langle X_{p\alpha}(t) X_{q\beta}(0) \rangle$ . With these observations, we can obtain well-known properties for a

Rouse chain such as (i) longest relaxation time (i.e., Rouse time)  $\tau_{\text{R}} = \frac{\xi N^2 b^2}{3\pi^2 k_{\text{B}} T}$ , (ii) dynamical

property: diffusion coefficient  $D_{\text{G}} = \frac{k_{\text{B}} T}{N \xi}$ , (iii) structural property: mean-squared end-to-end distance

$\langle R_{\text{ete}}^2 \rangle = N b^2$ , and (iv) polymeric stress  $\sigma_{\alpha\beta} \sim \frac{1}{V} \langle \vec{R}_{\alpha} \vec{F}_{\beta} \rangle$ . As you can see, Rouse model can be

considered as two parameter models with  $N \xi$  and  $\sqrt{N} b$ , which directly associated with dynamical and structural aspects, respectively. If we know each value of these two parameters, we can obtain all physical measurement through a precise statistical mechanics.

*Entangled polymer dynamics (Reptation/Tube model)*

Generally, Reptation model is considered as extended Rouse model for entangled polymers above entanglement molecular weights  $M_e$ . In Rouse model, we consider only single polymer chain as similar with dilute polymer solutions. Therefore, a polymer chain can freely move with 3-dimensional isotropic chain dynamics and there is no intermolecular interaction. However, in Reptation model (concentrated condition), we should consider intermolecular interactions resulting restricted 1-dimensional degree of freedom of chain dynamics. It means that a polymer chain has only itself contour path due to surrounding chains (i.e., topological constraints) like in a tube-like region. Thus, Reptation model is also called as Tube model. As a result, the topological constraints (chain entanglements) disturb polymer chain dynamics, thus a polymer chain in a tube-like region cannot overcome its constraints due to energetic effects. Therefore, in Reptation (tube) model, we consider Rouse model condition plus topological constraints. Reptation model was first proposed by de Gennes to describe the restricted chain dynamics only moving along its own contour path called the primitive path (PP), which indicates geometrically the shortest pathway in the tube-like region connecting the chain ends, like creeping motion of snake in the forest. This feature was called reptation motion based on the Latin *reptare*. By de Gennes and Doi-Edwards, the tube theory (Reptation model) was established to describe entangled polymer dynamics in consideration to the topological constraints through an effective mean-field tube and dynamics of the PP for each chain in the entangled polymeric system. As a result, the contour length of PP can be obtained as  $L_{pp} = Nb^2 / d_{pp}$ , where  $d_{pp}$  denotes a tube diameter, since the mean-squared end-to-end vector of the primitive chain should be the same with  $Nb^2$  of Rouse chain. Furthermore, as following with tube theory, the longest relaxation time is also calculated with this expression  $\tau_d = \frac{1}{\pi^2} \frac{\xi N^3 b^4}{k_B T d_{pp}^2}$ . Interestingly, in contrast to the Rouse time  $\tau_R$  (which is proportional to  $N^2$ ),  $\tau_d$  is proportional to  $N^3$  considering the effect of topological constraints on entangled polymer dynamics. This demonstrates the crucial effect of topological constraints on the conformational change of polymer chains in entangled polymer dynamics.

Although entangled polymer chain dynamics is almost restricted to its contour path by surrounding chains, these topological constraints can be additionally released itself (CR) and contour length fluctuation (CLF) of chain ends is also to help release of topological constraints. These two factors have important influences on the entangled polymeric system. As following with experimental results,  $\tau_d$  is proportional to  $N^{3.4}$  rather than  $N^3$ . The value of 3.4 of exponent comes from the CR and CLF effects in real polymeric systems.

## 1.2 Polymer rheology

Polymer physics (models) are generally originated from the equilibrium condition for polymer materials in the absence of the flowing condition. Therefore, to figure out the flow effect on polymeric materials under nonequilibrium condition, it is also important to understand polymer rheology. Rheology is the study of stress and deformation relationship under the applied flow condition (e.g., shear and elongational flow). For example, when we apply some shear flow or perturbation on the polymeric system, we can measure material functions such as viscosity or normal stress in response to external field through proper constitutive equations. Likewise, in polymer rheology, we elucidate the relationship between stress induced by external flow field and system response originated by conformational deformation of polymer materials. Actually, the constitutive equations are well-defined for only Newtonian fluid like water. However, the constitutive equation for non-Newtonian fluid like polymeric materials is still not established due to their complicated behaviors. Therefore, in the field of rheology, to understand Weissenberg effect or die swell phenomena, the final goal is to obtain well-described constitutive equations of stress for certain polymeric materials. In nature, the polymeric systems can be divided with these two standard systems: bulk and confined systems. The major difference between them is the existence of surface effect. Due to the effect of solid surface, confined (interfacial) polymers show different behavior in comparison with bulk polymers such as a solid-like behavior, high viscosity, oscillatory density and so on. Still these days, there is less information about fundamental reasons to describe their macroscopic phenomena even for bulk polymers. Generally, microscopic behaviors directly affects to macroscopic properties or material functions. That's why we closely focused on microscopic level molecular dynamics to understand their macroscopic properties.

Polymeric fluids exhibit a variety of distinctive structural and dynamic behaviors (especially under flowing conditions) and associated versatile properties due to the multiplicity of the intrinsic time and length scales inherent to polymers in association with their diverse internal microstructures. This enables many practical applications, such as polymer processing, lubrication, adhesion, nanocomposites, and biotechnology. Importantly, the characteristic time scales vary significantly with the chain length and molecular architecture (e.g., linear, ring, or branched polymers) in addition to the polymer concentration and system conditions (e.g., temperature and pressure). This can lead to drastic changes in the physical and rheological properties of polymeric materials. In turn, the ability to manipulate the spatial and temporal scales is tremendously advantageous in practical applications because it allows systematically controlling and tailoring the material properties. Thus, numerous research efforts have been made in the past to establish the fundamental knowledge on the dependence of the characteristic scales and rheological properties of flowing polymeric materials on the chain length and polymer architecture in bulk or interfacial systems.

### 1.3 Polymer nanocomposite materials

With these basic understandings for pure polymeric materials, the advanced polymer composites could be developed. Polymer nanocomposites consist of polymer and nanofillers such as nanoparticles, fibers, clusters, and so on. There are countless cases considering factors like filler shape, dispersion, size, and the degree of interaction with polymer matrix. And then, with this mixture, through a micromold or substrate, the polymer composites can be generated considering the optimized composition, surface nanostructure or morphology. And then finally it will be constructed to final product such as multifunctional real sensor devices. However, is it possible to cover all of things with only experimental approach? There should be limitation like countless cases, high cost, inefficiency, and limited length scale. That's why more fundamental and systematic approaches are also needed to advance polymer nanocomposite materials.

Nowadays, devices based on multi-functional smart sensor techniques are gradually attracting public attentions to improve the quality of personal life (e.g., flexible, wearable, and skin-attachable devices, wireless and self-powered apparatus, electronic and artificial skin). Based on above fundamental studies for polymeric materials, we have additionally researched to produce a versatile sensor as applicational studies. We proposed the most optimized nanostructured polymer composite materials and demonstrated appropriate physical sensing mechanisms via the finite element method (FEM) simulation. Note that it is quite difficult to carry out overall procedures to produce a versatile sensor covering from the research on specific materials in details and controlling their micro-structures through only experiments, since there are countless number of cases to consider as candidates and many infeasible measurements throughout the micro- to nano-scale (e.g., the contact area, stress propagation and concentration, electric field distribution, and etc.). Therefore, through a precise modeling with multi-scale simulations collaborated with experimental processing, the most optimized construction of the nanostructured polymer composite materials with highly improved sensing performances (e.g., ultrahigh sensitivity, linear sensing capability, broad sensing range, etc.) would be possible. Thus, we have researched considering that which polymer composite material would be utilized with deep understanding of its real benefits and disadvantages for certain sensors (in particular for triboelectric, ferroelectric, mechanochromic, and piezoelectric sensors) with multi-scale simulations collaborated with actual experimental approach.

### 1.4 Computer simulation

We utilized the multi-scale computer simulation to achieve our research goal. Recently, thanks to the enhanced computing power, there are various ranges of computer simulation from the quantum, atomistic, coarse-grained, and continuum levels as described in Figure 1.1.2 with respect to various time and length scales. In particular, the molecular dynamics (MD) simulation in the atomistic and coarse-grained levels are usually executed to investigate the fundamental origin or molecular characteristics underlying macroscopic observations in the field of polymeric materials. Through a detailed analysis using MD simulation, we can directly observe molecular dynamics, microscopic properties and phenomena based on the Newtonian and statistical mechanics, which significantly affects to macroscopic observations.

In addition, for applicational research, the coarse-grained and continuum level simulation (e.g., FEM) are performed to describe real polymeric processing or collaborate with actual experimental approach. For example, considering the microstructure or surface morphology (e.g., interlocked micro-dome, -pyramid, and -square arrays, porosity, stacking, inserting nanoparticles, and so on) with a precise physical (fundamental) mechanism to improve sensing ability, we can demonstrate each multi-functional versatile sensor based on the nanostructured polymer composite materials with these nano-controlled compositions of composites.

Likewise, computer simulation can be a bridge role between theory and experiment to complement their limitations. Through computer simulation, we can reveal microscopic fundamental characteristics underlying macroscopic phenomena, observe infeasible measurements, guide to experimental conditions, and demonstrate theoretical and experimental results.

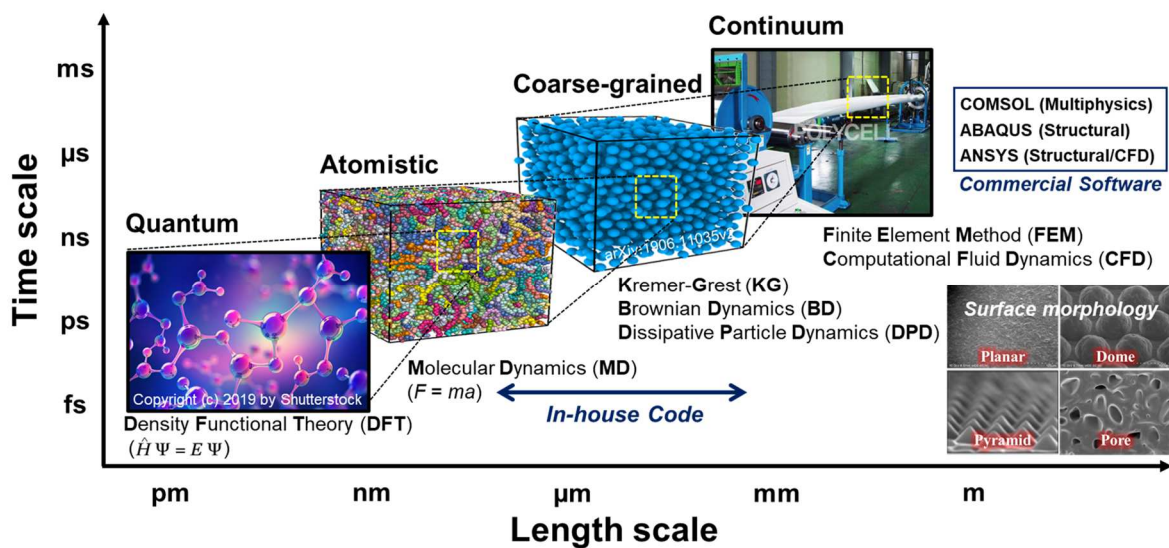


Figure 1.1.2. Multi-scale simulation methods with respect to various time and length scales.

## II. Shear Rheology of Polymers

---

This chapter includes the materials from:

1. Jeong, S. H.<sup>†</sup>; **Cho, S.**<sup>†</sup>; Ha, T. Y.; Roh, E. J.; Baig, C.\* Structural and Dynamical Characteristics of Short-Chain Branched Ring Polymer Melts at Interface under Shear Flow. *Polymers* **2020**, *12*, 3068.
  2. Jeong, S. H.<sup>†</sup>; **Cho, S.**<sup>†</sup>; Roh, E. J.<sup>†</sup>; Ha, T. Y.<sup>†</sup>; Kim, J. M.<sup>†</sup>; Baig, C.\* Intrinsic Surface Characteristics and Dynamic Mechanisms of Ring Polymers in Solution and Melt under Shear Flow. *Macromolecules* **2020**, *53*, 10051-10060.
  3. **Cho, S.**<sup>†</sup>; Kim, J. M.<sup>†</sup>; Baig, C.\* Scaling Characteristics of Rotational Dynamics and Rheology of Linear Polymer Melts in Shear Flow. *Macromolecules* **2020**, *53*, 3030-3041.
  4. Jeong, S.; **Cho, S.**; Kim, J. M.; Baig, C.\* Interfacial Molecular Structure and Dynamics of Confined Ring Polymer Melts under Shear Flow. *Macromolecules* **2018**, *51*, 4670-4677.
  5. Jeong, S. H.<sup>†</sup>; Kim, J. M.<sup>†</sup>; **Cho, S.**; Baig, C.\* Effect of short-chain branching on interfacial polymer structure and dynamics under shear flow. *Soft Matter* **2017**, *13*, 8644-8650.
  6. **Cho, S.**; Jeong, S.; Kim, J. M.\*; Baig, C.\* Molecular dynamics for linear polymer melts in bulk and confined systems under shear flow. *Scientific Reports* **2017**, 9004.
  7. Jeong, S.; **Cho, S.**; Kim, J. M.; Baig, C.\* Molecular mechanisms of interfacial slip for polymer melts under shear flow. *Journal of Rheology* **2017**, *61*, 253-264.
- 

### 2.1 Introduction

Polymeric fluids exhibit a variety of distinctive structural and dynamic behaviors (especially under flowing conditions) and associated versatile properties due to the multiplicity of the intrinsic time and length scales inherent to polymers in association with their diverse internal microstructures. This enables many practical applications, such as polymer processing, lubrication, adhesion, nanocomposites, and biotechnology. Importantly, the characteristic time scales vary significantly with the chain length and molecular architecture (e.g., linear, ring, and branched polymers) in addition to the polymer concentration and system conditions (e.g., temperature and pressure). This can lead to drastic changes in the physical and rheological properties of polymeric materials. In turn, the ability to manipulate the spatial and temporal scales is tremendously advantageous in practical applications because it allows systematically controlling and tailoring the material properties. Thus, numerous research efforts have been made in the past to establish the fundamental knowledge on the dependence of the characteristic scales and rheological properties of flowing polymeric materials on the chain length and polymer architecture in bulk or interfacial systems.<sup>1-4</sup>

In the field of rheology, it is still challenging issue how to elucidate general scaling behaviors of macroscopic rheological responses (i.e., material functions) with fundamental origins under

nonequilibrium conditions for both unentangled and entangled polymeric materials. In linear viscoelastic regimes, viscoelastic properties are nearly invariable showing a Newtonian plateau, whereas in nonlinear viscoelastic regimes, polymers undergo significant deformation (i.e., distorted intrinsic molecular networks) exhibiting a variety of interesting phenomenon (e.g., shear thinning behavior for shear stress and normal stress) depending on several important factors such as chain length, polymer architecture, and type of imposed flow. In particular, the scaling behavior of the material functions (e.g., viscosity) for polymer solutions or melts with respect to the flow type and strength have been informative to characterize material properties and tune the product quality for various polymer processes. Accordingly, numerous experimental and theoretical studies have been conducted for decades, revealing a variety of rheological scaling characteristics. For instance, above a certain critical flow strength, which can be roughly estimated as the Weissenberg number  $Wi \simeq 1$  as defined by the product of the longest characteristic relaxation time of the system and the imposed flow rate, it is typically observed for polymeric liquids that the shear viscosity  $\eta$  and the first normal stress coefficient  $\Psi_1$  decrease as the applied shear rate  $\dot{\gamma}$  increases (i.e., shear-thinning behavior prevails). Specifically, simple power-law expressions of the form  $\eta \sim \dot{\gamma}^{-b_1}$  and  $\Psi_1 \sim \dot{\gamma}^{-b_2}$  with  $0.40 \leq b_1 \leq 0.95$  and  $1.3 \leq b_2 \leq 1.7$  have been reported for most polymer solutions and melts both experimentally<sup>2,5-8</sup> and through simulations.<sup>9-20</sup> In perspective of the structure–property relationship, such nonlinear rheological behavior is supposed to be directly associated with structural (conformational) changes in the polymer chains due to the flow. In this respect, optical (e.g., birefringence) measurements have been extensively applied in practice to estimate the stress of deformed polymeric materials under various flow fields.<sup>1,2,4,21-23</sup> Flow birefringence measurements have been useful for estimating the stress of flowing polymeric liquids via the linear relationship between the stress tensor and the birefringence tensor [the so-called stress-optical rule (SOR)] in the range of flow strength spanning from the linear up to a certain (rather weakly) intermediate flow regime under shear or elongation. This indicates that the degree of anisotropy in the chain orientation and stretch with respect to the flow strength is an important fundamental structural characteristic governing the rheological behavior.

However, birefringence measurements become less informative for polymer systems at high flow fields where chains are highly stretched and the SOR is likely to break down, as has been shown in various experiments and simulations.<sup>1,2,4,21-23</sup> In fact, SOR has a rigid molecular basis only when the chain is not too much deformed or stretched. Therefore, it would be useful if we could find certain (empirical) scaling relationships that may work throughout the intermediate-to-strong flow regime (which will be shown in this study). Attempts have been made to modify SOR through introduction of the chain stretch and the corresponding stiffening of the chains under strong flow. However, we might find simpler relationships in a sense similar to an experimental approach correlating rheological and structural data.

Severe failure of SOR under very strong flow fields can be readily understood by considering that the degree of chain orientation and stretch along the flow direction would be eventually saturated in such fields. Therefore, it is necessary to account for the rather complicated dynamic influences beyond the purely structural ones to properly represent the stress variations in the strong flow regime. An additional important factor that determines the stress for entangled polymer systems is the degree of entanglement (topological constraints) between chains, which has been well established in both theory and experiments.<sup>1,7-8,15,19-20,24</sup>

It is widely known that even with the same chemical composition and molecular weight, the structural and dynamical properties of polymers can be significantly altered by varying their molecular architecture, i.e., by using either a linear or branched structure.<sup>25-33</sup> Thus far, however, most research efforts aiming to explore the fundamental role of branches in polymer science have mainly focused on long-chain branched polymers, although it is equally well known that short-chain branching generally significantly affects a wide variety of physical properties such as crystallinity, melting point, modulus, and the hardness of polymeric materials. From a thermodynamic viewpoint, the standard approach would be to analyze the structure of polymers in solution or melt by accounting simultaneously for the energetics (polymer-polymer and polymer-solvent) and (intramolecular and intermolecular) entropy of the system, and then to determine the properties of the system based on the resulting structural information. This conventional approach, though generally effective for long-chain branched polymers, may cause significant errors in the case of polymeric materials containing chains with branches along the main backbone that are rather short, as this is likely to lead to the presumption of a negligible entropic contribution by such short branches. Short-chain branches are able to play a prominent role in polymer dynamics on account of their intrinsic fast kinetic nature, which enables them to exert a strong influence on the overall structural and dynamical properties of the system. A concrete understanding of the structure-property-phenomenon-process linkage would be attained only by truly grasping the distinctive roles of long and short branches.

Over the past decades, intensive research has been carried out to understand the structural and rheological behaviors of ring polymers in dilute solutions and melts.<sup>34-37</sup> In comparison to linear polymers, ring polymers exhibit a variety of distinctive structural and dynamical properties. Practically, ring polymers are directly relevant to biological systems, and they serve as a model system for biophysical problems, such as circular plasmid DNA<sup>38,39</sup> and chromatin packing in nucleosomes.<sup>40,51</sup> It is generally known that ring polymers possess relatively compact structures compared with their corresponding linear analogs. For instance, various experiments and simulations have reported that ring melts display unusual chain-dimension scaling behavior with respect to molecular weight  $M_w$ , e.g.,  $1/3 \leq \nu \leq 0.4$  for the chain radius of gyration  $R_g \approx M_w^\nu$ , which is in sharp contrast to  $\nu = 0.5$  for linear melts.<sup>36,42-46</sup> Pure ring melts typically exhibit a smaller viscosity, larger diffusion coefficient, and faster relaxation behavior compared with their corresponding linear analogs. These structural and dynamical



features have also been supported by several theoretical analyses, such as the Flory-like mean-field approach,<sup>14</sup> lattice animal model,<sup>48,49</sup> and crumpled globule model.<sup>46,50,51</sup> Other theoretical and numerical works looked into the minimal surface area of ring polymers, which has been applied to analyze the physical characteristics of inter-ring concatenation or penetration and the effective topological constraints.<sup>52-56</sup> Notably, the well-known reptation or tube theory, which has most successfully described the rheological behavior of entangled linear polymer systems, cannot be properly applied to the ring system because of the absence of chain ends that are necessary for chain reptation through a one-dimensional curvilinear confined (mean-field) tube.

Recent nonequilibrium molecular dynamics (NEMD) simulations for bulk ring polymeric melt systems under shear and planar elongational flows showed that ring polymers exhibit a stronger resistance to structural deformation against the applied flow field, leading to a substantially lower degree of chain stretch and alignment in the flow direction.<sup>57</sup> This feature results in less shear-thinning and extension-thinning behaviors for ring systems compared with their linear analogs.<sup>57</sup> Similar characteristics were observed in experiments.<sup>58,59</sup> Another NEMD study on confined ring melts undergoing shear flow revealed that the ring polymer exhibits a weaker interfacial (wall) slip in the weak-to-intermediate flow regime compared with its linear analog.<sup>60</sup> This was attributed to the longer chain dimension of the ring polymers in the neutral direction at the wall, thereby resulting in large polymer-wall friction. This study further revealed characteristic molecular mechanisms, such as loop wagging, loop migration, and loop tumbling dynamics for interfacial ring chains. Other simulation studies have reported additional dynamical mechanisms for ring chains, such as mutual threading dynamics,<sup>54,55</sup> tank-treading dynamics,<sup>61,62</sup> and hydrodynamic inflation.<sup>59,63-66</sup> Other coarse-grained NEMD simulations using the Kremer–Grest model for ring melts under uniaxial extensional flow showed the formation of supramolecular rings linked with multiple individual ring chains, resulting in a distinctively high strain-hardening of viscosity, as reported in previous experiments.<sup>67,68</sup>

There still remain many unresolved rheological issues (especially from the microscopic viewpoint) for polymeric materials in bulk or confined system, e.g., fundamental mechanisms underlying stress overshoot, interfacial slip, and melt instability for polymer melts under shear flow. To systematically control such rheological phenomena, it is most essential to comprehend the intrinsic molecular dynamics of individual polymer chains separately in bulk and confined situations and how they compare to each other, which would greatly help build the general knowledge of accurately capturing physical aspects underlying such complex macroscopic responses of polymer systems and tuning the materials properties in response to an arbitrary external flow field. Molecular-level information attained by directly tracking down individual chain motions is applied to understand rheological behaviors of representative meso- and macroscopic structural and dynamical properties in response to the applied flow field in a wide range of flow strengths.

## 2.2 Simulation Methodology

In this work, we conducted atomistic canonical nonequilibrium molecular dynamics (NEMD) simulations of polyethylene (PE) melts using the well-known  $p$ -SLLOD algorithm<sup>69</sup> implemented with the Nosé–Hoover thermostat<sup>70,71</sup> and the Lees–Edwards sliding-brick boundary conditions<sup>72</sup>:

$$\dot{\mathbf{q}}_{ia} = \frac{\mathbf{p}_{ia}}{m_{ia}} + \mathbf{q}_{ia} \cdot \nabla \mathbf{u}, \quad (2.1.1)$$

$$\dot{\mathbf{p}}_{ia} = \mathbf{F}_{ia} - \mathbf{p}_{ia} \cdot \nabla \mathbf{u} - m_{ia} \mathbf{q}_{ia} \cdot \nabla \mathbf{u} \cdot \nabla \mathbf{u} - \zeta \dot{\mathbf{p}}_{ia}, \quad (2.1.2)$$

$$\dot{\zeta} = \frac{p_\zeta}{Q}, \quad \dot{p}_\zeta = \sum_i \sum_a \frac{\mathbf{p}_{ia}^2}{m_{ia}} - DNk_B T, \quad Q = DNk_B T \tau^2, \quad (2.1.3)$$

where  $\mathbf{q}_{ia}$ ,  $\mathbf{p}_{ia}$ , and  $\mathbf{F}_{ia}$  denote the position, peculiar momentum, and force vector of atom  $a$  of the mass  $m_{ia}$  in molecule  $i$ , respectively. Correspondingly,  $\zeta$ ,  $p_\zeta$ , and  $Q$  to the coordinate-like variable, the momentum-like variable, and the mass parameter, respectively, of the Nosé–Hoover thermostat.  $D$ ,  $N$ , and  $\tau$  denote the dimensionality of the system, the total number of atoms, and the thermostat relaxation time parameter, respectively.  $\tau$  was set equal to 0.24 ps for all simulations.  $k_B$  denotes the Boltzmann constant. The velocity gradient tensor ( $\nabla \mathbf{u}$ ) for simple shear flow is written as

$$\nabla \mathbf{u} = \begin{bmatrix} 0 & 0 & 0 \\ \dot{\gamma} & 0 & 0 \\ 0 & 0 & 0 \end{bmatrix}, \quad (2.1.4)$$

where  $\dot{\gamma}$  is applied shear rate.

The well-known Siepmann-Karaboni-Smit (SKS) united-atom potential model<sup>73</sup> was adopted for all PE melts because of its high accuracy in predicting rheological properties of linear alkanes, except for that the original rigid bond was replaced by a flexible one with a harmonic spring. In the SKS model, the nonbonded intermolecular and intramolecular interactions are described by a pairwise 6-12 Lennard-Jones (LJ) potential:

$$U_{\text{LJ}}(r_{ij}) = 4\varepsilon_{ij} \left[ \left( \frac{\sigma_{ij}}{r_{ij}} \right)^{12} - \left( \frac{\sigma_{ij}}{r_{ij}} \right)^6 \right], \quad (2.1.5)$$

where  $\varepsilon_{ij} = (\varepsilon_i \varepsilon_j)^{1/2}$  and  $\sigma_{ij} = (\sigma_i + \sigma_j) / 2$  are based on the standard Lorentz-Berthelot mixing rules between atomic units  $i$  and  $j$ . The LJ energy and size parameters were set equal to  $\varepsilon/k_B = 47$  K and  $\sigma = 3.93$  Å for the CH<sub>2</sub> units, and  $\varepsilon/k_B = 114$  K and  $\sigma = 3.93$  Å for the CH<sub>3</sub> units. A cut-off distance equal to  $2.5 \sigma_{\text{CH}_2}$  was employed in the simulations. Note that the intramolecular LJ interaction was active only between atoms separated by more than three bonds along the chain. The bonded atomic

interactions [bond-stretching ( $U_{\text{str}}$ ), bond-bending ( $U_{\text{ben}}$ ), and bond-torsional ( $U_{\text{tor}}$ )] were described by the following expressions:

$$U_{\text{str}}(l) = \frac{k_{\text{str}}}{2}(l-l_{\text{eq}})^2, \quad (2.1.6)$$

$$U_{\text{ben}}(\theta) = \frac{k_{\text{ben}}}{2}(\theta-\theta_{\text{eq}})^2, \quad (2.1.7)$$

$$U_{\text{tor}}(\phi) = \sum_{m=0}^3 a_m (\cos \phi)^m, \quad (2.1.8)$$

where the bond-stretching constant  $k_{\text{str}}/k_{\text{B}} = 452,900 \text{ K}/\text{\AA}^2$ , the equilibrium bond length  $l_{\text{eq}} = 1.54 \text{ \AA}$ , the bond-bending constant  $k_{\text{ben}}/k_{\text{B}} = 62,500 \text{ K}/\text{rad}^2$ , and the equilibrium bond angle  $\theta_{\text{eq}} = 114^\circ$ . The bond-torsional constants are set as  $a_0/k_{\text{B}} = 1010 \text{ K}$ ,  $a_1/k_{\text{B}} = 2019 \text{ K}$ ,  $a_2/k_{\text{B}} = 136.4 \text{ K}$ , and  $a_3/k_{\text{B}} = -3165 \text{ K}$ .

In the present united-atom potential model, we adopted the flexible harmonic C-C bond spring with a very strong spring force constant ( $k_{\text{str}}/k_{\text{B}} = 452,900 \text{ K}/\text{\AA}^2$ ) which was taken to be in accordance with experimentally measured spectroscopic data, as consistent with the general MM3 force field<sup>75</sup>. This gives rise to a bond-length fluctuation of  $\sim 2\%$  around the equilibrium bond length ( $1.54 \text{ \AA}$ ) even for high flow fields applied in this work, as seen in Figure 2.2.1 corresponding to the probability distribution results for the C-C bond length. We thus consider all the structural and dynamical data even in strong flow regime reported here to be essentially unaffected due to the (very stiff) harmonic springs.

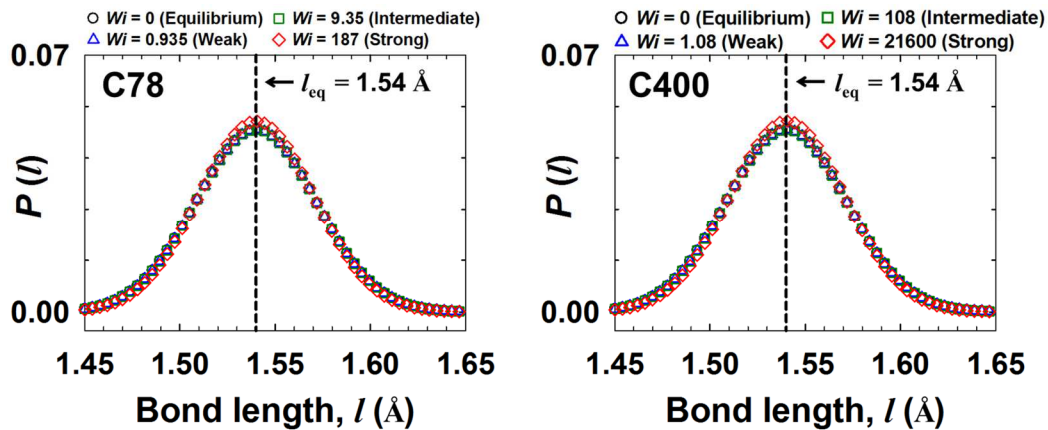


**Figure 3.2.1.** The probability distribution of C-C bond length for  $\text{C}_{78}\text{H}_{158}$  and  $\text{C}_{400}\text{H}_{802}$  linear PE melts under shear flow.

The set of evolution equations for each PE system was numerically integrated using the reversible reference system propagator algorithm (r-RESPA)<sup>74</sup> with two different time scales in the molecular dynamics (MD) step: the small time scale (0.47 fs) for bonded (bond-stretching, bond-bending, and bond-torsional) interactions, and the large time scale (2.35 fs) for the nonbonded Lennard–Jones (LJ) interactions, the Nosé–Hoover thermostat, and the external flow field. Specifically, we

utilized the r-RESPA algorithm to numerically integrate the evolution equations. The time propagator

$\mathbf{G}(\Delta t)$  for each atom can be derived as follows:

$$\begin{aligned}
\mathbf{G}(\Delta t) = & \exp\left[\frac{\Delta t}{2} F_s \frac{\partial}{\partial p_s}\right] \exp\left[\frac{\Delta t}{4} \mathbf{f}(\mathbf{r}_i) \frac{\partial}{\partial \mathbf{p}_i}\right] \exp\left[-\frac{\Delta t}{2} \frac{p_s}{Q} \mathbf{p}_i \cdot \frac{\partial}{\partial \mathbf{p}_i}\right] \\
& \times \exp\left[\frac{\Delta t}{4} \mathbf{f}(\mathbf{r}_i) \frac{\partial}{\partial \mathbf{p}_i}\right] \exp\left[-\frac{\Delta t}{2} m_i \mathbf{r}_i \cdot (\nabla u)_{input} \cdot (\nabla u)_{input} \frac{\partial}{\partial \mathbf{p}_i}\right] \\
& \times \exp\left[-\frac{\Delta t}{2} \mathbf{p}_i \cdot (\nabla u)_{input} \frac{\partial}{\partial \mathbf{p}_i}\right] \exp\left[\frac{\Delta t}{2} \frac{sp_s}{Q} \frac{\partial}{\partial s}\right] \exp\left[\frac{\Delta t}{2} \mathbf{r}_i \cdot (\nabla u)_{input} \frac{\partial}{\partial \mathbf{r}_i}\right] \\
& \times \exp[i\mathbf{L}_R \Delta t] \exp\left[\frac{\Delta t}{2} \mathbf{r}_i \cdot (\nabla u)_{input} \frac{\partial}{\partial \mathbf{r}_i}\right] \exp\left[\frac{\Delta t}{2} \frac{sp_s}{Q} \frac{\partial}{\partial s}\right] \\
& \times \exp\left[-\frac{\Delta t}{2} \mathbf{p}_i \cdot (\nabla u)_{input} \frac{\partial}{\partial \mathbf{p}_i}\right] \exp\left[-\frac{\Delta t}{2} m_i \mathbf{r}_i \cdot (\nabla u)_{input} \cdot (\nabla u)_{input} \frac{\partial}{\partial \mathbf{p}_i}\right] \\
& \times \exp\left[\frac{\Delta t}{4} \mathbf{f}(\mathbf{r}_i) \frac{\partial}{\partial \mathbf{p}_i}\right] \exp\left[-\frac{\Delta t}{2} \frac{p_s}{Q} \mathbf{p}_i \cdot \frac{\partial}{\partial \mathbf{p}_i}\right] \exp\left[\frac{\Delta t}{4} \mathbf{f}(\mathbf{r}_i) \frac{\partial}{\partial \mathbf{p}_i}\right] \exp\left[\frac{\Delta t}{2} F_s \frac{\partial}{\partial p_s}\right] . \quad (2.1.9)
\end{aligned}$$

The Liouville operator  $\mathbf{L}_R$  of the reference system is defined as

$$i\mathbf{L}_R = \frac{\mathbf{p}_i}{m_i} \frac{\partial}{\partial \mathbf{r}_i} + \mathbf{F}_R(\mathbf{r}_i) \frac{\partial}{\partial \mathbf{p}_i} . \quad (2.1.10)$$

All NEMD simulations were executed at constant temperature of  $T = 450$  K and density corresponding to a pressure of  $P = 1$  atm. A sufficiently large simulation box was employed for each system to minimize any undesirable effects by the system size. Furthermore, considering that chains become increasingly oriented and stretched along the flow direction as the shear rate increases, an extended box dimension in the flow ( $x$ -) direction was employed for each system. The box dimensions in the  $y$ - and  $z$ -directions were set as more than twice as large as the chain radius of gyration  $R_g$  of the system. A wide range of flow strengths covering linear up to highly nonlinear viscoelastic regimes was applied in the simulations. Here, the large-scale characteristic relaxation time of the system was estimated by the integral below the stretched-exponential curve describing the decay of the time autocorrelation function  $\langle \mathbf{u}(t) \cdot \mathbf{u}(0) \rangle$  of the unit chain end-to-end vector  $\mathbf{u}$  under equilibrium conditions using the stretched-exponential Kohlrausch–Williams–Watts (KWW) function of the form  $\langle \mathbf{u}(t) \cdot \mathbf{u}(0) \rangle = \exp(-(t / \tau_{\text{KWW}})^\beta)$ .<sup>76-78</sup> The  $\tau_{\text{KWW}}$  and  $\beta$  are the characteristic relaxation time and stretching exponent parameter, respectively. The correlation time  $\tau_c$  can be analytically evaluated using the formula  $\tau_c = \tau_{\text{KWW}} (\Gamma(1 / \beta) / \beta)$ .

We additionally note that in this study, the stress (and thus the shear viscosity  $\eta$  and the first normal stress coefficient  $\Psi_1$ ) and all the molecular properties (e.g., the average orientation angle  $\langle \theta \rangle$ , the mean-square chain end-to-end distance  $\langle R^2 \rangle$ , the average number  $\langle Z \rangle$  of chain entanglements, and the average length  $\langle d_{es} \rangle$  of an entanglement strand) were directly and independently calculated from atomistic NEMD simulations without any (coarse-graining) theoretical assumptions or hypotheses such as the Gaussian or the finitely extensible nonlinear elastic (FENE) entropic spring force that is typically adopted in standard coarse-grained polymer models and simulations. That is, in the present analysis of nonlinear rotational and rheological behaviors, the stress tensor  $\boldsymbol{\sigma}$  was calculated based on the rigorous Irving-Kirkwood statistical-mechanical formula for homogeneous fluids<sup>79</sup>,

$$\boldsymbol{\sigma} = \left\langle \frac{1}{V} \sum_i \sum_{\alpha} \left( \frac{\mathbf{p}_{i\alpha} \mathbf{p}_{i\alpha}}{m_{i\alpha}} + \mathbf{q}_{i\alpha} \mathbf{F}_{i\alpha} \right) \right\rangle, \quad (2.1.11)$$

where  $\mathbf{q}_{i\alpha}$ ,  $\mathbf{p}_{i\alpha}$ ,  $m_{i\alpha}$ , and  $\mathbf{F}_{i\alpha}$  are the position vector, momentum vector, mass, and force vector of atom  $\alpha$  in polymer molecule  $i$ , respectively, and  $V$  is the system volume. In this expression, the direct atomic force vector  $\mathbf{F}_{i\alpha}$  of atom  $\alpha$  in polymer molecule  $i$  was applied as

$$\mathbf{F}_{i\alpha} = \mathbf{F}_{i\alpha}^{\text{bs}} + \mathbf{F}_{i\alpha}^{\text{bb}} + \mathbf{F}_{i\alpha}^{\text{bt}} + \mathbf{F}_{i\alpha}^{\text{intra-LJ}} + \mathbf{F}_{i\alpha}^{\text{inter-LJ}}, \quad (2.1.12)$$

in accordance with the SKS atomistic potential model.<sup>73</sup> The superscripts bs, bb, bt, intra-LJ, and inter-LJ denote the bond-stretching, bond-bending, bond-torsional, intramolecular LJ, and intermolecular LJ interactions, respectively. It is thus understood that the force  $\mathbf{F}_{i\alpha}$  acting on each individual CH<sub>2</sub> or CH<sub>3</sub> unit in linear polyethylene molecules is purely mechanical and natural one without any coarse-graining theoretical assumptions or hypotheses, i.e., not associated with any of chain orientation and stretch and/or their degree of coupling as typically assumed in viscoelastic models and mesoscopic simulations such as the Gaussian or FENE chain entropic spring force. Therefore, the stress data obtained from the present atomistic NEMD simulations are practically equivalent to those measured in corresponding real experiments.

For the confined (i.e., interfacial) system, the simulation systems were confined by rigid simple cubic lattice walls where the lattice parameter of the simple cubic wall was set equal to  $\sigma_w = 1.33\sigma_{\text{CH}_2}$ . The LJ energy parameter of wall atoms in all PE systems was set as  $\varepsilon_w/k_B = 939$  K, which is comparable to that of a mica surface ( $\sim 200\text{-}400$  mJ/m<sup>2</sup>)<sup>80</sup>. Each wall atom was kept fixed at its lattice site during the simulations. The atomistic NEMD simulations were executed with the modified  $p$ -SLLOD algorithm with a Nosé-Hoover thermostat:

$$\dot{\mathbf{q}}_i = \frac{\mathbf{p}_i}{m_i} + \dot{\mathbf{q}}_i \cdot \nabla \mathbf{u} \quad , \quad (2.1.13)$$

$$\dot{\mathbf{p}}_i = \mathbf{F}_i(\mathbf{q}) - \mathbf{p}_i \cdot \nabla \mathbf{u} - m_i \mathbf{q}_i \cdot \nabla \mathbf{u} \cdot \nabla \mathbf{u} - \frac{p_s}{Q} \mathbf{p}_i - \frac{P_s}{Q} (m_i \mathbf{q}_i \cdot \nabla \mathbf{u} - m_i \mathbf{U}(\mathbf{q}_i)) \quad , \quad (2.1.14)$$

$$\dot{s} = \frac{P_s}{Q} \quad , \quad (2.1.15)$$

$$\dot{p}_s = F_s(\mathbf{p}_i) \quad , \quad (2.1.16)$$

where  $\mathbf{q}_{ia}$ ,  $\mathbf{p}_{ia}$ , and  $\mathbf{F}_{ia}$  denote the position, (nominal) peculiar momentum, and force vector of atom  $a$  of the mass  $m_{ia}$  in molecule  $i$ , respectively.  $s$  and  $p_s$  are coordinate-like and momentum-like variables, respectively, of the Nosé-Hoover thermostat.  $Q = DNk_B T \tau^2$  is thermostat mass parameter, where  $D$  and  $\tau$  are the dimensionality and relaxation time parameter, respectively. The  $\tau$  was set equal to 0.24 ps for all simulations.  $\mathbf{U}(\mathbf{q}_i)$  is the streaming velocity at position  $\mathbf{r}_i$ , which was evaluated based on a 5th order polynomial fitting throughout the total region in every MD step during simulation. The real peculiar momentum  $\mathbf{p}_i^{\text{real}}$  of each atom was then calculated by subtracting the streaming velocity at its position from its laboratory momentum:

$$\dot{\mathbf{p}}_i^{\text{real}} = \mathbf{p}_i + m_i \mathbf{q}_i \cdot \nabla \mathbf{u} - m_i \mathbf{U}(\mathbf{q}_i) \quad . \quad (2.1.17)$$

## 2.3 Results and Discussion

### 2.3.1 Shear rheology of bulk polymers

#### Correlation of Rheological Properties with Conformation for Linear Polymers Under Shear Flow

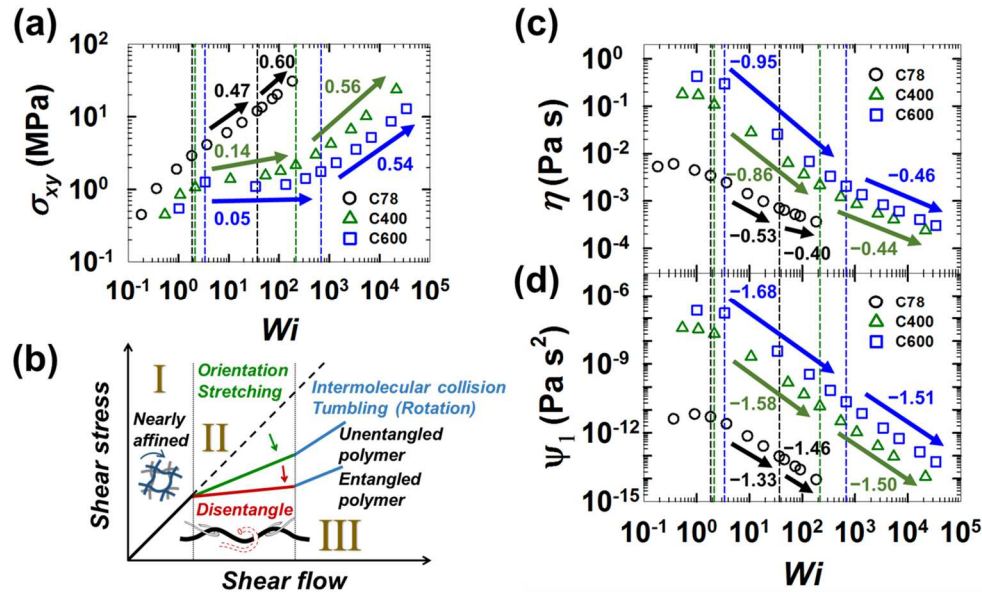


**Figure 2.3.1.1.** Shear stress and material functions. Plots of (a) the shear stress  $\sigma_{xy}$ , (c) the shear viscosity  $\eta$ , and (d) the first normal stress coefficient  $\Psi_1$  for the simulated unentangled ( $C_{78}H_{158}$ ) and entangled ( $C_{400}H_{802}$  and  $C_{600}H_{1202}$ ) PE melts as a function of  $Wi$  number. The vertical dotted lines (black for  $C_{78}H_{158}$ , green for  $C_{400}H_{802}$ , and blue for  $C_{600}H_{1202}$ ) distinguish the distinctive scaling behaviors of the three characteristic (weak, intermediate, and strong) flow regimes. A schematic description in (b) illustrates the general trend of  $\sigma_{xy}$  for unentangled and entangled linear polymer melts under shear for the respective flow regime.

**Unentangled Chains in Intermediate Flow Regime:** Figure 2.3.1.1 presents the plots of shear stress  $\sigma_{xy}$  vs.  $Wi$  for the simulated unentangled ( $C_{78}H_{158}$ ) and entangled ( $C_{400}H_{802}$  and  $C_{600}H_{1202}$ ) PE melts. One can identify the distinctive scaling behavior of  $\sigma_{xy}$  for each of the three (weak, intermediate, and strong) characteristic flow regimes. The standard Newtonian behavior,  $\sigma_{xy} \sim Wi^1$  (i.e., constant viscosity), emerges in the weak flow regime for all systems, which reflects the stress being proportional to the orientation anisotropy (as described by the stress-optical rule valid in the linear viscoelastic regime). In the intermediate flow regime, the scaling exponent  $\nu$  in  $\sigma_{xy} \sim Wi^\nu$  becomes smaller than unity, as typically observed in experiments.<sup>1-4</sup> This shear-thinning behavior arises from the increase in the degree of the average chain orientation toward the flow direction with increasing shear rate, thereby alleviating the stress imposed by the flow. While unentangled and entangled melts show a qualitatively similar behavior, the entangled systems exhibit significantly stronger shear-thinning than the unentangled

system, which confirms experimental observations.<sup>1-4</sup> This difference is attributed to the reduction in the degree of entanglement between chains for entangled systems as a result of collective chain alignment and stretch, as schematically depicted in Figure 2.3.1.1b. — see the intermolecular part  $\sigma_{xy}^{\text{inter}}$  of shear stress presented in Figure 2.3.1.2.

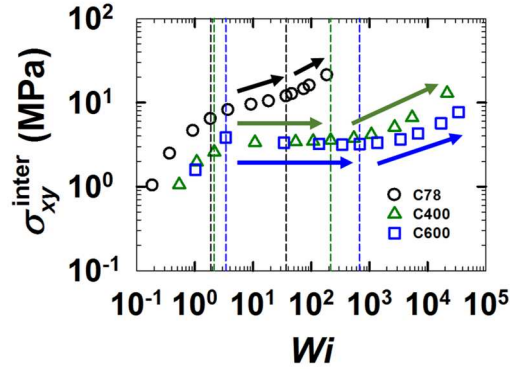


**Figure 2.3.1.2.** The variation of the intermolecular part of shear stress  $\sigma_{xy}$  as a function of  $Wi$  number for the simulated unentangled ( $C_{78}H_{158}$ ) and entangled ( $C_{400}H_{802}$  and  $C_{600}H_{1202}$ ) PE melts. The vertical dotted lines represent the same as with Figure 2.3.1.1.

Figures 2.3.1.1(c and d) summarize the overall scaling behavior of  $\eta$  and  $\Psi_1$  with respect to  $Wi$  under shear flow. The results are in good agreement with known experimental and computational results<sup>2,5,6,9-20</sup> where the scaling exponents of  $\eta \sim Wi^{-b_1}$  and  $\Psi_1 \sim Wi^{-b_2}$  are in typical ranges of  $0.40 \leq b_1 \leq 0.95$  and  $1.3 \leq b_2 \leq 1.7$  for most polymer solutions and melts in the intermediate flow regime. It is noted that the viscosity scaling of  $\eta \sim Wi^{-0.53}$  found for the unentangled  $C_{78}H_{158}$  melt in that regime appears very similar to that of  $\eta \sim Wi^{-0.52}$  observed for the dilute DNA solutions in experiment.<sup>5,6</sup> Also notable is that the degree of shear thinning for  $\eta$  and  $\Psi_1$  at high flow fields beyond the intermediate flow regime, described by  $\eta \sim Wi^{-(0.40-0.46)}$  and  $\Psi_1 \sim Wi^{-(1.46-1.51)}$ , becomes quantitatively very similar between unentangled and entangled PE melts; the physics underlying this rheological characteristics is discussed later.



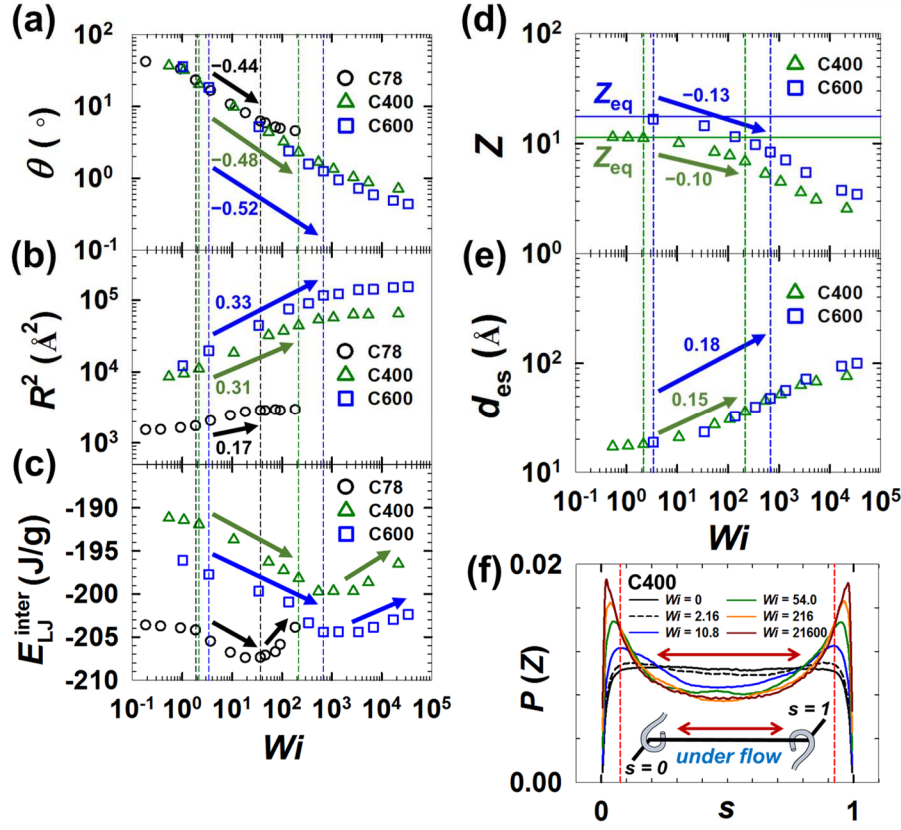


**Figure 2.3.1.3.** Representative molecular scaling variables. Plots of (a) the average chain orientation angle  $\theta$  with respect to the flow ( $x$ -)direction, (b) the mean-square chain end-to-end distance, and (c) the intermolecular Lennard-Jones (LJ) potential energy as a function of  $Wi$  number for the unentangled ( $C_{78}H_{158}$ ) and entangled ( $C_{400}H_{802}$  and  $C_{600}H_{1202}$ ) PE melts. Variations of (d) the average number  $Z$  of chain entanglements, (e) the average length  $d_{es}$  of an entanglement strand, and (f) the probability distribution of entanglements  $P(Z)$  along the normalized chain primitive path (PP) contour segment  $s$  ranging from 0 to 1, as a function of  $Wi$  number for the entangled ( $C_{400}H_{802}$  and  $C_{600}H_{1202}$ ) systems. The vertical dotted lines represent the same as with Figure 2.3.1.1. All the properties from (a) to (e) are the statistical ensemble averaged ones for which the standard angular bracket marks (i.e.,  $\langle \rangle$ ) have been removed for notational simplicity in the main text.

The primary molecular characteristic behind these shear-thinning behavior of  $\eta$  and  $\Psi_1$  lies in the variations in the degree of chain orientation and structural deformation with the flow strength. Thus, we extracted the average chain orientation angle  $\langle \theta \rangle$  and the mean square chain end-to-end distance  $\langle R^2 \rangle$  from the simulation, and examined their dependence on  $Wi$ .  $\langle \theta \rangle$  was calculated based on the well-known formula  $2\langle \theta \rangle = \tan^{-1} \left( 2\tilde{c}_{xy} / (\tilde{c}_{xx} - \tilde{c}_{yy}) \right)$  where  $\tilde{c}_{\alpha\beta}$  denotes the  $\alpha\beta$ -component of the second-rank conformation tensor  $\tilde{\mathbf{c}} = 3\langle \mathbf{R}\mathbf{R} \rangle / \langle R^2 \rangle_{eq}$  of the chain end-to-end vector  $\mathbf{R}$ . Note that this  $\langle \theta \rangle$  is identical to the angle formed between the flow direction and the eigenvector (called the director) corresponding to the largest eigenvalue of the order tensor  $\mathbf{S} = \langle (3\mathbf{u}\mathbf{u} - \mathbf{I}) \rangle / 2$  where  $\mathbf{u}$  represents the

unit chain end-to-end vector and  $\mathbf{I}$  a second-rank unit tensor.

It is noticed that both  $\theta$  and  $R^2$  vary steeply with  $Wi$  in the intermediate flow regime and relatively slowly in the strong flow regime in Figure 2.3.1.3(a and b). These features appear to be consistently reflected in the rheological behavior of  $\eta$  and  $\Psi_1$  in Figure 2.3.1.1(c and d). Quantifying the characteristic scaling behavior of  $\eta$  and  $\Psi_1$  with respect to the variation of the average chain configurations under the applied strong flow (in a sense similar to an experimental attempt of correlating rheological and structural data), we propose the following scaling expression for unentangled polymer systems in the intermediate flow regime:

$$\tilde{\eta} \sim \tilde{\theta}^{\alpha_1} \tilde{R}^2 \quad \text{and} \quad \tilde{\Psi}_1 \sim \tilde{\theta}^{\alpha_2} \tilde{R}^2. \quad (2.1.18)$$

Here,  $\tilde{\eta}$ ,  $\tilde{\Psi}_1$ ,  $\tilde{\theta}$ , and  $\tilde{R}^2$  represent dimensionless quantities normalized by the zero-shear viscosity  $\eta_0$ , zero-shear first normal stress coefficient  $\Psi_{1,0}$ , zero-shear orientation angle  $\theta_0 (= 45^\circ)$ , and  $R_{\text{eq}}^2$  at equilibrium, respectively. In equation 2.1.18, the exponent value of 2 for the  $R$ -dependence of  $\eta$  and  $\Psi_1$  is deduced from a consideration of the Gaussian entropic spring force. For higher accuracy, we can consider the finitely extensible nonlinear elastic (FENE) spring force by incorporating the multiplicative

factor  $\left(1 - \frac{R^2}{R_{\text{max}}^2}\right)^{-1}$  where  $R_{\text{max}}$  is the maximum stretched chain length.

It should be emphasized that the average orientation angle under shear flow appearing in equation 2.1.18 is not uniquely related to a quantity representing shear orientation anisotropy  $\langle u_x u_y \rangle$  (because  $\theta$  is calculated as  $\tan 2\theta = 2\langle u_x u_y \rangle / \langle u_x^2 - u_y^2 \rangle$ ). Consequently, the proposed scaling relationships (equation 2.1.18) do not correspond to the frequently utilized stress expression considering the entropic tension along the chain backbone, i.e.,  $\sigma_{\alpha\beta} \sim \langle F_\alpha R_\beta \rangle \sim kh \langle R_\alpha R_\beta \rangle$ ; here,  $F_\alpha = khR_\alpha$  is the entropic spring force expressed in terms of the Gaussian spring constant  $k \equiv 3k_B T / \langle R^2 \rangle_{\text{eq}}$  and a non-Gaussian spring contribution  $h$ . This expression with  $h = 1$  is equivalent to the well-established stress-optical rule (SOR) and has a rigid molecular basis under weak flow. Under strong flow, SOR fails and the expression is often modified as  $\sigma_{\alpha\beta} \sim kh \langle R^2 \rangle \langle u_\alpha u_\beta \rangle$  via the decoupling approximation. As a substitute for this approximate modification, we adopt the experimental sense of thinking explained above to propose equation 2.1.18 as a relationship between the rheological properties (or stress) and the chain conformation under strong flow: If we can measure  $\theta$  and  $R$  for polymer chains under strong flow, equation 2.1.18 may serve as a basis for resolving a conformational origin(s) of nonlinear rheological behavior. (At the same time, under weak flow, SOR is considered to be more fundamental and

quantitative compared to equation 2.1.18).

The present simulation results for the moderately strong flow (Figures 2.3.1.1c, 2.3.1.1d, 2.3.1.3a, and 2.3.1.3b) can be cast in the scaling form of equation 2.1.18 to give  $\tilde{\eta} \sim \tilde{\theta}^{1.59 \pm 0.13} \tilde{R}^2$  and  $\tilde{\Psi}_1 \sim \tilde{\theta}^{3.41 \pm 0.24} \tilde{R}^2$  for the unentangled  $C_{78}H_{158}$  PE melt, which demonstrates highly nonlinear dependence of both  $\eta$  and  $\Psi_1$  on the chain orientation. (The  $\theta$ -dependence of  $\eta$  and  $\Psi_1$  appeared fairly similar between the Gaussian and FENE models, because the average chain dimension is still much smaller than  $R_{\max}$  under shear flow) Notably, the exponent for the  $\theta$ -dependence of  $\Psi_1$  turns out to be approximately twice that of  $\eta$ . This result would be characteristic to the nonlinear rheological behavior of unentangled chains under moderately strong flow (with representing the stronger  $\theta$ -dependence of  $\Psi_1$  than  $\eta$  in this flow regime), although a superficial similarity is noted for that result ( $\eta^2 / \Psi_1$  being insensitive to  $\theta$ ) and the shear-rate independence of the  $\eta^2 / \Psi_1$  ratio rigidly established in the linear viscoelastic regime where chain deformation is assumed negligible (i.e.,  $R^2 \approx R_{eq}^2$ ) and related to SOR.

We confirmed that previous simulation data for unentangled polymers were re-cast in the scaling form of equation 2.1.18 to give the scaling exponent values similar to those shown above. For example, our analysis of the NEMD simulation works for unentangled  $C_{100}H_{202}^{12}$  and  $C_{128}H_{258}^{13}$  PE melts gave  $\tilde{\eta} \sim \tilde{\theta}^{1.78} \tilde{R}^2$  and  $\tilde{\Psi}_1 \sim \tilde{\theta}^{3.71} \tilde{R}^2$  for  $C_{100}H_{202}$ , and  $\tilde{\eta} \sim \tilde{\theta}^{1.80} \tilde{R}^2$  and  $\tilde{\Psi}_1 \sim \tilde{\theta}^{3.80} \tilde{R}^2$  for  $C_{128}H_{258}$  system (although  $C_{128}H_{258}$  is located in the crossover zone between the unentangled and entangled regimes and the agreement of its exponents may be rather fortuitous).

We also note that the scaling relationships for the unentangled  $C_{78}H_{158}$  melt appear very similar to those found in experiments for the dilute DNA solutions,<sup>5,6</sup>  $\tilde{\eta} \sim \tilde{\theta}^{1.53} \tilde{R}^2$  and  $\tilde{\Psi}_1 \sim \tilde{\theta}^{3.23} \tilde{R}^2$  and in additional Brownian dynamics (BD) simulations of a bead-rod coarse-grained linear chain including the hydrodynamic and excluded volume interactions between the beads (thereby mimicking real chains in dilute solutions),  $\tilde{\eta} \sim \tilde{\theta}^{1.58} \tilde{R}^2$  and  $\tilde{\Psi}_1 \sim \tilde{\theta}^{3.25} \tilde{R}^2$ . This apparent similarity possibly reflects the lack of the rheological influences from the effective topological constraints (entanglements) between chains in both systems.

Considering these observations and the numerical and statistical uncertainties in the NEMD simulation data, we estimated possible ranges of the scaling exponent  $\alpha$  for the  $\theta$ -dependence of  $\eta$  and  $\Psi_1$  for unentangled linear PE chains of various lengths;  $\alpha_1 = (1.5 \sim 1.7)$  for  $\eta$  and  $\alpha_2 = (3.2 \sim 3.6)$  for  $\Psi_1$ . We note that these scaling relationships were numerically extracted from the NEMD data without any a priori theoretical assumptions between the stress (i.e.,  $\eta$  and  $\Psi_1$ ) and molecular variables ( $\theta$  and  $R$ ), each of which was directly and independently measured from atomistic NEMD simulations.

Nevertheless, the properties calculated from simple viscoelastic models, such as Giesekus and FENE-P models, numerically obey somewhat consistent our proposed scaling relationships (although these relationships are not analytically deduced from the models).

**Entangled Chains in Intermediate Flow Regime:** Now, we focus on the nonlinear rheological behavior of entangled chains. For the entangled melt systems, the degree of interchain entanglement is an important factor for determining the rheological behavior. As is well known in polymer physics and rheology (e.g., in the tube theory and polymer network theory),<sup>1,2</sup> the entanglement segment vector is the primary object determining the stress tensor of deformed entangled polymer systems. Accordingly, we compared  $\eta$  and  $\Psi_1$  of entangled  $C_{400}$  and  $C_{600}$  PE chains with structural characteristics of the entanglement segments (not of the chain as a whole), such as the average number of entanglements per chain,  $Z$ , and the average orientation angle and length of those segments,  $\theta_{es}$  and  $d_{es}$ , all being normalized by respective values at equilibrium (obtained from the primitive path analysis of the entanglement network via the Z-code). In this comparison, we targeted the following scaling relationships, again in a sense similar to an experimental approach of correlating rheological and structural data, with incorporating the number of entanglement segments as an additional molecular variable:

$$\tilde{\eta} \sim \tilde{\theta}_{es}^{\beta_1} \tilde{Z}^{\gamma_1} \tilde{d}_{es}^2 \quad \text{and} \quad \tilde{\Psi}_1 \sim \tilde{\theta}_{es}^{\beta_2} \tilde{Z}^{\gamma_2} \tilde{d}_{es}^2. \quad (2.1.19)$$

The exponent for  $\tilde{d}_{es}$  appearing in equation 2.1.19 was set to be 2 with an assumption of Gaussian entropic force acting on the entanglement segment (as similar to the assumption underlying equation 2.1.18 for unentangled chains). Additionally, the NEMD simulation data for the  $C_{400}$  and  $C_{600}$  PE melt systems was found to exhibit a quantitatively similar scaling behavior between  $R$  and  $d_{es}$  with respect to  $Wi$  number. Therefore, the use of either  $\tilde{d}_{es}^2$  or  $\tilde{R}^2$  in equation 2.1.19 gives rise to practically the same scaling result for entangled melt systems. Because the scaling expression of  $\eta$  includes two independent variables  $\theta_{es}$  and  $Z$  with unknown exponents  $\beta_1$  and  $\gamma_1$ , it is impossible to uniquely separate the shear rate dependence of  $\eta$  into the  $\theta_{es}$  and  $Z$  dependencies. This situation is the same for  $\Psi_1$ . Thus, assuming that the entanglement strands considered here behave similarly to the whole backbone of unentangled chains in their contributions to the stress, we set the exponents  $\beta_1$  and  $\beta_2$  to be identical to the exponents for the unentangled chains  $\alpha_1 (= 1.59 \pm 0.13)$  and  $\alpha_2 (= 3.41 \pm 0.24)$ , respectively. This assumption would work under fast flow (although it should fail under slow flow in the linear regime). With this assumption, the exponents  $\gamma_1$  and  $\gamma_2$  can be evaluated from the shear rate dependence of  $\eta$ ,  $\Psi_1$ , and  $\theta_{es}$  obtained from the simulation and the dependence of  $Z$  estimated from the primitive path analysis.

Fitting the NEMD data of  $\eta$  and  $\Psi_1$  together with those of  $Z$  and  $d_{es}$  for the  $C_{400}$  and  $C_{600}$  PE

melts to equation 2.1.19 with the above assumption, we find the following scaling behavior:  $\tilde{\eta} \sim \tilde{\theta}_{es}^{1.59 \pm 0.13} \tilde{Z}^{3.97 \pm 0.21} \tilde{d}_{es}^2$  and  $\tilde{\Psi}_1 \sim \tilde{\theta}_{es}^{3.41 \pm 0.24} \tilde{Z}^{2.43 \pm 0.18} \tilde{d}_{es}^2$  for  $C_{400}$  and  $\tilde{\eta} \sim \tilde{\theta}_{es}^{1.59 \pm 0.13} \tilde{Z}^{3.72 \pm 0.25} \tilde{d}_{es}^2$  and  $\tilde{\Psi}_1 \sim \tilde{\theta}_{es}^{3.41 \pm 0.24} \tilde{Z}^{2.05 \pm 0.20} \tilde{d}_{es}^2$  for  $C_{600}$ . The scaling exponent for the  $Z$ -dependence of  $\eta$  appears to be larger than that of  $\Psi_1$ . Consistent behavior has been obtained by applying the present analysis based on equation 2.1.19 to previous NEMD simulation data for  $C_{400}H_{802}^{15}$  and  $C_{700}H_{1402}^{19}$  PE melt systems, i.e.,  $\tilde{\eta} \sim \tilde{\theta}_{es}^{1.59} \tilde{Z}^{4.10} \tilde{d}_{es}^2$  and  $\tilde{\Psi}_1 \sim \tilde{\theta}_{es}^{3.41} \tilde{Z}^{2.67} \tilde{d}_{es}^2$  for  $C_{700}$ , lending support to the scaling approach adopted in this study. We should point out that there may be a small discrepancy between the present results and those of  $C_{700}H_{1402}$  PE melts<sup>19</sup> due to some improved corrections in the  $Z$ -code utilized in this study for obtaining the entanglement network of the system through the contour reduction procedure, which might have made a small influence on the value of the scaling exponent of  $Z$ . Based on these observations, we estimated a possible range for the scaling exponents regarding the  $Z$ -dependence of  $\eta$  and  $\Psi_1$  for entangled linear PE melts, i.e.,  $\gamma_1 = (3.8 \sim 4.0)$  for  $\eta$  and  $\gamma_2 = (2.1 \sim 2.4)$  for  $\Psi_1$ .

While the  $C_{400}$  and  $C_{600}$  PE melts employed in this study are rather short and only mildly entangled systems, we believe that the basic features of the scaling expressions deduced for those chains remain valid for longer, strongly entangled chains within statistical uncertainties. Nevertheless, considering the rheological influence of entanglement segments near the chain ends (e.g., the effect of the contour length fluctuations in the tube theory<sup>1</sup>), which is particularly important for rather weakly entangled melt systems, the scaling exponent for the  $Z$ -dependence reported here may change slightly and approach gradually an asymptotic value as the chain length increases to highly entangled polymer melts. Furthermore, the scaling relationships (equation 2.1.19) may be adapted to entangled branched polymers with additional scaling component of the arm orientation and stretch at the junction points along the chain backbone whose scaling behavior is to be the same as that of entangled linear polymers.

**Linear Chains in Strong Flow Regime:** We now consider the scaling behavior of  $\eta$  and  $\Psi_1$  at high flow strengths. As shown in Figures 2.3.1.1c, the scaling exponent of  $\eta$  with respect to  $Wi$  number in the strong flow regime is significantly smaller than that in the intermediate flow regime for each melt (similarly for  $\Psi_1$ , but with a rather small change). If we keep the scaling expression equation 2.1.18, we obtain the following result:  $\tilde{\eta} \sim \tilde{\theta}^{2.39} \tilde{R}^2$  and  $\tilde{\Psi}_1 \sim \tilde{\theta}^{8.28} \tilde{R}^2$  for  $C_{78}$  PE melt under high flow fields, which is quantitatively inconsistent with that of the intermediate flow regime. This inconsistency arises from the weak variations of  $\theta$  and  $R$  with shear rate in the strong flow regime. In fact, the average chain orientation angle  $\theta$  becomes very small ( $< 5^\circ$ ) at the end of the intermediate flow regime, and its absolute variation at high shear rates is practically negligible. Thus, we expect a rather insignificant role of the

$\theta$  variable in determining rheological behavior under strong flow fields. Similarly, the average chain dimension does not change much with  $Wi$  in the strong flow regime.

In short, both chain orientation and chain stretch are nearly saturated at high  $Wi$ , and accordingly, their rheological influences would be negligible. Therefore, the scaling expression equation 2.1.18 for  $\eta$  and  $\Psi_1$  would no longer be valid under strong flow. Furthermore, a large portion of the entanglements become located closely to the chain ends at high  $Wi$  as a result of a high degree of collective chain alignment to the flow direction. Such entanglements are likely to be easily destroyed in a relatively short time under fast flow and would therefore not contribute effectively to the (elastic) stress of polymers.

In this regard, we consider another essential physical mode which becomes particularly important in the strong flow regime. We can imagine that the chain motion in this regime is very fast and irregular in association with intensive chain rotation and tumbling dynamics. Consequently, the degree of intermolecular collisions between chains would be very high and govern the overall polymer conformation and dynamics — see Figure 2.3.1.3c for a dramatic increase of the intermolecular LJ energy  $E_{LJ}^{\text{inter}}$  in the strong flow regime, which is in contrast with its gradual decrease in the intermediate regime via the mutual chain alignment and stretch. Physically, the intermolecular collisions enhance the momentum transfer process between chains, thus increasing the stress. Therefore, we need to take into account the effect of interchain collisions to correctly describe the dependence of  $\eta$  and  $\Psi_1$  on  $Wi$  in the strong flow regime. We assert that the stress governed by the collision-induced momentum transfer can be a general feature under strong flow fields emerging for any polymer architecture and flow type (e.g., shear or elongational flow).

Precise quantification of the rheological contribution of the intermolecular collision is very difficult due to the intricate dynamic nature of molecular collisions. Instead, we propose the following ad-hoc scaling expression for  $\eta$  and  $\Psi_1$  indirectly in terms of the average chain rotation time  $\tau_{\text{rot}}$ , assuming that the intermolecular collisions dominantly influence the chain rotation and tumbling dynamics at high shear rates for both unentangled and entangled polymer systems:

$$\tilde{\eta} \sim \tilde{\tau}_{\text{rot}}^{\delta_1} \quad \text{and} \quad \tilde{\Psi}_1 \sim \tilde{\tau}_{\text{rot}}^{\delta_2}. \quad (2.1.20)$$

Here,  $\tilde{\tau}_{\text{rot}}$  is made dimensionless as normalized by the characteristic rotational relaxation time of the system at equilibrium. Based on the above argument, equation 2.1.20 would be valid for both entangled and unentangled polymers in the strong shear flow regime, regardless of the chain length. Confirming this scaling characteristic, the NEMD simulation data show that  $\tilde{\eta} \sim \tilde{\tau}_{\text{rot}}^{0.50}$  and  $\tilde{\Psi}_1 \sim \tilde{\tau}_{\text{rot}}^{1.83}$  for  $C_{78}$ ,  $\tilde{\eta} \sim \tilde{\tau}_{\text{rot}}^{0.54}$  and  $\tilde{\Psi}_1 \sim \tilde{\tau}_{\text{rot}}^{1.85}$  for  $C_{400}$ , and  $\tilde{\eta} \sim \tilde{\tau}_{\text{rot}}^{0.61}$  and  $\tilde{\Psi}_1 \sim \tilde{\tau}_{\text{rot}}^{2.01}$  for  $C_{600}$  PE melts based on the

results of rotational time  $\tau_{\text{rot}}$  in Figure 2.3.1.4. From this result, possible ranges for the scaling exponents for the  $\tau_{\text{rot}}$  (common for unentangled and entangled linear polymers) are estimated to be  $\delta_1 = (0.5\sim 0.6)$  for  $\eta$  and  $\delta_2 = (1.8\sim 2.0)$  for  $\Psi_1$ .

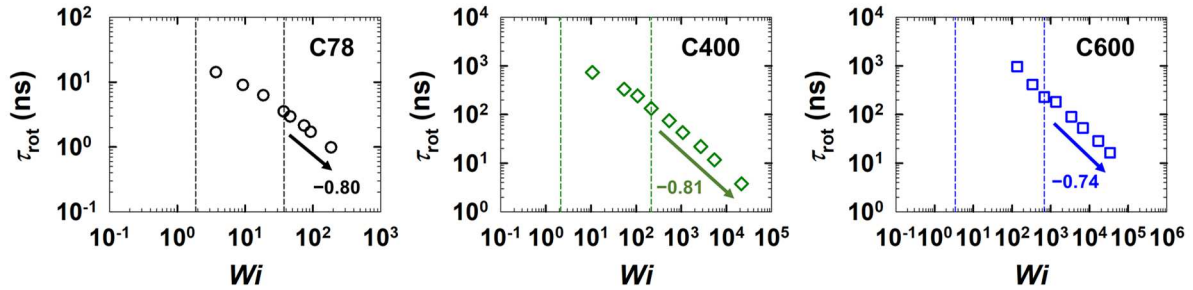


**Figure 2.3.1.4.** Variations of the whole chain rotation (tumbling) time  $\tau_{\text{rot}}$  with respect to the applied flow strength for  $C_{78}H_{158}$ ,  $C_{400}H_{802}$ , and  $C_{600}H_{1202}$  PE melts. Here,  $\tau_{\text{rot}}$  is directly computed by measuring the accumulated orientational angle of the chain end-to-end vector in the flow-gradient ( $xy$ ) plane as a function of time.  $\tau_{\text{rot}}$  is practically identical to the time scale extracted from the power spectral density analysis through Fourier transformation of the time autocorrelation function  $\langle \mathbf{u}(t) \cdot \mathbf{u}(0) \rangle$  of the unit chain end-to-end vector  $\mathbf{u}(t)$ . We further note that the complete results for  $C_{600}H_{1202}$  melt could not be obtained in this work because a very long simulation trajectory (i.e., over 10 times longer than the longest relaxation time of the system especially in the intermediate flow regime) is required to obtain statistically reliable data for each state point. However, our preliminary results for  $C_{600}H_{1202}$  melt in the strong flow regime exhibit consistent scaling behaviors for  $\tau_{\text{rot}}$  in comparison with those of the  $C_{78}H_{158}$  and  $C_{400}H_{802}$  melts. The vertical dotted lines represent the same as with Figure 2.3.1.1.

*Intrinsic Surface Characteristics of Ring Polymers in Solution and Melt under Shear Flow*

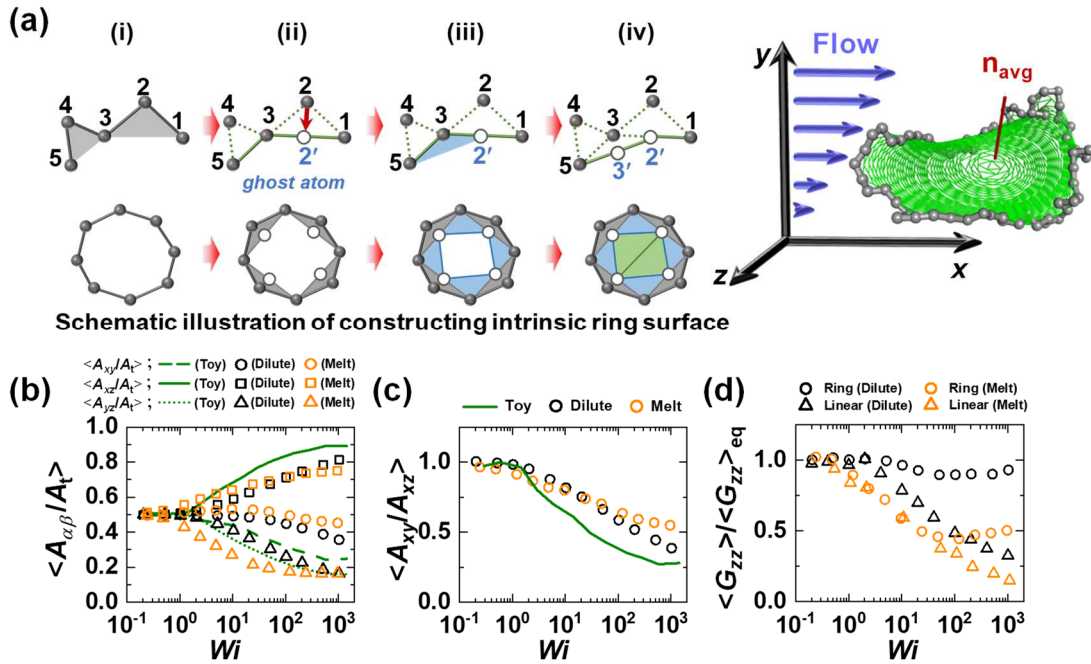


**Figure 2.3.1.5.** (a) Schematic description of the numerical algorithm for constructing intrinsic ring surface. (b) Area projected from the intrinsic surface of the ring into three  $xy$ - (circles and dashed line),  $xz$ - (squares and solid line), and  $yz$ - (triangles and dotted line) planes for melt (orange symbols), dilute (black symbols), and toy model (dark green lines) as a function of Weissenberg number ( $Wi$ ). Note that these projected areas were normalized by the total area of the intrinsic ring surface  $A_t$ . (c) The ratio between  $A_{xy}$  and  $A_{xz}$  vs.  $Wi$  for melt (orange circles), dilute (black circles), and toy model (dark green line). (d) The  $zz$ -component of the gyration tensor  $\mathbf{G}$  normalized by the equilibrium value for linear (triangles) and ring (circles) polymers with respect to  $Wi$ .

Starting from the viewpoint that the ring polymer, with its closed molecular geometry, naturally defines an intrinsic two-dimensional topological surface, we devised a simple and efficient numerical algorithm that could accurately describe the geometrically complex curved surfaces exhibited by flexible ring polymers. Figure 2.3.1.5a illustrates the main steps of the algorithm and how it allows for the extraction of the characteristic surfaces of the ring chains. Specifically, (i) we start to construct all the non-overlapping local triangular planes, each of which are constituted by three consecutive neighboring atoms (or beads) along the ring backbone; these triangles effectively depict the outermost ring surface. (ii)-(iv) We then apply the same procedure to successively build the inner surfaces of the ring in a step-by-step manner by forming new triangles with the remaining active atoms (which define a new inner closed-loop), excluding the middle (apex) atoms of the previous triangles. Here, to accurately extract the geometrical surfaces of the rings, ghost atoms were added in the middle of each line if the line connecting two neighboring atoms was longer than the original bond length. This procedure was repeated until only three atoms remained at the end to form the last triangle. This simple algorithm was numerically fast and could properly represent a variety of geometrically complex



surfaces formed by ring polymers, as exemplified in snapshot of Figure 2.3.1.5a.

From the constructed ring surface composed of numerous (locally-planar) small triangles, we obtained detailed geometric information of the ring in three-dimensional space, including the intrinsic surface shape and surface area. In particular, we could readily determine a set of the local normal vectors corresponding to each triangle over the entire ring surface. Here, we propose the average normal vector  $\mathbf{n}_{\text{avg}}$  of the entire surface as a useful physical measure that can effectively characterize the global orientation of a ring chain. The chain end-to-end vector  $\mathbf{R}_{\text{ete}} = \sum_{i=1}^{N_b} \mathbf{r}_i = N_b \left( \sum_{i=1}^{N_b} \mathbf{r}_i / N_b \right)$  with each bond vector  $\mathbf{r}_i$  and total number of local bonds  $N_b$  geometrically represents the average bond vector for the whole one-dimensional linear chain; while  $\mathbf{n}_{\text{avg}} = \sum_{i=1}^{N_s} \mathbf{n}_i = N_s \left( \sum_{i=1}^{N_s} \mathbf{n}_i / N_s \right)$  with each surface normal vector  $\mathbf{n}_i = \mathbf{r}'_{ia} \times \mathbf{r}'_{ib}$  for two bond vectors  $\mathbf{r}'_{ia}$  and  $\mathbf{r}'_{ib}$  constituting a triangle and the total number of local triangular surfaces  $N_s$  represents the average surface normal vector for the entire two-dimensional surface formed by a ring chain. Therefore, the  $\mathbf{n}_{\text{avg}}$  of the ring polymer that defines the two-dimensional characteristic surface is considered to intrinsically correspond with  $\mathbf{R}_{\text{ete}}$  for the linear polymer. Additionally, the magnitudes of  $\mathbf{r}_i$  and  $\mathbf{n}_i$  geometrically represent the local bond length and local triangular surface area ( $=|\mathbf{n}_i|/2$ ), respectively. We demonstrate that these surface properties are very useful for analyzing the fundamental structural and dynamical characteristics of ring polymers under flow conditions.

Next, we analyze the basic structural characteristics of the surface orientation and stretch for ring systems under shear flow. For an in-depth understanding of the fundamental aspects of actual ring polymers, we first set up a simple ‘toy model’ with a fixed two-dimensional flat square surface comprising four beads and rigid rods, simply mimicking a closed-loop geometry of ring polymers. This model was analyzed by applying free-draining (without EV and HI) bead-rod BD simulations. From the BD simulations, it can be clearly seen that the rigid surface tends to lie down preferentially in the  $xz$ -plane. Furthermore, the simulations without random thermal noise show that the most stable position of the two-dimensional surface is the lying position in the  $xz$ -plane, except for certain special initial surface orientations. While the geometric surface formed by the actual flexible ring polymers is generally curved and much more complex, their fundamental orientational characteristics are considered to be essentially similar to those of the aforementioned rigid structure.

This was confirmed by the results for the projected areas of the curved ring surface for each system, i.e.,  $A_{xy}$  on the  $xy$ -plane,  $A_{yz}$  on the  $yz$ -plane, and  $A_{xz}$  on the  $xz$ -plane in Figure 2.3.1.5b. The total surface area  $A_t$  of the ring could become significantly larger for actual ring polymers with increasing shear rate. This is because the flexible ring chains tend to be stretched and expand from their equilibrium coiled conformations. Therefore, we analyzed each projected area normalized by  $A_t$  for ring systems, in

comparison with the toy model which had a constant  $A_t$ . Notably, both the dilute and melt ring systems exhibited rapid overall increasing and decreasing behaviors for  $\langle A_{xz} / A_t \rangle$  and  $\langle A_{xy} / A_t \rangle$ , respectively, as the flow strength increased. This behavior by the actual ring polymers is fully consistent with that of the toy model, indicating essentially the same fundamental orientational characteristics (preferentially lying in the  $xz$ -plane) of the ring surface under shear flow. However, the degree of  $\langle A_{xz} / A_t \rangle$  and  $\langle A_{xy} / A_t \rangle$  variation appears to be somewhat smaller for actual systems compared with the toy model. This observation in real ring polymers can be attributed to local surface fluctuations in association with many local loops that protrude in the velocity-gradient ( $y$ )-direction along their flexible backbone. We further notice a larger  $\langle A_{xy} / A_t \rangle$  and smaller  $\langle A_{yz} / A_t \rangle$  for the ring melt compared with the dilute ring system in the intermediate-to-strong flow regime. This can be closely associated with the higher degree of ring polymer center-loop tumbling dynamics (via strong intermolecular collisions) in the melt relative to a dilute solution. Additionally, Figure 2.3.1.5c shows the ratio between  $\langle A_{xy} \rangle$  and  $\langle A_{xz} \rangle$  representing the degree of surface orientation relative to the kinematically stable  $xz$ -plane under shear flow as a function of the applied flow strength. While both the dilute and melt ring systems show an overall decreasing behavior of  $\langle A_{xy} \rangle / \langle A_{xz} \rangle$  with increasing shear rate, which is consistent with the toy model, it is weaker for the former compared with the latter. This is because of the significant dynamical role of local loops in actual ring polymers, resulting in considerable surface fluctuations. It was additionally observed that the melt system exhibits a lower overall degree of surface alignment parallel to the  $xz$ -plane than the dilute system in the intermediate-to-strong flow regime.

As a distinctive structural feature of ring polymers, we observe that  $\langle G_{zz} \rangle / \langle G_{zz} \rangle_{\text{eq}}$  of the gyration tensor  $\mathbf{G}$  is considerably larger for a ring polymer than for a linear polymer for both dilute and melt systems in the intermediate-to-strong flow regime (Figure 2.3.1.5d). Note that the gyration tensor can be defined as  $G_{\alpha\beta} = \frac{1}{N} \sum_{i=1}^N (\mathbf{r}_{i,\alpha} - \mathbf{r}_{c,\alpha})(\mathbf{r}_{i,\beta} - \mathbf{r}_{c,\beta})$ , where  $\mathbf{r}_i$ ,  $\mathbf{r}_c$ , and  $N$  denote the position of particle  $i$ , the center of mass of the chain, and the number of particles per chain, respectively. In contrast with the overall monotonically decreasing tendency of  $\langle G_{zz} \rangle / \langle G_{zz} \rangle_{\text{eq}}$  with increasing shear rate for the linear system, ring systems exhibit a plateau region for  $\langle G_{zz} \rangle / \langle G_{zz} \rangle_{\text{eq}}$  in certain intermediate flow regimes and even exhibit an increasing behavior under higher flow strengths. Further, the dilute ring systems also possess significantly larger values of  $\langle G_{zz} \rangle / \langle G_{zz} \rangle_{\text{eq}}$  in comparison to the ring melt

systems in the whole flow regime. This result for dilute ring systems appears to be consistent with the existing experimental<sup>59</sup> and numerical<sup>63-66</sup> observations of hydrodynamic inflation in the neutral ( $z$ -)direction for a diluted ring chain under shear and planar elongational flows. The rather large values for  $G_{zz}$  as well as  $A_{yz}$  and  $A_{xz}$  for the ring polymers are expected to have a significant rheological influence. For instance, these geometrical characteristics would generally promote the degree of transient structural coupling between chains during their rotational and tumbling dynamics in shear flow, which results in an effective increase of momentum transfer and correlation between chains, thereby enhancing the overall stress (or viscosity) of the melt system. This has been confirmed by the lower shear-thinning behavior of the ring melt in comparison with the linear melt in the intermediate-to-strong flow regime.

### Synergistic role of ring geometry and short branches in bulk polymer rheology

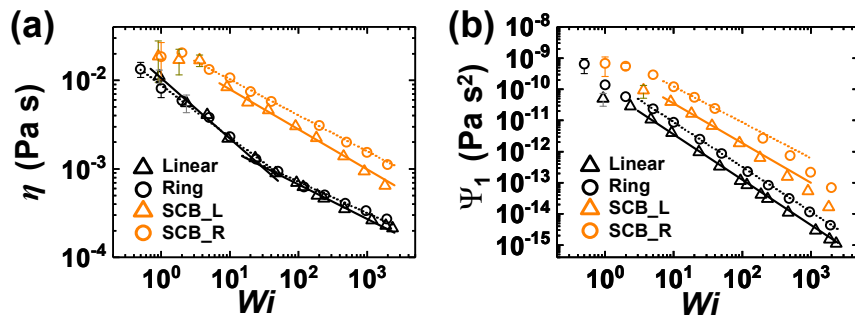


**Figure 2.3.1.6.** (a) The steady state shear viscosity  $\eta$  and (b) the first normal stress coefficient  $\Psi_1$  as a function of the Weissenberg number  $Wi$  for the  $C_{128}H_{258}$  linear (Linear; black triangles),  $C_{400}H_{800}$  ring (Ring; black circles),  $C_{178}H_{358}$  SCB linear (SCB\_L; orange triangles), and  $C_{565}H_{1130}$  SCB ring (SCB\_R; orange circles) PE melt systems. The error bars are smaller than the size of the symbols unless otherwise specified. The slopes in (a) and (b) were calculated by fitting the  $\eta$  and  $\Psi_1$  in the shear-thinning regime through simple power-law expression of the forms  $\eta \sim Wi^{-b_1}$  and  $\Psi_1 \sim Wi^{-b_2}$  with slopes  $b_1$  and  $b_2$  (Linear; black solid line, Ring; black dotted line, SCB\_L; orange solid line, and SCB\_R; orange dotted line).

To help interpret the general behavior of rheological characteristics for the short-chain branched (SCB) ring polyethylene (PE) melts in a view of the synergistic role of ring geometry and short branches, we performed comprehensive analysis on shear rheology in connection with underlying fundamental molecular mechanisms via direct comparison with linear, ring, SCB linear, and SCB ring polymers. In Figure 2.3.1.6, we present the macroscopic rheological properties of shear viscosity  $\eta$  and first normal stress coefficient  $\Psi_1$ . Figure 2.3.1.6a shows the results of shear viscosity  $\eta$  as a function of Weissenberg number  $Wi$  for the  $C_{128}H_{258}$  linear (Linear),  $C_{400}H_{800}$  ring (Ring),  $C_{178}H_{358}$  SCB linear (SCB\_L), and  $C_{565}H_{1130}$  SCB ring (SCB\_R) PE melt systems. It is noted that we decided to compare  $C_{400}H_{800}$  ring PE system with unentangled  $C_{128}H_{258}$  linear PE system to avoid the significant effect of interchain entanglements. As seen in Figure 2.3.1.6a, all four PE systems exhibit a typical shear-thinning

behavior as  $Wi$  increases ( $Wi > 1$ ) with respect to the molecular characteristics of chain orientation and stretching toward the flow ( $x$ -)direction. However, the detailed shear-thinning behavior of each system has qualitatively different tendencies depending on their molecular architectures and flow strengths according to the simple power-law expression of forms  $\eta \sim Wi^{-b_1}$ . In case of the pure linear PE system (Linear), it shows two different slopes  $b_1$  of  $0.68 \pm 0.05$  and  $0.39 \pm 0.02$  for  $\eta$  in the intermediate ( $1 < Wi < 20$ ) and strong flow ( $40 < Wi < 2000$ ) regimes, respectively. In the intermediate flow regime, the linear system displays the shear-thinning behavior generally attributed to the chain orientation and stretching with respect to the applied flow strength. In the strong flow regime, the chain orientation and stretching of molecular chains are nearly saturated and their rheological influences would be negligible. Instead, in the strong flow regime, the degree of intermolecular collision significantly increases as another essential molecular characteristics due to the flow-induced collisions and intensive chain rotation dynamics, which effectively contribute the stress of polymers. Therefore, the shear-thinning behavior is generally weaker (i.e., less shear-thinning  $\approx$  decrease of slope  $b_1$ ) than the intermediate flow regime.

Compared to their linear analogues,  $\eta$  for the pure ring system (Ring) shows qualitatively similar tendencies on the overall flow strengths, however the detailed degree of shear-thinning (i.e., the value of slope  $b_1$ ) is slightly smaller than those of the linear system; two different slopes  $b_1$  of  $0.59 \pm 0.05$  and  $0.35 \pm 0.03$  for  $\eta$  in the intermediate ( $0.5 < Wi < 20$ ) and strong flow ( $40 < Wi < 2000$ ) regimes, respectively. Although the employed linear and ring systems in this study have different molecular weights, the lower degree of shear-thinning behavior of the ring system than that of the linear system is qualitatively consistent with the results in previous studies simulated in the condition of the same backbone length at 78 and 400 carbon atoms for linear and ring systems. The lower degree of shear-thinning behavior for the ring system than their linear analogous is generally attributed to the compact structure and less degree of chain orientation due to the intrinsic closed-loop geometry [e.g., the inflation of ring toward neutral ( $z$ -)direction and the structure of the double strands].

In comparison with the pure linear and ring systems displaying two different degrees of shear-thinning behavior with respect to the applied flow strength, interestingly the SCB systems (SCB\_L and SCB\_R) apparently show one degree of shear-thinning behavior on overall flow strengths as described in Figure 2.3.1.6a; one slope  $b_1$  of  $0.46 \pm 0.02$  and  $0.41 \pm 0.02$  for SCB\_L ( $10 < Wi < 2000$ ) and SCB\_R ( $5 < Wi < 2000$ ), respectively. It should be noted that although SCB systems display one slope behavior of shear-thinning in both intermediate and strong flow regimes, it cannot imply that their structural and dynamical molecular characteristics are also same in these flow regimes. Thus, it is apparently obtained result due to the effect of short branches on bulk polymer rheology. As well known in recent studies, the short-chain branches generally execute the fast random thermal Brownian motions associated with their short characteristic relaxation time due to their very short chain length (e.g., 2, 4, and 6 carbon atoms in PE molecule). It indicates that their dynamics are practically unaffected by the external flow field. Therefore, short branches disturb the chain orientation and deformation of the backbone chain

against the applied flow field leading to more compact structures than their pure linear and ring analogues. As a result, as seen in Figure 2.3.1.6a (SCB\_L and SCB\_R), the SCB systems exhibit a lesser degree of shear-thinning behavior in association with the more compact and less deformed (stretched) structure than their pure linear and ring system in the intermediate flow regime. However, in the strong flow regime, the chain conformations of SCB PE melts are also nearly saturated and intermolecular collisions are also considered as a crucial role regardless of molecular architectures (i.e., fundamental molecular characteristics in the strong flow regime) resulting similar values of slope  $b_1$  for all four PE systems in this flow regime. That is, since SCB systems have less degree of shear-thinning (i.e., lower value of slope  $b_1$ ) due to the significant effect of the short branches at the chain backbone in the intermediate flow regime, SCB systems apparently show that they have one slope of shear-thinning on the overall flow strengths.

Furthermore, in contrast to pure linear and ring systems that have almost similar values of slope  $b_1$  and general tendencies even though they have different molecular weights, the SCB\_R system shows a significantly lesser degree of shear-thinning behavior and higher values of shear viscosity  $\eta$  rather than those of SCB\_L system. These features indicate that the synergistic effect of short-chain branches and ring geometric (closed-loop) backbone are pronounced on shear rheology inducing the less shear-thinning behaviors with respect to the applied flow field.

As another interesting rheological feature, the first normal stress coefficient  $\Psi_1$  as a function of  $Wi$  for the Linear, Ring, SCB\_L, and SCB\_R is obtained in Figure 2.3.1.6b. All four PE melt systems also exhibit a typical shear-thinning behavior of  $\Psi_1$  with power-law expression of forms  $\Psi_1 \sim Wi^{-b_2}$ ; slope  $b_2$  of  $1.45 \pm 0.02$ ,  $1.44 \pm 0.01$ ,  $1.28 \pm 0.05$ , and  $1.14 \pm 0.1$  for Linear ( $5 < Wi < 2000$ ), Ring ( $5 < Wi < 2000$ ), SCB\_L ( $5 < Wi < 1000$ ), and SCB\_R ( $5 < Wi < 1000$ ; orange dotted line), respectively. One can easily identify that (i) SCB systems exhibit higher values of  $\Psi_1$  than those of pure linear and ring systems and (ii) SCB systems apparently show two slope behaviors of shear-thinning of  $\Psi_1$  [i.e., the slope  $b_2$  fitting in the intermediate flow regime cannot match in the strong flow regime ( $Wi > 1000$ )] in contrast to the one slope behavior of  $\eta$ . These features are reasonably consistent results of shear-thinning behavior of  $\eta$  in Figure 2.3.1.6a. That is, in case of  $\Psi_1$ , less shear-thinning behavior for SCB systems due to the effect of short chains at the chain backbone apparently induce two slope behaviors of  $\Psi_1$  for SCB systems in contrast to one slope behavior of  $\eta$  for pure linear and ring systems.

### 2.3.2 Shear rheology of interfacial polymers

Here, we analyzed the degree of slip ( $d_s$ ) for the confined polymeric system defined as  $d_s = 1 - \dot{\gamma}_{\text{real}} / \dot{\gamma}_{\text{ideal}} = V_s / V_w$ , where  $V_s$  is the total slip velocity occurring at the top and bottom walls and  $V_w$  is the applied velocity of the moving top wall toward the flow direction in shear flow. Whereas the ideal (nominal) shear rate  $\dot{\gamma}_{\text{ideal}} = V_w / H$  is based on the assumption of the no-slip boundary condition with  $H$  being the box dimension in the velocity gradient (y-)direction, the real shear rate  $\dot{\gamma}_{\text{real}} = (V_w - V_s) / H$  accounts for a finite slip at the boundary walls. Practically, we evaluated the value of  $\dot{\gamma}_{\text{real}}$  for the  $d_s$  of the confined systems as follows: the y-dimension of the simulation box (i.e.,  $H$ ) was divided into several bins with a constant interval, and the streaming velocity in the flow direction for each bin was calculated by averaging the  $x$  component of velocity for all atoms belonging to that bin. Then, the final streaming velocity was obtained by applying a fifth-order polynomial fitting to the velocity data measured in each MD step and averaging the resulting velocity profile over a sufficiently long system trajectory.  $\dot{\gamma}_{\text{real}}$  was then calculated by applying linear regression to the average streaming velocity data along the velocity gradient direction. We also note that the degree of slip is directly related to the standard slip length ( $L_s$ ) by  $d_s^{-1} = 1 + \tilde{L}_s^{-1}$  with  $\tilde{L}_s \equiv L_s / H$ .

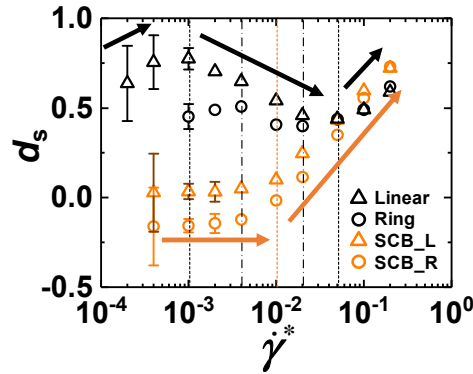


**Figure 2.3.2.1.** Degree of slip ( $d_s$ ) as a function of the reduced shear rate  $\gamma^* \equiv \dot{\gamma} \sqrt{m\sigma^2 / \epsilon}$  for the simulated  $C_{128}H_{258}$  linear (Linear; black triangles),  $C_{128}H_{256}$  ring (Ring; black circles),  $C_{178}H_{358}$  SCB linear (SCB\_L; orange triangles), and  $C_{178}H_{356}$  SCB ring (SCB\_R; orange circles) PE melt systems. The vertical black dashed lines (Linear), black dash-dotted lines (Ring), and orange dashed line (SCB\_L and SCB\_R) separate the characteristic flow regimes with respect to  $d_s$  for each system. It is noted that while the linear and ring polymers exhibit three distinct characteristic  $d_s$  regimes (increasing, decreasing, and increasing) as a function of shear rate, the SCB systems show almost constant behavior of  $d_s$  in the weak and intermediate flow regimes and increasing behavior of  $d_s$  in the strong flow regime. The error bars are smaller than the size of the symbols unless otherwise indicated.

Figure 2.3.2.1 presents the variation of the degree of slip for the simulated linear  $C_{128}H_{258}$ , ring

$C_{128}H_{256}$ , SCB linear  $C_{178}H_{358}$ , and SCB ring  $C_{178}H_{356}$  PE melts with respect to the applied shear rate over a wide range of flow strengths for the confined systems. The pure linear and ring melts exhibit three distinct characteristic  $d_s$  regimes with respect to the shear rate, i.e., an increasing, decreasing, and increasing behavior of  $d_s$  in the weak, intermediate, and strong flow regimes, respectively. In contrast, the SCB linear and SCB ring melts display almost constant behavior of  $d_s$  in the weak-to-intermediate flow regimes, followed by a rapid increase of  $d_s$  in the strong flow regime. To understand these distinctive slip behaviors of  $d_s$  for each system, it is essential to examine the fundamental molecular mechanisms of polymer chains at interfaces as a function of the applied shear rate by considering the dynamical influences of the external flow field and polymer–wall interactions.

Figure 2.3.2.2 depicts the characteristic molecular mechanisms for each polymer system in the three representative (weak, intermediate, and strong) flow regimes. To systematically understand the influence of the ring and short-chain branches on the interfacial chain dynamics, we illustrate the mechanisms of the linear polymer as basis.

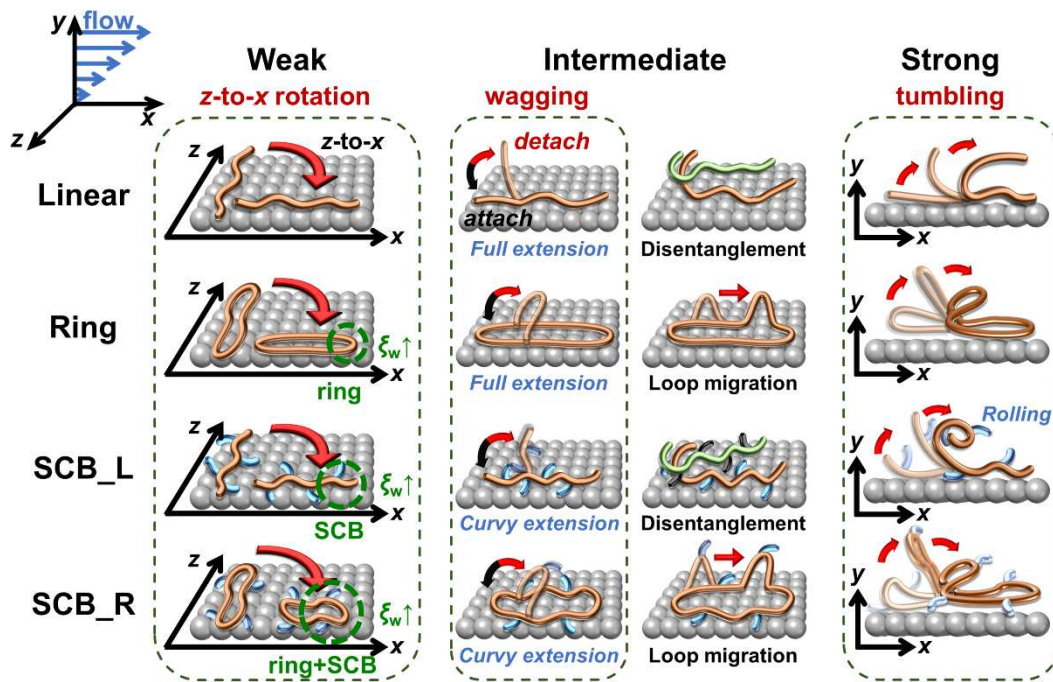


**Figure 2.3.2.2.** Schematic description of the characteristic molecular mechanisms for the interfacial linear, ring, SCB linear, and SCB ring polymers in the three representative (weak, intermediate, and strong) flow regimes. These mechanisms underlie the general behavior of the interfacial slip ( $d_s$ ) for each system.  $\xi_w$  denotes the polymer-wall friction coefficient.

In the weak flow regime, the applied shear force induces the interfacial linear chains to undergo z-to-x chain rotation while residing in the  $xz$ -plane, and the degree of chain alignment in the flow direction increases as the shear rate increases. This effectively reduces the dynamic friction of polymer

chains moving against the wall in the flow direction, thereby increasing the degree of slip. The ring polymer also exhibits a similar in-plane  $z$ -to- $x$  rotation, enhancing the interfacial slip. However, in comparison to the linear polymer, the ring polymer has a relatively larger chain dimension in the neutral ( $z$ -)direction owing to its intrinsic closed-loop molecular geometry, which promotes the dynamic friction of ring chains against the wall. This leads to a relatively smaller  $d_s$  value and less pronounced increase in  $d_s$  for the ring polymer in the weak flow regime in comparison to the linear analogue, as observed in Figure 2.3.2.1.

Looking into the effect of short-chain branching, the SCB linear polymer similarly exhibits  $z$ -to- $x$  chain rotation, thus reducing the overall interfacial dynamic friction and enhancing the wall slip. However, in contrast to the general alignment of the chain backbone in the flow direction, the short branches tend to be oriented rather perpendicular (i.e., aligned in the neutral direction) than parallel to the backbone owing to their bonded and nonbonded intramolecular LJ interactions with the neighboring backbone atoms around the branch points. This orientational tendency of short-chain branches along the  $z$ -direction effectively increases the polymer–wall friction, diminishing the interfacial slip. These two contrasting contributions between the backbone and short branches cancel each other out to result in a nearly constant behavior of  $d_s$  in the weak flow regime for the SCB linear polymer. We further note that the short branches have intrinsically fast random Brownian kinetics owing to their very short characteristic relaxation time scale (e.g.,  $\sim 0.06$  ns for  $C_5H_{12}$  at  $T = 450$  K and  $P = 1$  atm), and thus their dynamics are practically unaffected by the external flow field. Such fast random movements of short branches along the chain backbone constantly disturb the overall chain conformation and tend to diminish the degree of structural deformation of the polymer chains in response to the applied flow. This further facilitates the overall chain dimension of SCB polymers in the neutral direction.

By combining the respective influences of the ring topology and short-chain branching on the interfacial dynamics, we can reliably predict the general behavior of  $d_s$  for the SCB ring polymer. As mentioned above, the ring polymer, owing to its closed-loop topology, has a larger chain dimension in the neutral direction in comparison to the linear analogue. Furthermore, the fast random motions of the highly mobile short branches along the backbone constantly disturb the overall chain conformation, leading to lesser degrees of chain stretch and orientation along the flow direction and also a relatively larger chain dimension along the neutral direction. Thus, both the ring geometry and short-chain branching are expected to diminish the overall chain extension and alignment in the flow direction and increase the chain dimension in the neutral direction, synergistically enhancing the dynamic friction of interfacial chains moving against the wall. We therefore consider that the SCB ring polymer would exhibit significantly lower values of  $d_s$  in the weak flow regime in comparison to the other (linear, ring, and SCB linear) polymers, which is confirmed by the results shown in Figure 2.3.2.1.

Let us now examine the slip behavior of each polymer system in the intermediate flow regime.



Two representative molecular mechanisms were identified for the interfacial linear polymer in this regime: (i) an out-of-plane wagging mechanism [i.e., repetitive motions of the (outer) parts of the interfacial chains between detachment from the wall due to the external flow field and attachment to the wall due to the attractive polymer–wall interaction] and (ii) a disentanglement mechanism between the interfacial chains and nearby surrounding bulk chains via chain alignment and stretch along the flow direction. These two molecular processes effectively mitigate the movement of interfacial chains at the wall in the flow direction, resulting in an overall decreasing tendency of  $d_s$  for the linear and ring polymers in the intermediate flow regime. Notably, interfacial ring polymers, in addition to the loop wagging mechanism, exhibit a loop migration dynamic mechanism where locally created loop segments can propagate along the chain toward the flow direction. Because the loops can be created locally and randomly along the ring chain via thermal Brownian motion, the applied flow field, and intermolecular collisions, the loop wagging and loop migration dynamics may occur at any position of the chain, which is in contrast to the case of the linear polymer for which the out-of-plane wagging mechanism commonly occurs near the chain ends. Furthermore, the loop migration mechanism facilitates the movement of the whole ring chain in the flow direction and thus enhances the polymer slip at the wall. Also, the closed-loop topology of ring chains results in relatively fewer entanglement interactions compared to linear chains. These two factors together lead to a smaller decrease in  $d_s$  for the ring polymer compared to the linear polymer in the intermediate flow regime.

In contrast, both the SCB linear and SCB ring polymers exhibit nearly constant behavior for with respect to the shear rate throughout the weak and intermediate flow regimes. As mentioned previously, the highly mobile short branches make the overall chain structure more compact and less deformed (with highly curvy backbone structures) against the applied flow. This structural feature entails smaller entanglement interactions between chains and less variation in the degree of entanglement with respect to the flow strength, ultimately weakening the degree of the out-of-plane wagging and disentanglement mechanisms and consequently affording the apparent constant behavior of  $d_s$  for the SCB polymers.

In the strong flow regime, the external flow field is sufficiently strong to overcome the attractive polymer–wall interactions and cause intensive dynamical collisions between interfacial chains and the wall. This leads the interfacial chains to frequently detach from the wall and undergo irregular (chaotic) chain rotation and tumbling dynamics. This dynamic feature underlies a rapid increase in the degree of slip in this flow regime for all of the polymer systems.

It is interesting to note that whereas the tumbling dynamics occurs exclusively with the chain ends for the linear polymer, it can occur with any local loop(s) along the chain in the case of the ring polymer. This fact leads to two distinct types of tumbling mechanism: end-loop tumbling and center-loop tumbling. The end-loop tumbling mechanism is induced by the local loops situated near the ends

(outermost parts) of the stretched ring backbone along the flow direction, which is essentially similar to the typical end-over-end tumbling mechanism of the linear polymer. In contrast, the center-loop tumbling mechanism is driven by the loops located in the middle of the stretched ring backbone. Therefore, whereas end-loop tumbling practically occurs in the shear or flow-gradient ( $xy$ -)plane, the center-loop mechanism exhibits a diagonal chain rotation lying through both the  $xy$ - and  $yz$ -planes. These dynamic mechanisms were observed for both pure ring and SCB ring polymers at the interface under strong flow fields (specific quantification of the individual loop-tumbling mechanisms will be presented later).

Another interesting feature is that the interfacial SCB linear polymer exhibits not only the hairpin-like end-over-end tumbling behavior (similar to the linear polymer) but also additional distinct mechanisms such as head-roll and tail-roll tumbling dynamics, which is essentially caused by the short branches forming the compact head or tail parts along the chain backbone during the tumbling event. However, such rolling mechanisms were rarely observed in the case of the SCB ring polymer studied here. This is attributed to the relatively larger chain dimension along the neutral direction for the SCB ring polymer compared to the corresponding SCB linear polymer in addition to the rather double-stranded stretched ring conformations at strong flow fields, both of which may have effectively impeded the whole chain rolling along the flow direction (additionally, the  $C_{128}$  backbone length of the present  $C_{178}H_{356}$  SCB ring PE might not be sufficiently long to facilitate chain rolling). Also important is that the short branches promote the interfacial chain detachment from the wall by constantly disturbing the chain conformation via their fast random motions. This leads to a steeper increasing behavior of  $d_s$  in the strong flow regime for both SCB linear and ring polymers in comparison to the corresponding pure linear and ring polymers.

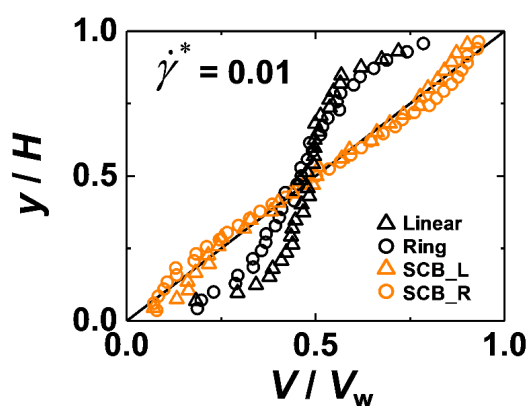


**Figure 2.3.2.3.** Streaming velocity profiles (normalized by the applied wall velocity  $V_w$ ) along the velocity gradient direction at a certain intermediate shear rate for the simulated  $C_{128}H_{258}$  linear (black triangles),  $C_{128}H_{256}$  ring (black circles),  $C_{178}H_{358}$  SCB linear (orange triangles), and  $C_{178}H_{356}$  SCB ring (orange circles) PE melts. The solid line represents the ideal streaming velocity profile assuming the no-slip boundary condition.

Figure 2.3.2.3 displays the steady-state streaming velocity profiles in the flow direction along the velocity gradient direction for the four polymer systems at an intermediate flow strength. In general, the nonlinearity of the velocity profile for a polymeric material is associated with the degree of interfacial slip. As noted earlier,  $\dot{\gamma}_{\text{real}}$  was calculated by applying linear regression to the streaming velocity data along the  $y$ -direction. Clearly, the pure linear and ring polymers exhibit a noticeable deviation from the ideal velocity profile (i.e., assuming the no-slip boundary condition) due to finite slip at the walls. Interestingly, the corresponding SCB linear and ring systems at the same shear rate display velocity profiles rather close to the ideal one ( $d_s \approx 0$ ), indicating apparently small interfacial slip. This behavior results from the enhanced polymer–wall friction due to the highly mobile short branches. Furthermore, owing to the additional wall friction caused by its closed-loop geometry, the SCB ring polymer exhibits even smaller interfacial slip than the SCB linear polymer.

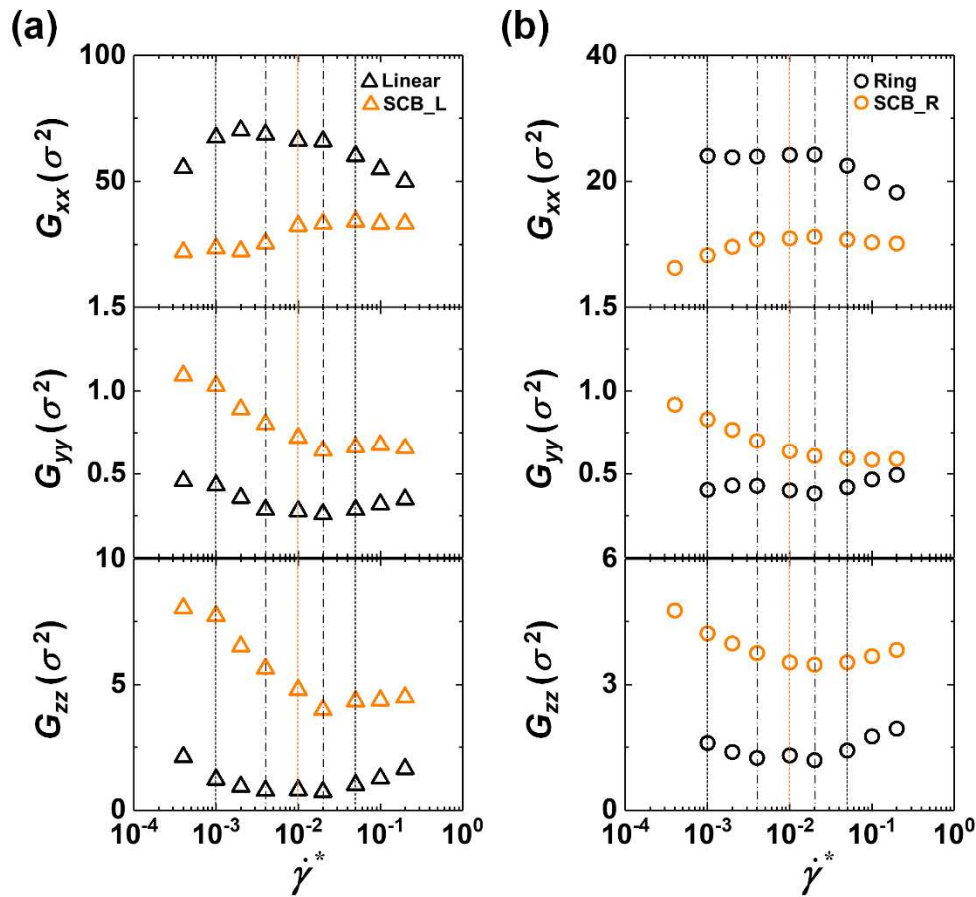


**Figure 2.3.2.4.** The  $xx$ ,  $yy$ , and  $zz$  components of the gyration tensor  $\mathbf{G}$  for the interfacial chains whose center-of-mass is located within a distance of  $2.5 \sigma$  from the wall for the (a)  $C_{128}H_{258}$  linear (black triangles) and  $C_{178}H_{358}$  SCB linear (orange triangles) and (b)  $C_{128}H_{256}$  ring (black circles) and  $C_{178}H_{356}$  SCB ring (orange circles) systems as a function of the applied shear rate. To allow comparison with the pure ring and linear systems, only the chain backbone, excluding the short branches, was considered in the calculation of  $\mathbf{G}$  for the SCB systems. The symbols and vertical lines have the same meaning as in Figure 2.3.2.1. The error bars are smaller than the size of the symbols unless otherwise indicated.

To further understand the interfacial characteristics in conjunction with the dynamic mechanisms, we analyzed the structural properties of the interfacial chains with centers of mass located within a distance of  $2.5 \sigma$  from the wall. Figure 2.3.2.4 presents the  $xx$ -,  $yy$ -, and  $zz$ -components of the gyration tensor  $\mathbf{G}$  of the interfacial chains for each system as a function of the applied flow strength. It should be noted that to examine the influence of short-chain branching on the overall chain structure, only the chain backbone (excluding the short branches) was included in the calculation of  $\mathbf{G}$  for the SCB polymers. First, as the shear rate increases in the weak flow regime, the linear polymer exhibits an increasing behavior of  $G_{xx}$  (which approaches a plateau value) and a decreasing behavior of both  $G_{yy}$  and  $G_{zz}$ . This is directly related to the  $z$ -to- $x$  rotation mechanism of the interfacial chains with their decreased  $y$  dimension via chain alignment and stretch in the flow direction. Upon further increasing the flow strength to the intermediate flow regime,  $G_{xx}$  shows almost constant behavior while both  $G_{yy}$  and  $G_{zz}$  continue to decrease until reaching a minimum value. These features can be understood by considering the aforementioned out-of-plane wagging and disentanglement mechanisms of the interfacial chains in the intermediate flow regime. Both mechanisms lead to significant suppression of the rotation and tumbling dynamics for the interfacial chains moving away from the wall. In the strong flow regime, as the shear rate increases,  $G_{xx}$  appears to rapidly decrease, whereas both  $G_{yy}$  and  $G_{zz}$  display a gradual increase. This is directly associated with the irregular rotation and tumbling dynamic mechanism of the interfacial chains via their strong dynamical collisions with the wall, which facilitates the detachment of the interfacial chains from the wall and their frequent movement toward the bulk region. Overall similar behavior is exhibited by the ring polymer, which, however, owing to its intrinsic closed-loop molecular geometry, shows somewhat smaller variation in each component ( $G_{xx}$ ,  $G_{yy}$ , and  $G_{zz}$ ) with respect to the flow strength compared to the linear polymer. It is also noted that the ring topology gives rise to an increase in  $G_{zz}$  and a decrease in  $G_{yy}$ .

In contrast, the SCB linear and ring polymers exhibit increasing behavior of  $G_{xx}$  and decreasing behavior of  $G_{yy}$  and  $G_{zz}$  throughout the weak-to-intermediate flow regimes, with all components remaining almost constant in the strong flow regime. Furthermore, the SCB polymers display a significant reduction in  $G_{xx}$  and increase in  $G_{yy}$  and  $G_{zz}$  in comparison to the corresponding pure linear and ring polymers. This feature is directly associated with the fact that the structural disturbance by the fast random motions of the short branches results in highly curvy backbone structures and lesser degrees of chain stretch and alignment to the flow direction for the SCB polymers.

It can be summarized that (i) the closed-loop ring geometry tends to reduce both  $G_{xx}$  and  $G_{yy}$  and promote  $G_{zz}$  and (ii) short-chain branching tends to reduce  $G_{xx}$  and promote both  $G_{yy}$  and  $G_{zz}$ .

## 2.4 Conclusion

In this study, the nonlinear rheological properties for linear PE melts (reflecting substantial deformation of polymer chains under intermediate-to-strong flow fields) were closely examined with respect to the following molecular characteristics: (i) chain orientation, (ii) stretching, (iii) disentanglement, (iv) intermolecular collision, and (v) end-over-end tumbling dynamics. Here, properties (i)–(iii) conform to the well-known polymer kinetic theory.<sup>1,2</sup> Through a detailed analysis of the variations in the molecular characteristics in response to the applied shear rate, we propose scaling expressions for the shear viscosity  $\eta$  and the first normal stress coefficient  $\Psi_1$  for unentangled and entangled linear PE systems with respect to those molecular variables. Comparing the  $Wi$  dependence of the structural parameters (defined for the whole chain backbone and/or entanglement strand) and rheological properties, we examine the scaling of those properties with respect to the structural parameters. Specifically, in the intermediate flow regime, we find scaling relationships for the viscosity  $\eta$  and the first normal stress difference  $\Psi_1$  with respect to the well-known fundamental molecular characteristics in polymer rheology such as the chain orientation, chain stretch, and interchain entanglement: (i)  $\eta \sim \theta^{\alpha_1} R^2$  and  $\Psi_1 \sim \theta^{\alpha_2} R^2$  with  $\alpha_1 = (1.5–1.7)$  and  $\alpha_2 = (3.2–3.6)$  for unentangled melts and (ii)  $\eta \sim \theta_{es}^{\alpha_1} Z^{\gamma_1} d_{es}^2$  and  $\Psi_1 \sim \theta_{es}^{\alpha_2} Z^{\gamma_2} d_{es}^2$  with  $\gamma_1 = (3.8–4.0)$  and  $\gamma_2 = (2.1–2.4)$  for entangled melts. Here,  $\theta$  ( $\theta_{es}$ ),  $R$ ,  $Z$ , and  $d_{es}$  are the average chain orientation angle (that of entanglement strand), the mean chain end-to-end distance, the average number of interchain entanglements, and the average length of an entanglement strand, respectively. While the C<sub>400</sub> and C<sub>600</sub> PE melts employed in this study are rather short and only mildly entangled systems, we believe that the basic features of the scaling expressions deduced for those chains remain valid for longer, strongly entangled chains within statistical uncertainties. Nevertheless, considering the rheological influence of entanglement segments near the chain ends (e.g., the effect of the contour length fluctuations in the tube theory<sup>1</sup>), which is particularly important for rather weakly entangled melt systems, the scaling exponent for the  $Z$ -dependence reported here may change slightly and approach gradually an asymptotic value as the chain length increases to highly entangled polymer melts. Furthermore, our proposed scaling relationships may be adapted to entangled branched polymers with additional scaling component of the arm orientation and stretch at the junction points along the chain backbone whose scaling behavior is to be the same as that of entangled linear polymers. Under moderately strong flow, those relationships may serve as a supplement (or substitute) for SOR which has a rigid molecular basis under slow flow. In the strong flow regime, the above scaling expressions become invalid and another empirical rheological scaling is found in terms of the characteristic rotational time  $\tau_{rot}$  as the representative dynamic variable to accommodate intermolecular collisional effects: (iii)  $\eta \sim \tau_{rot}^{\delta_1}$  and  $\Psi_1 \sim \tau_{rot}^{\delta_2}$  with  $\delta_1 = (0.5–0.6)$  and  $\delta_2 = (1.8–2.0)$  for both unentangled and entangled systems. The proposed scaling

relationships in this study well described  $\eta$  and  $\Psi_1$  obtained from the NEMD simulations under intermediate flow, thereby allowing us to correlate  $\eta$  and  $\Psi_1$  with the molecular variables ( $\theta$ ,  $R$ ,  $Z$ , and  $d_s$ ), in particular the scalar orientational variable  $\theta$  in the experimental sense (of correlating rheological and structural data) explained earlier. Thus, those relationships are believed to serve as a supplement (or substitute) for the modified SOR under the intermediate flow.

Additionally, we carried out a comprehensive study on the intrinsic structural characteristics of ring polymers under shear flow with both dilute and melt conditions. Our analysis began with the advanced viewpoint that ring polymers intrinsically possess two-dimensional surface characteristics because of their closed-loop geometry, which is in contrast with the one-dimensional line characteristics of linear polymers. Based on this view, we introduced several representative physical measures that could effectively describe the structural and dynamical characteristics of ring polymers, such as the total and projected surface areas and the average normal vector  $\mathbf{n}_{\text{avg}}$  of the ring surface, which corresponds with the chain end-to-end vector  $\mathbf{R}_{\text{ete}}$  of a linear polymer. Knowing the variation of these surface measures in response to the applied flow was found to be very informative for analyzing the characteristic molecular dynamics mechanisms of ring chains. An efficient numerical scheme was also developed that allowed us to effectively describe the complex curved surface formed by flexible ring chains. Applying this algorithm, we could accurately measure the overall surface shape and total or projected areas. The obtained surface information was found to be very useful for analyzing the characteristic dynamic mechanisms of ring polymers under shear flow. This scheme can be further applied to extract the intrinsic geometrical characteristics for various ring-type polymers (e.g., tadpole-like polymers) and ring/linear blend systems. Furthermore, the numerical algorithm can be used to directly quantify the degree of penetration between different ring chains, thereby enabling a systematic analysis of the dynamical role of interchain penetration for ring melt systems; this has been an important (and rather controversial) rheological issue in the last decades.

Finally, we performed a comprehensive analysis of the interfacial structural and dynamical behavior of confined polymer melt systems possessing various molecular architectures (linear, ring, SCB linear, and SCB ring) under shear flow using atomistic NEMD simulations. We placed a particular focus on the combined rheological influence of the closed-loop ring geometry and short-chain branching on the general structure and dynamics of the interfacial chains. In doing so, we examined the degree of interfacial slip, the underlying characteristic molecular mechanisms, and the detailed chain conformations for interfacial chains with respect to their molecular architectures. In general, the interfacial linear and ring polymers exhibit three distinct characteristic regimes for the degree of slip ( $d_s$ ) with respect to the applied shear rate: an increasing, decreasing, and increasing behavior of  $d_s$  in the weak, intermediate, and strong flow regimes, respectively. In contrast, the interfacial SCB linear and SCB ring polymers display almost constant behavior of  $d_s$  throughout the weak and intermediate flow regimes followed by rapidly increasing behavior of  $d_s$  in the strong flow regime. To elucidate the

interfacial slip behavior, it is very informative to analyze the fundamental molecular mechanisms with respect to the three representative (weak, intermediate, and strong) flow regimes. In the weak flow regime, all of the interfacial polymers (linear, ring, SCB linear, and SCB ring) undergo  $z$ -to- $x$  chain rotation from the neutral direction to the flow direction, which effectively reduces the dynamic wall friction against chain movement along the flow direction. However, in comparison with its linear analogue, the ring polymer possesses a relatively longer chain dimension in the neutral direction owing to its intrinsic closed-loop geometry, which enhances the dynamic friction of the interfacial ring chains moving against the wall in the flow direction. In the case of the interfacial SCB polymers, whereas the main chain backbone becomes gradually aligned to the flow direction with increasing flow strength (thus decreasing the dynamic wall friction), the short branches tend to be oriented more perpendicular (i.e., aligned in the neutral direction) than parallel to the backbone (thus increasing the dynamic wall friction) in conjunction with their intrinsically fast random motions that are practically unaffected by the imposed flow fields. These two contrasting factors cancel each other out to result in almost constant in the weak flow regime for the interfacial SCB polymers. Furthermore, owing to its relatively larger chain dimension in the neutral direction associated with the ring topology, the SCB ring polymer exhibits the lowest degree of slip among all of the polymers. In respect to the overall chain dimension, the closed-loop ring topology tends to enhance  $G_{zz}$  but diminish both  $G_{xx}$  and  $G_{yy}$ , while short-chain branching tends to enhance both  $G_{yy}$  and  $G_{zz}$  but diminish  $G_{xx}$ .

## 2.5 References

1. Doi, M.; Edwards, S. F. *The Theory of Polymer Dynamics*; Oxford University Press: New York, 1986.
2. Bird, R. B.; Armstrong, R. C.; Hassager, O. *Dynamics of Polymeric Liquids*, Vol. 1: Fluid Mechanics, Vol. 2: Kinetic Theory, 2nd edition; Wiley-Interscience: New York, 1987.
3. Larson, R. G. *Constitutive equations for polymer melts and solutions*; Butterworths: Boston, 1988.
4. Morrison, Faith. A. *Understanding Rheology*; Oxford University Press: New York, 2001.
5. Schroeder, C. M.; Teixeira, R. E.; Shaqfeh, E. S. G.; Chu, S. Dynamics of DNA in the flow-gradient plane of steady shear flow: Observations and Simulations. *Macromolecules* **2005**, *38*, 1967-1978.
6. Teixeira, R. E.; Babcock, H. P.; Shaqfeh, E. S. G.; Chu, S. Shear thinning and tumbling dynamics of single polymers in the flow-gradient plane. *Macromolecules* **2005**, *38*, 581-592.
7. Teixeira, R. E.; Dambal, A. K.; Richter, D. H.; Shaqfeh, E. S. G.; Chu, S. The individualistic dynamics of entangled DNA in solution. *Macromolecules* **2007**, *40*, 2461-2476.
8. Costanzo, S.; Huang, Q.; Ianniruberto, G.; Marrucci, G.; Hassager, O.; Vlassopoulos, D. Shear and extensional rheology of polystyrene melts and solutions with the same number of entanglements. *Macromolecules* **2016**, *49*, 3925-3935.
9. Cui, S. T.; Cummings, P. T.; Cochran, H. D. Multiple time step nonequilibrium molecular dynamics simulation of the rheological properties of liquid n-decane. *J. Chem. Phys.* **1996**, *104*, 255.
10. Cui, S. T.; Gupta, S. A.; Cummings, P. T.; Cochran, H. D. Molecular dynamics simulations of the rheology of normal decane, hexadecane, and tetracosane. *J. Chem. Phys.* **1996**, *105*, 1214.
11. Kröger, M.; Hess, S. Rheological evidence for a dynamical crossover in polymer melts via nonequilibrium molecular dynamics. *Phys. Rev. Lett.* **2000**, *85*, 1128-1131.
12. Moore, J. D.; Cui, S. T.; Cochran, H. D.; Cummings, P. T. A molecular dynamics study of a short-chain polyethylene melt. I. Steady-state shear. *J. Non-Newtonian Fluid Mech.* **2000**, *93*, 83-99.
13. Kim, J. M.; Keffer, D. J.; Kröger, M.; Edwards, B. J. Rheological and entanglement characteristics of linear chain polyethylene liquids in planar Couette and planar elongational flows. *J. Non-Newtonian Fluid Mech.* **2008**, *152*, 168-183.
14. Kim, J. M.; Edwards, B. J.; Keffer, D. J.; Khomami, B. Dynamics of individual molecules of linear polyethylene liquids under shear: Atomistic simulation and comparison with a free-draining bead-rod chain. *J. Rheol.* **2010**, *54*, 283-310.
15. Baig, C.; Mavrantzas, V. G.; Kröger, M. Flow effects on melt structure and entanglement network of linear polymers: Results from a nonequilibrium molecular dynamics simulation study of a polyethylene melt in steady shear. *Macromolecules* **2010**, *43*, 6886-6902.



16. Dalal, I. S.; Hoda, N.; Larson, R. G. Multiple regimes of deformation in shearing flow of isolated polymers. *J. Rheol.* **2012**, *56*, 305-332.
17. Harasim, M.; Wunderlich, B.; Peleg, O.; Kröger, M.; Bausch, A. R. Direct observation of the dynamics of semiflexible polymers in shear flow. *Phys. Rev. Lett.* **2013**, *110*, 108302.
18. Nafar Sefiddashti, M. H.; Edwards, B. J.; Khomami, B. Individual chain dynamics of a polyethylene melt undergoing steady shear flow. *J. Rheol.* **2015**, *59*, 119-153.
19. Nafar Sefiddashti, M. H.; Edwards, B. J.; Khomami, B. Steady shearing flow of a moderately entangled polyethylene liquid. *J. Rheol.* **2016**, *60*, 1227-1244.
20. Nafar Sefiddashti, M. H.; Edwards, B. J.; Khomami, B. Individual molecular dynamics of an entangled polyethylene melt undergoing steady shear flow: Steady-state and transient dynamics. *Polymers* **2019**, *11*, 476.
21. Janeschitz-Kriegl, H. Polymer melt rheology and flow birefringence; Springer-Verlag: New York, 1983.
22. Baig, C.; Edwards, B. J.; Keffer, D. J. A molecular dynamics study of the stress-optical behavior of a linear short-chain polyethylene melt under shear. *Rheol. Acta* **2007**, *46*, 1171-1186.
23. Baig, C. Torsional linearity in nonlinear stress-optical regimes for polymeric materials. *ACS Macro Lett.* **2016**, *5*, 273-277.
24. de Gennes, P. G. Reptation of a polymer chain in the presence of fixed obstacles. *J. Chem. Phys.* **1971**, *55*, 572-579.
25. Fetters, L. J.; Loshe, D. J.; Richter, D.; Witten, T. A.; Zirkel, A. Connection between polymer molecular weight, density, chain dimensions, and melt viscoelastic properties. *Macromolecules* **1994**, *27*, 4639-4647.
26. McLeish, T. C. B. Tube theory of entangled polymer dynamics. *Adv. Phys.* **2002**, *51*, 1379-1527.
27. Lohse, D. J. The influence of chemical structure on polyolefin melt rheology and miscibility. *J. Macromol. Sci., Part C: Polym. Rev.* **2005**, *45*, 289-308.
28. Larson, R. G. The Structure and Rheology of Complex Fluids; Oxford University Press: New York, 1999.
29. Rubinstein, M.; Colby, R. H. Polymer Physics; Oxford University Press: New York, 2003.
30. Bird, R. B.; Armstrong, R. C.; Hassager, O. Dynamics of Polymeric Liquids, Vol. 1: Fluid Mechanics; Wiley-Interscience: New York, 1987.
31. Baig, C.; Mavrantzas, V. G. Tension thickening, molecular shape, and flow birefringence of an H-shaped polymer melt in steady shear and planar extension. *J. Chem. Phys.* **2010**, *132*, 014904.
32. Doi, M.; Edwards, S. F. The Theory of Polymer Dynamics; Oxford University Press: New York, 1986.
33. Watanabe, H. Viscoelasticity and dynamics of entangled polymers. *Prog. Polym. Sci.* **1999**, *24*, 1253-1403.

34. Kapnistos, M.; Lang, M.; Vlassopoulos, D.; Pyckhout-Hintzen, W.; Richter, D.; Cho, D.; Chang, T.; Rubinstein, M. Unexpected power-law stress relaxation of entangled ring polymers. *Nat. Mater.* **2008**, *7*, 997-1002.
35. Roovers, J. The melt properties of ring polystyrenes. *Macromolecules* **1985**, *18*, 1359-1361.
36. Halverson, J. D.; Lee, W. B.; Grest, G. S.; Grosberg, A. Y.; Kremer, K. Molecular dynamics simulation study of nonconcatenated ring polymers in a melt. I. Statics. *J. Chem. Phys.* **2011**, *134*, 204904.
37. Pasquino, R.; Vasilakopoulos, T. C.; Jeong, Y. C.; Lee, H.; Rogers, S.; Sakellariou, G.; Allgaier, J.; Takano, A.; Brás, A. R.; Chang, T.; Gooßen, S.; Pyckhout-Hintzen, W.; Wischnewski, A.; Hadjichristidis, N.; Richter, D.; Rubinstein, M.; Vlassopoulos, D. Viscosity of ring polymer melts. *ACS Macro Lett.* **2013**, *2*, 874-878.
38. Trabi, M.; Craik, D. J. Circular proteins-no end in sight. *Trends Biochem. Sci.* **2002**, *27*, 132-138.
39. Sanchez, T.; Kulic, I. M.; Dogic, Z. Circularization, photomechanical switching, and a supercoiling transition of actin filaments. *Phys. Rev. Lett.* **2010**, *104*, 098103.
40. Cremer, T.; Cremer, C. Chromosome territories, nuclear architecture and gene regulation in mammalian cells. *Nat. Rev. Genet.* **2001**, *2*, 292-301.
41. Halverson, J. D.; Smrek, J.; Kremer, K.; Grosberg, A. Y. From a melt of rings to chromosome territories: the role of topological constraints in genome folding. *Rep. Prog. Phys.* **2014**, *77*, 022601.
42. Brown, S.; Lenczycki, T.; Szamel, G. Influence of topological constraints on the statics and dynamics of ring polymers. *Phys. Rev. E* **2001**, *63*, 052801.
43. Arrighi, V.; Gagliardi, S.; Dagger, A. C.; Semlyen, J. A.; Higgins, J. S.; Shenton, M. J. Conformation of cyclics and linear chain polymers in bulk by SANS. *Macromolecules* **2004**, *37*, 8057-8065.
44. Tsolou, G.; Stratikis, N.; Baig, C.; Stephanou, P. S.; Mavrantzas, V. G. Melt structure and dynamics of unentangled polyethylene rings: Rouse theory, atomistic molecular dynamics simulation, and comparison with the linear analogues. *Macromolecules* **2010**, *43*, 10692-10713.
45. Vettorel, T.; Grosberg, A. Y.; Kremer, K. Statistics of polymer rings in the melt: a numerical simulation study. *Phys. Biol.* **2009**, *6*, 025013.
46. Rosa, A.; Everaers, R. Ring polymers in the melt state: the physics of crumpling. *Phys. Rev. Lett.* **2014**, *112*, 118302.
47. Cates, M.; Deutsch, J. Conjectures on the statistics of ring polymers. *J. Phys. (France)* **1986**, *47*, 2121-2128.
48. Obukhov, S. P.; Rubinstein, M.; Duke, T. Dynamics of a ring polymer in a gel. *Phys. Rev. Lett.* **1994**, *73*, 1263.
49. Milner, S. T.; Newhall, J. D. Stress relaxation in entangled melts of unlinked ring polymers. *Phys. Rev. Lett.* **2010**, *105*, 208302.

50. Grosberg, A. Y.; Nechaev, S. K.; Shakhnovich, E. I. The role of topological constraints in the kinetics of collapse of macromolecules. *J. Phys. (France)* **1988**, *49*, 2095-2100.
51. Sakaue, T. Statistics and geometrical picture of ring polymer melts and solutions. *Phys. Rev. E* **2012**, *85*, 021806.
52. Lang, M. Ring conformations in bidisperse blends of ring polymers. *Macromolecules* **2013**, *46*, 1158-1166.
53. Smrek, J.; Grosberg, A. Y. Minimal surfaces on unconcatenated polymer rings in melt. *ACS Macro Lett.* **2016**, *5*, 750-754.
54. Tsalikis, D. G.; Mavrantzas, V. G.; Vlassopoulos, D. Analysis of slow modes in ring polymers: Threading of rings controls long-time relaxation. *ACS Macro Lett.* **2016**, *5*, 755-760.
55. Smrek, J.; Kremer, K.; Rosa, A. Threading of unconcatenated ring polymers at high concentrations: double-folded vs time-equilibrated structures. *ACS Macro Lett.* **2019**, *8*, 155-160.
56. Schram, R. D.; Rosa, A.; Everaers, R. Local loop opening in untangled ring polymer melts: a detailed “Feynman test” of models for the large scale structure. *Soft Matter* **2019**, *15*, 2418-2429.
57. Yoon, J.; Kim, J.; Baig, C. Nonequilibrium molecular dynamics study of ring polymer melts under shear and elongation flows: A comparison with their linear analogs. *J. Rheol.* **2016**, *60*, 673-685.
58. Yan, Z. C.; Costanzo, S.; Jeong, Y.; Chang, T.; Vlassopoulos, D. Linear and nonlinear shear rheology of a marginally entangled ring polymer. *Macromolecules* **2016**, *49*, 1444-1453.
59. Li, Y.; Hsiao, K. W.; Brockman, C. A.; Yates, D. Y.; Robertson-Anderson, R. M.; Kornfield, J. A.; San Francisco, M. J.; Schroeder, C. M.; Mckenna, G. B. When ends meet: Circular DNA stretches differently in elongational flows. *Macromolecules* **2015**, *48*, 5997-6001.
60. Jeong, S.; Cho, S.; Kim, J. M.; Baig, C. Interfacial molecular structure and dynamics of confined ring polymer melts under shear flow. *Macromolecules* **2018**, *51*, 4670-4677.
61. Chen, W.; Chen, J.; An, L. Tumbling and tank-treading dynamics of individual ring polymers in shear flow. *Soft Matter* **2013**, *9*, 4312-4318.
62. Tsamopoulos, A. J.; Katsarou, A. F.; Tsalikis, D. G.; Mavrantzas, V. G. Shear rheology of unentangled and marginally entangled ring polymer melts from large-scale nonequilibrium molecular dynamics simulations. *Polymers* **2019**, *11*, 1194.
63. Hsiao, K. W.; Schroeder, C. M.; Sing, C. E. Ring polymer dynamics are governed by a coupling between architecture and hydrodynamic interactions. *Macromolecules* **2016**, *49*, 1961-1971.
64. Liebetreu, M.; Ripoll, M.; Likos, C. N. Trefoil knot hydrodynamic delocalization on sheared ring polymers. *ACS Macro Lett.* **2018**, *7*, 447-452.
65. Young, C. D.; Qian, J. R.; Marvin, M.; Sing, C. E. Ring polymer dynamics and tumbling-stretch transitions in planar mixed flows. *Phys. Rev. E* **2019**, *99*, 062502
66. Liebetreu, M.; Likos, C. N. Hydrodynamic inflation of ring polymers under shear. *Commun. Mater.* **2020**, *1*, 1-11.

67. O' Connor, T. C.; Ge, T.; Rubinstein, M.; Grest, G. S. Topological linking drives anomalous thickening of ring polymers in weak extensional flows. *Phys. Rev. Lett.* **2020**, *124*, 027801.
68. Huang, Q.; Ahn, J.; Parisi, D.; Chang, T.; Hassager, O.; Panyukov, S.; Rubinstein, M.; Vlassopoulos, D. Unexpected stretching of entangled ring macromolecules. *Phys. Rev. Lett.* **2019**, *122*, 208001.
69. Baig, C.; Edwards, B. J.; Keffer, D. J.; Cochran, H. D. A proper approach for nonequilibrium molecular dynamics simulations of planar elongational flow. *J. Chem. Phys.* **2005**, *122*, 114103.
70. Nosé, S. A molecular dynamics method for simulations in the canonical ensemble. *Mol. Phys.* **1984**, *52*, 255-268.
71. Hoover, W. G. Canonical dynamics: equilibrium phase-space distributions. *Phys. Rev. A* **1985**, *31*, 1695-1697.
72. Lees, A. W.; Edwards, S. F. The computer study of transport processes under extreme condition. *J. Phys. C: Solid State Phys.* **1972**, *5*, 1921-1929.
73. Siepmann, J. I.; Karaborni, S.; Smit, B. Simulating the critical behaviour of complex fluids. *Nature* **1993**, *365*, 330-332.
74. Tuckerman, M.; Berne, B. J.; Martyna, G. J. Reversible multiple time scale molecular dynamics. *J. Chem. Phys.* **1992**, *97*, 1990-2001.
75. Allinger, N. L.; Yuh, Y. H.; Lii, J. H. Molecular mechanics. The MM3 force field for hydrocarbons. *J. Am. Chem. Soc.* **1989**, *111*, 8551-8582.
76. Williams, G.; Watts, D. C. Non-symmetrical dielectric relaxation behaviour arising from a simple empirical decay function. *Trans. Faraday Soc.* **1970**, *66*, 80-85.
77. Williams, G.; Watts, D. C.; Dev, S. B.; North, A. M. Further considerations of non-symmetrical dielectric relaxation behaviour arising from a simple empirical decay function. *Trans. Faraday Soc.* **1971**, *67*, 1323-1335.
78. Tsolou, G.; Mavrantzas, V. G.; Theodorou, D. N. Detailed atomistic molecular dynamics simulation of cis-1,4-poly(butadiene). *Macromolecules* **2005**, *38*, 1478-1492.
79. Irving, J. H.; Kirkwood, J. G. The Statistical Mechanical Theory of Transport Processes. IV. The Equations of Hydrodynamics, *J. Chem. Phys.* **1950**, *18*, 817-829.
80. Cui, S. T., P. T. Cummings, and H. D. Cochran, "Molecular simulation of the transition from liquidlike to solidlike behavior in complex fluids confined to nanoscale gaps," *J. Chem. Phys.* **2001**, *114*, 7189-7195.

### III. Mechanical Properties of Polymer Nanocomposites

---

This chapter includes the materials from:

1. Lee, Y.<sup>†</sup>; Myoung, J.<sup>†</sup>; **Cho, S.<sup>†</sup>**; Park, J.; Kim, J.; Lee, H.; Lee, Y.; Lee, S.; Baig, C.\*; Ko, H.\* Bioinspired Gradient Conductivity and Stiffness for Ultrasensitive Electronic Skins. *ACS Nano* **2021**, *15*, 1795-1804.
  2. Park, J.<sup>†</sup>; Lee, Y.<sup>†</sup>; Barbee, M. H.<sup>†</sup>; **Cho, S.<sup>†</sup>**; Cho, S.; Shanker, R.; Kim, J.; Myoung, J.; Kim, M. P.; Baig, C.\*; Craig, S. L.\*; Ko, H.\* A Hierarchical Nanoparticle-in-Micropore Architecture for Enhanced Mechanosensitivity and Stretchability in Mechanochromic Electronic Skins. *Advanced Materials* **2019**, *31*, 1808148.
  3. Lee, Y.; Park, J.; **Cho, S.**; Shin, Y.-E.; Lee, H.; Kim, J.; Myoung, J.; Cho, S.; Kang, S.; Baig, C.; Ko, H.\* Flexible Ferroelectric Sensors with Ultrahigh Pressure Sensitivity and Linear Response over Exceptionally Broad Pressure Range. *ACS Nano* **2018**, *12*, 4045-4054.
  4. Ha, M.<sup>†</sup>; Lim, S.<sup>†</sup>; **Cho, S.<sup>†</sup>**; Lee, Y.; Na, S.; Baig, C.\*; Ko, H.\* Skin-Inspired Hierarchical Polymer Architectures with Gradient Stiffness for Spacer-Free, Ultrathin, and Highly Sensitive Triboelectric Sensors. *ACS Nano* **2018**, *12*, 3964-3974.
- 

#### 3.1 Introduction

Recently, significant interests in internet of things (IoT) boost the rapid development of flexible, wearable, and skin-attachable electronics, including artificial skins,<sup>1-3</sup> human-machine interface system,<sup>4,5</sup> sustainable power management,<sup>6-9</sup> and wireless signal transduction.<sup>10-12</sup> For the practical applications of wearable electronics in the fields of IoT, long-term sustainability as well as highly flexible, lightweight, and miniaturized designs are required to provide convenience and comfortable feelings for users as well as to achieve reliable and human-friendly electrical devices and sensors. Even though a great progress has been made in wearable platforms integrated with flexible, stretchable, and sustainable power systems,<sup>6,8,9</sup> energy storage systems still remain premature and insufficient for practical use because of the impermanent lifetime, limited capacity, and safety issue for the highly flexible and deformable designs of wearable devices.<sup>13</sup> On the other hand, self-powered wearable devices, which can generate power by harvesting ambient energy sources such as kinetic energy from human daily motion and thermal energy from body temperature, show great potential to address power issues in wearable electronics.<sup>7,14-18</sup>

To convert human bodily energy into available electricity, a variety of energy conversion systems have been developed based on piezoelectric,<sup>15-17</sup> thermoelectric,<sup>18</sup> electromagnetic,<sup>19</sup> and triboelectric effects.<sup>19,20</sup> Triboelectricity, a common phenomenon of charge generation occurring on the contact surface of two different materials, can be used to effectively convert frictional contact into

electricity.<sup>20</sup> The triboelectric devices can provide more diverse choices of flexible materials and higher power generation than other energy harvesting ones. In addition, triboelectric devices can be used as self-powered sensors as well to detect pressure and motion. Previously, Jiang et al. demonstrated a self-powered tactile sensor based on micro-textured poly(dimethylsiloxane) (PDMS), which showed the pressure sensitivity of 2.28 mV/kPa and the maximum power generation of ~130 nW.<sup>21</sup> Li et al. fabricated a dual-mode triboelectric sensor (TES) that perceived the tactile stimuli with the force sensitivity of 0.028 V/N and the generated output voltage of 10.6 V at 140 N.<sup>22</sup> To achieve both high sensitivity and output power, most of the previous TESs utilized bulk spacers,<sup>22</sup> arch shapes,<sup>23</sup> and 3D structures<sup>24</sup> to provide a large variation of gap distance between opposing surfaces, which is proportional to the triboelectric output voltage.<sup>14,25,26</sup> Although these designs based on high volumetric structures enhanced the performance of triboelectric devices and sensors, the bulky geometry impeded their applications in flexible and wearable devices.<sup>27</sup> Recently, ultra-thin and flexible TESs that were based on single-electrode device structures were also reported as motion tracking sensors.<sup>28,29</sup> Nevertheless, the single-electrode based TESs have limited applications in pressure sensors, because the generation of triboelectric charge is not uniform and can be randomly affected by the contact of different charged materials instead of the applied pressure. In addition, the single-electrode based TES is not a monolithic design which requires additional connections to induction and reference electrodes to provide the potential differences between them,<sup>30</sup> still causing the space constraints for use in wearable devices.

Moreover, the voluminous or non-monolithic designs of triboelectric devices also make the device packaging a challenge for applications in harsh environment. High air conductivity of humid atmosphere causes discharging of triboelectric charges and thus reduces the triboelectric output performances.<sup>31-34</sup> In these applications, fully packaged triboelectric devices are necessary for reliable and sustainable wearable devices. To achieve both fully packaged designs having large flexibility and maximal triboelectric charge generation, morphological and structural control of triboelectric materials and devices is highly required for the body-wearable and high performance self-powered TESs with ultrathin and flexible form factors.

The multi-functional mechanical sensitivity of biological tissues,<sup>35,36</sup> such as skin, is difficult to reproduce. In polymers that incorporate force-responsive molecules (i.e. mechanophores), mechanical force induces chemical transformations of mechanophores,<sup>37-39</sup> enabling controlled colour/luminescence changes,<sup>40,41</sup> mechanocatalysis,<sup>42,43</sup> isomerisation,<sup>44</sup> release of small molecules<sup>44,45</sup> and self-healing behaviours.<sup>46</sup> Mechanochromic polymers that undergo colour changes in response to mechanical stress can be used to directly visualise the stress distribution and mechanochemical activations within polymers, which is advantageous for application in stress/strain sensing<sup>47-49</sup> and damage monitoring in polymeric materials.<sup>50,51</sup> To induce stress-driven mechanochemical transformations, efficient transmission of mechanical stress through the polymer matrix and coupling

to the mechanophore is critical. Various factors affect the efficiency of mechanochemical activation, including the mechanophore position in the polymer chain,<sup>40</sup> polymer molecular weight,<sup>52</sup> polymer chain alignment<sup>53</sup> and temperature.<sup>54</sup> Mechanochemical activation can also be enhanced by controlling the hard and soft blocks within the polymer. In this approach, soft polymer chains can be aligned parallel to the tensile direction via localised stress at the hard polymer blocks<sup>55,56</sup> or soft mechanophores and hard ligands enable mechanochemistry even under isotropic compressive force.<sup>57</sup> However, most previously reported mechanochromic polymers exhibit mechanophore activation after irreversible plastic deformation<sup>51</sup> or provide reversible stretchability at the expense of mechanosensitivity.<sup>49,53,57,59</sup> For use in sensing applications, e.g. electronic skins, mechanochromic polymers with high stress sensitivity and reversible stretchability under large strain are needed. Furthermore, although several mechanophores based on fluorescent and phosphorescent properties have exhibited fast response/relaxation times to track force-induced luminescence changes in real-time,<sup>60,61</sup> mechanochromic polymers with sensing capability of high-frequency dynamic forces over a few hundreds of Hz are still required for multifunctional e-skins.<sup>62-64</sup> However, multifunctional mechanochromic materials with all these properties are yet to be demonstrated.

With human skin-like sensing capabilities, e-skin has emerged as one of the promising technologies of wearable devices,<sup>65,66</sup> soft robotics,<sup>67,68</sup> artificial prostheses,<sup>69,70</sup> and healthcare monitoring devices.<sup>71,72</sup> E-skins can perceive different external stimuli, including magnitude and distribution of mechanical stimuli, temperature, and subtle textural differences through electrical signals.<sup>73-75</sup> Among various e-skins with different sensing mechanisms (e.g., piezoresistivity, capacitance, piezoelectricity, and triboelectricity),<sup>76-80</sup> piezoresistive sensors have attracted considerable interest due to their simple fabrication process, low cost, and easy readout mechanism.<sup>81</sup> While conventional sensors relying on piezoresistance of bulk materials have shown rather low sensitivity,<sup>65</sup> recent approaches based on micro/nanostructures (e.g., micro-domes/pillars/pyramids,<sup>78,81,82</sup> micropores,<sup>83</sup> and sea-urchin nanoparticles<sup>84</sup>) have proven to improve the sensitivity because the piezoresistance is predominantly affected by the deformation of surface microstructures rather than the bulk material, resulting in a significant change in the contact resistance rather than bulk film resistance. Electrode design is another factor affecting the sensitivity. Instead of piezoresistive materials sandwiched between top and bottom electrodes,<sup>81-86</sup> coplanar electrode structures (two electrodes on the same side of the active layer) have shown enhanced pressure sensitivity<sup>87-90</sup> due to the dominant role of contact resistance of surface microstructures. In addition, employing slit<sup>91</sup> or interdigitated<sup>92,93</sup> patterns on the electrode induce high initial resistance, thus resulting in enhanced pressure sensitivity. However, existing sensors have shown non-linear or narrow-range sensing, because piezoresistance is mainly governed by the variation in contact resistance, showing rapid resistance saturation. In order to simultaneously obtain a linear response as well as high sensitivity over a large pressure range, hierarchical,<sup>94</sup> hollow,<sup>95</sup> and multi-layered microstructures<sup>96</sup>

have been suggested to further increase the contact area change and control the deformation patterns of active materials under pressure. However, most existing sensors still exhibit sensitivities less than  $50 \text{ kPa}^{-1}$ , which are insufficient to detect the subtle differences in bio-signals, such as pulse pressure variation and intracranial pressure. For practical applications of e-skin, the combined pressure sensing capabilities of linearity, high sensitivity, and wide detection range are critical. However, existing e-skins do not have the full extent of these properties.

### 3.2 Methods

The Finite Element Method (FEM) simulation is a numerical method of solving systems of partial differential equations (PDEs) in various fields of engineering and mathematical modeling. FEM is based on the concept of a continuum which can be continually sub-divided into infinitesimal elements with properties being those of the bulk material, as described in Figure 3.2.1. Therefore, many engineering problems (e.g., electrostatics, heat transfer, structural mechanics, fluid flow, acoustics, and so on) can be expressed by appropriate “Governing equations” and “Boundary conditions”. Based on these equations, we can obtain the algebraic equations for each element in complicated systems and solve PDEs for each element.

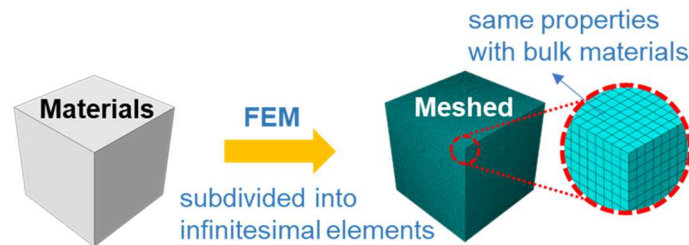


**Figure 3.2.1.** Schematic illustration of the Finite Element Method (FEM) simulation.

In this dissertation, through collaboration with experimental group, almost structural analysis to develop advanced polymer nanocomposite materials were performed by the FEM simulation (ABAQUS and COMSOL software), including stress propagation, gap distance and surface contact area between two polymeric layers under vertical pressure and bending strain. All simulated conditions of the sizes, compositions, surface morphology, and elastic modulus of polymer nanocomposites were consistent with the actual experimental conditions. To implement the mechanical contact interaction in response to the applied physical force between two polymeric layers for interlocked microdome sensors, we executed the general surface-to-surface contact interaction with linear elastic deformation of the interlocked and different surface-structured polymers.



### 3.3 Results and Discussion

**Triboelectric sensors:** The gradient stiffness between stiff epidermis and soft dermis with interlocked microdome structures in human skin induces effective stress transmission to underlying mechanoreceptors for enhanced tactile sensing. Inspired by skin structure and function, we fabricate hierarchical nanoporous and interlocked microdome-structured polymers with gradient stiffness for the spacer-free, ultrathin, and highly-sensitive triboelectric sensors (TESs), as shown in Figure 3.3.1. The skin-inspired hierarchical polymers with gradient elastic modulus enhance the compressibility and contact areal differences due to effective transmission of the external stress from stiff to soft layers, resulting in highly sensitive TESs capable of detecting human vital signs and voice. In addition, the microdomes in the interlocked polymers provide an effective variation of gap distance between interlocked layers without using the bulk spacer and thus facilitate the ultrathin and flexible design of TESs that could be worn on the body and detect a variety of pressing, bending, and twisting motions even in humid and underwater environments.

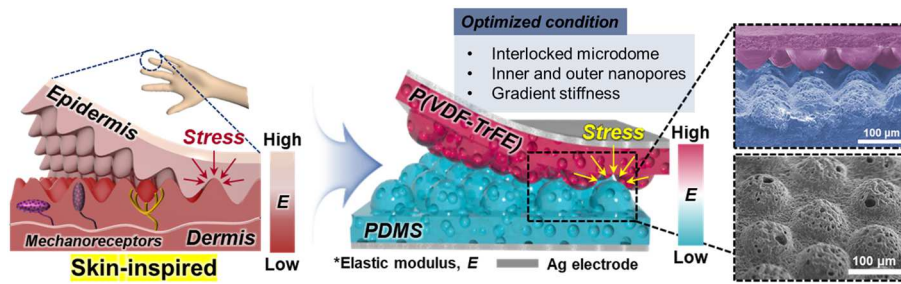


Figure 4.3.1. Structural characteristics of highly-sensitive triboelectric sensors.

Specifically, in this work, ultrathin, highly-sensitive, and wearable TESs were developed by the hierarchical polymeric architectures of nanoporous and interlocked microdome structures with gradient stiffness. The hierarchical geometry of nanoporous and interlocked microdome structured polymers could enhance the effective variations of gap distance between interlocked layers without bulk extra spacers and be an ultrathin and highly flexible design for wearable TESs as shown in Figure 3.3.2.

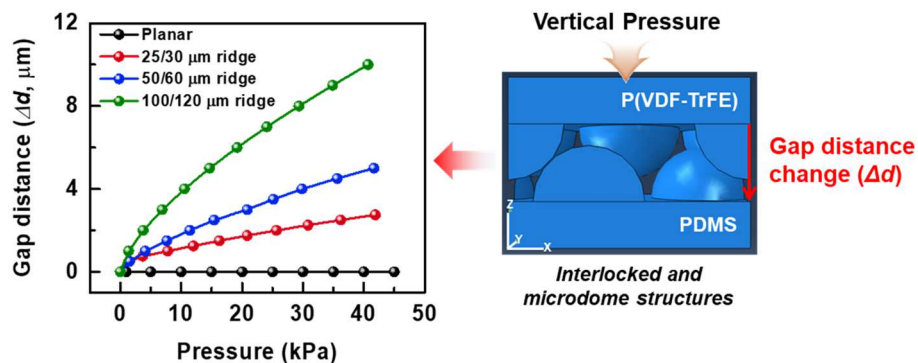
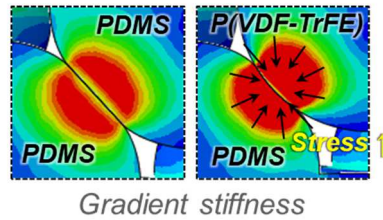


Figure 5.3.2. Theoretical analysis of the gap distance change in the interlocked films. The finite element

simulations by using ABAQUS software for the gap distance change ( $\Delta d$ ) from the initial gap in the interlocked microdome-structured and planar films with respect to the applied vertical pressure. Note that while the elastic modulus of P(VDF-TrFE) is constant as 1 GPa for all sizes of microdome arrays, that of PDMS decreases with the larger width/pitch size of microdome arrays due to the effect of nanoporous structure.

In addition, inspired by gradient stiffness of stiff epidermis and soft dermis layers, which can effectively transfer the external stress, the gradient elastic modulus of interlocked P(VDF-TrFE) and PDMS layers significantly enhanced the triboelectric output performances as well as pressure and bending sensitivity to perceive the minute pulse waves of radial artery and finger bending motion (see Figure 3.3.3).



**Figure 6.3.3.** Theoretical analysis of the stress distribution in the interlocked films under the vertical pressure. The finite element simulations of the stress distribution depending on the elastic modulus of interlocked and microdome-structured polymers by using ABAQUS software. The elastic modulus of P(VDF-TrFE) and PDMS is 1 GPa and 3 MPa, respectively. Left and right panels show the result for the contact interaction for the interlocked PDMS-PDMS and the P(VDF-TrFE)-PDMS layers, respectively.

To further understand the structural effect of hierarchical microdome arrays on the performance of TESSs, we analyzed the vertical stress propagation (Figure 3.3.4) and contact area (Figure 3.3.5) of TESSs having different width ( $w$ ) and pitch ( $p$ ) size of microdome arrays ( $w/p = 25/30$ ,  $50/60$ , and  $100/120 \mu\text{m}$ ) via theoretical and experimental methods. As shown in Figures 3.3.4 and 3.3.5, hierarchical PDMS microdome arrays with  $w/p$  of  $100/120 \mu\text{m}$  exhibit the largest deformation and increase of contact area between the interlocked P(VDF-TrFE) and PDMS microdome structures due to the lowest elastic modulus (which demonstrated with experimental results).

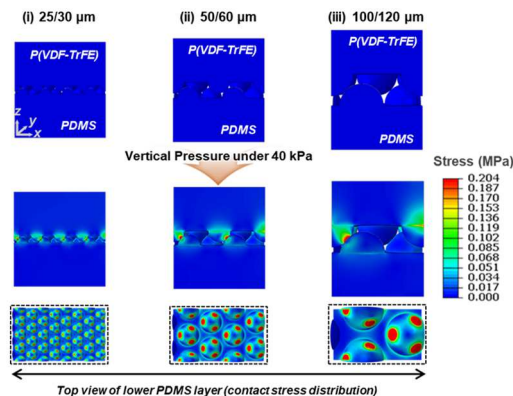


**Figure 7.3.4.** The finite element simulations for the comparison of vertical stress concentration with the different

width/pitch size of interlocked and microdome-structured polymers by using Abaqus software under the applied vertical pressure (40 kPa). The elastic modulus of P(VDF-TrFE) is 1 GPa, and that of PDMS is varied depending on the width/pitch size of microdome arrays.

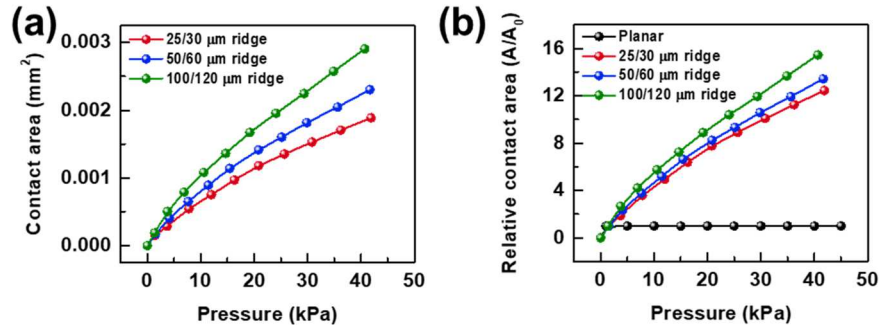


**Figure 8.3.5.** The finite element simulations for the comparison of the numerical calculation of (a) contact area and (b) relative contact areal change with the different width/pitch size of interlocked and microdome-structured polymers by using Abaqus software under the applied vertical pressure. The elastic modulus of P(VDF-TrFE) is 1 GPa, and that of PDMS is varied depending on the width/pitch size of microdome.

Figure 3.3.6a theoretically verifies that the potential difference from hierarchical microdome arrays increases by increasing width and pitch sizes, which can be attributed to the increase of gap distance (Figure 3.3.2) and large amount of triboelectric charge density, resulting from the increase of effective surface contact area (Figure 3.3.5) between triboelectric layers. The experimental results coincide with the theoretical estimation very well. While the resulting contact stress between the two layers shows an overall uniform (homogenous) distribution throughout the microdome arrays under the vertical pressure, a nonuniform (inhomogeneous) stress distribution appears in the case of bending process. This is because the microdome array of the top layer contracts inward and that of the bottom layer expands outward during bending process. Furthermore, given the same value of the radius of bending curvature, the degree of geometrical mismatch in contact between the two microdome arrays and thus the concomitant inhomogeneity for the contact stress distribution relatively increases with the larger width/pitch size of the arrays. As a result, the effective contact area becomes smaller for the larger size of interlocked microdome array. With these different aspects between the vertical pressing and bending process, as contrary to the response to vertical pressure, the theoretically calculated electric field of interlocked films from the bending strain exhibits that the electric field of hierarchical microdome arrays increases via decreasing width and pitch sizes (Figure 3.3.6b). Similarly, the triboelectric output voltage and current density increase by reducing the width and pitch sizes of microdome arrays.

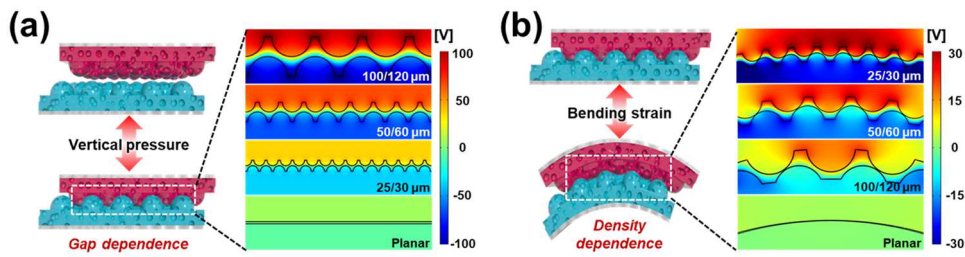


**Figure 9.3.6.** (a) Schematic illustration of gap distance change of TESs under vertical pressure and theoretically calculated electric field distribution and (b) density of point contact between interlocked micridges under bending strain and coincident theoretically calculated electric field distribution by COMSOL simulations depending on the width ( $w$ ) and pitch ( $p$ ) size of interlocked microdome arrays ( $w/p = 25/30, 50/60,$  and  $100/120 \mu\text{m}$ ) and planar structures.

Our TESs exhibited the highest power density ( $46.7 \mu\text{W}/\text{cm}^2$ ), and pressure ( $0.55 \text{ V}/\text{kPa}$ ) and bending ( $\sim 0.1 \text{ V}/^\circ$ ) sensitivities ever reported on the flexible TESs. Also, the fast responsive TESs could detect the dynamic stimuli from low frequency of contact vibrations to high frequency of acoustic wave for recognizing human voice. The spacer-free and monolithic design of ultra-flexible TESs could be not only worn on human hands but fully packaged for highly reliable and sustainable wearable devices as well. All of these outstanding functionalities of our skin-inspired and ultra-flexible TESs are available for both power generation and detection of human vital signs, voice recognition, and real-time monitoring of bodily motion even in a harsh environment, which facilitates the broaden applications for wearable health monitoring devices, self-diagnostic system, popular biometric security system, prosthetic limbs, rehabilitation devices, and humanoid robotics.

**Ferroelectric sensors:** Flexible pressure sensors with a high sensitivity over a broad linear range can simplify the wearable sensing systems without additional signal processing for the linear output, enabling device miniaturization and low power consumption. Here, we demonstrate a flexible ferroelectric sensor with ultrahigh pressure sensitivity and linear response over an exceptionally broad pressure range based on the material and structural design of ferroelectric composites with a multilayer interlocked microdome geometry, as shown in Figure 3.3.7.

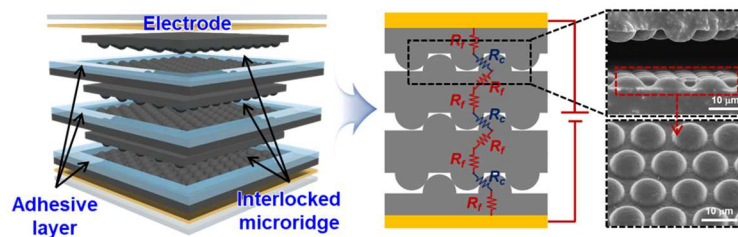


**Figure 3.3.7.** Structural characteristics of highly-sensitive ferroelectric sensors.

Specifically, in this work, we demonstrated a flexible ferroelectric sensor with high pressure sensitivity and linear response over an exceptionally broad pressure range. The suggested ferroelectric sensor is based on the rGO/PVDF ferroelectric composites with a multilayer interlocked microdome geometry. Figure 3.3.8a shows the calculated contact area change of three different multilayer e-skins as a function of applied pressure. The contact area of the interlocked microdome structures rapidly increases from almost zero in the initial unloading state to an extremely high value in the high-pressure loading state, which can be attributed to the concentrated and amplified stress at a small spot between interlocked microdomes that greatly deforms the interlocked microdomes, resulting in the significant increase of the contact area. With increasing number of stacked layers, the contact area dramatically increases due to the increased number of contacted microdomes. The contact area change in Figure 3.3.7a also indicates that the linearly increasing contact area starts to decrease at a pressure over  $\approx 244$  and 148 kPa for double- and single-interlocked layers, respectively, which is consistent with the experimental observations for the relative current ( $I/I_0$ ) of e-skins with multilayer geometry with different numbers of stacked layers and planar geometry in response to applied pressure. The multilayer geometry can enhance the linearity of pressure sensing because the multilayer interlocked microdomes can distribute the applied stress to each stacked layer (Figure 3.3.8b). As a result, pressure sensitivity and linearity increase with an increase in the number of layers in multilayer e-skins. We also investigated the effect of the rGO loading concentration on the pressure-sensing performances of multilayer e-skins.

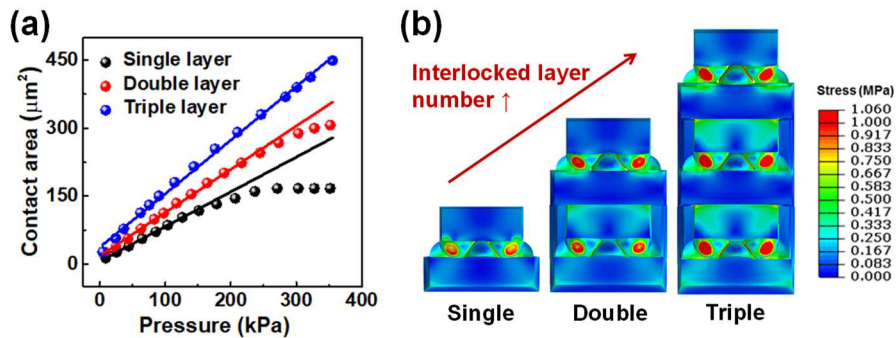


**Figure 3.3.8.** The finite element simulations of (a) the contact area change as a function of pressure for different numbers of stacked layers and (b) the local stress distribution for different numbers of interlocked layers showing the concentrated and amplified stress at the small spot between interlocked microdomes under a pressure of 100 kPa.

Our multilayer e-skins showed a simultaneous achievement of linear sensing capability with an ultrahigh sensitivity of  $47 \text{ kPa}^{-1}$  over an exceptionally large pressure-sensing range from 1.3 Pa to 353 kPa. The ultrahigh pressure sensitivity and linear response over an exceptionally broad pressure range can be achieved by the effective stress concentration, increased contact area, and stress

distribution between multilayer interlocked microdome arrays, which has been also verified by the theoretical calculations. These sensing capabilities enabled our e-skins to monitor diverse stimuli from low to high pressure range. For example, our e-skins can precisely monitor the weak gas flow and acoustic sound in a low pressure regime, respiration and pulse pressure in a medium pressure regime, and plantar pressure monitoring in a high pressure regime. The suggested e-skins may be useful for diverse sensor applications requiring precise detection of pressure from extremely low to high pressure range such as robotics, prostheses, and wearable healthcare devices.

**Mechanochromic sensors:** Biological tissues are multi-responsive and functional, and similar properties might be possible in synthetic systems by merging responsive polymers with hierarchical soft architectures. For example, mechanochromic polymers have applications in force-responsive colourimetric sensors and soft robotics, but their integration into sensitive, multi-functional devices remains challenging. Herein, we report a hierarchical nanoparticle-in-micropore (NP-MP) architecture in porous mechanochromic polymers to enhance the mechanosensitivity and stretchability of mechanochromic electronic skins (e-skins), as shown in Figure 3.3.9.

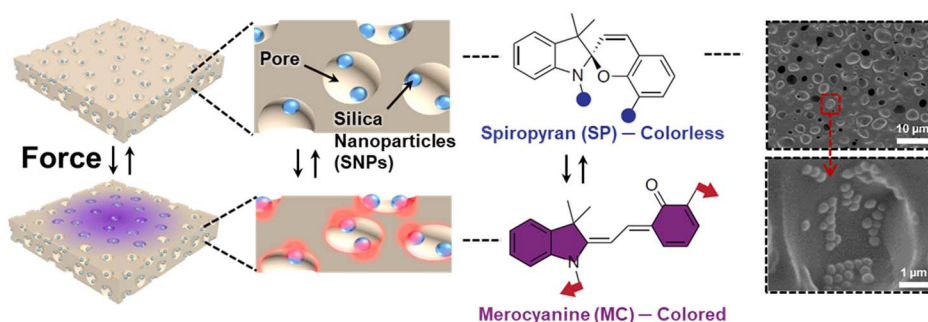


**Figure 3.3.9.** Structural characteristics of highly-sensitive mechanochromic sensors.

Specifically, in this work, this study demonstrates that a hierarchical NP-MP architecture in porous mechanochromic composites can enhance both mechanochromic strain/stress sensitivity and stretchability. The experimentally determined structure–activity relationships and computational modelling results suggest the following general design principle: reducing pore size while increasing SNP size should enhance the mechanochromic sensitivity. To demonstrate this design principle, we analyzed the simulated localized stress numerically calculated by finite-element analysis (FEA). From the stress–strain curves of the porous PDMS/SP composites, the required critical stress for their initial color transition is 0.17–0.2 MPa, whereas the planar composites exhibit a critical stress of 0.67 MPa. The decreased critical stress (3.4–3.9 times) for the porous structures can be attributed to the highly localized stress concentration that originates from the large difference in mechanical modulus between the polymer matrix and air. As summarized in Figure 3.3.10, the higher stress localization can be

observed following great circle of pore than planar structure, which induces to be higher than critical stress for mechanochromic activation of SP near the pore. All of the porous structures exhibit 1.6 times higher maximum localized stress, than that exhibited by the planar structure under a strain of 100% (Figure 3.3.10b), which result matches with the experimental result that depicts a decrease in the critical strain (55%) for the porous structures as compared with the planar one (150%). Furthermore, the porous structure with the smaller pore size possesses a higher PDMS/air interface surface area, which can increase the mechanochromic activation sites of concentrated stress near the interface, resulting in a considerable increase in color contrast, strain sensitivity, and strain sensing range. Based on these results, it is worth noting that the number of activation sites for localized stress around the pore would be crucial for dependence of pore size on mechanochromic sensitivity, rather than maximum localized stress. For the porous mechanochromic composites having SNPs, the greatly reduced critical stress at strain values of 35%, 45%, and 45% corresponds to 0.08–0.14 MPa, which can be attributed to significant enhancement in maximum localized stress by up to 5.7 times near the SNPs (Figure 3.3.10c). Further, the maximum localized stress near SNPs gradually increases with the size of SNPs (Figure 3.3.10c), leading to significant reduction of critical stress (35%) for mechanochromic activation and thereby enhancing mechanochromic sensitivity under the same strain.

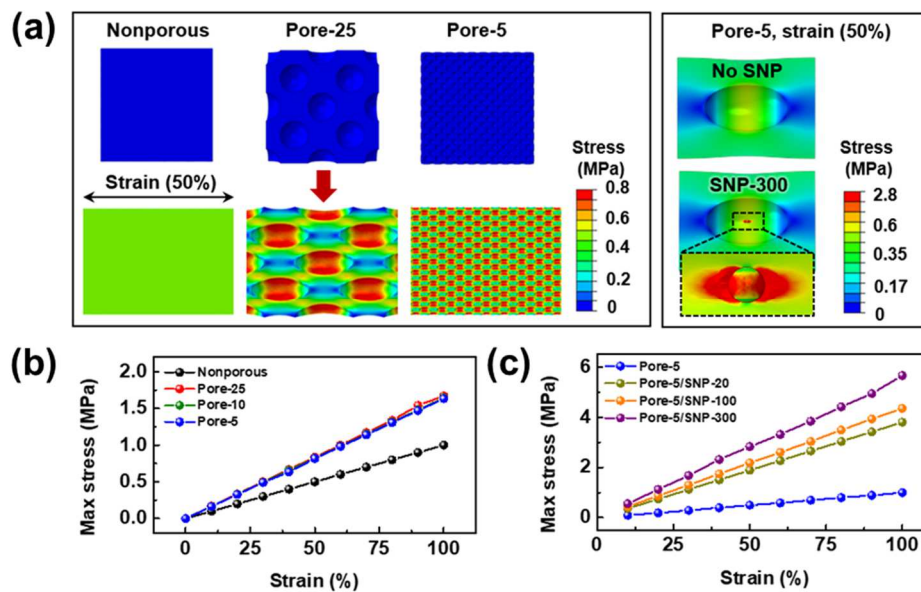


**Figure 3.3.10.** The finite element simulations of (a) stress distributions of mechano-chromic polymers with different pore sizes (left) and with 300-nm SNPs and a 5- $\mu\text{m}$  pore size (right) under a tensile strain of 50% and maximum localized stress near the pore surface in porous mechano-chromic polymers with (b) different pore sizes and (c) different SNP sizes and a pore size of 5  $\mu\text{m}$  as a function of strain (see Figure 3.3.11 for the initial system configuration).

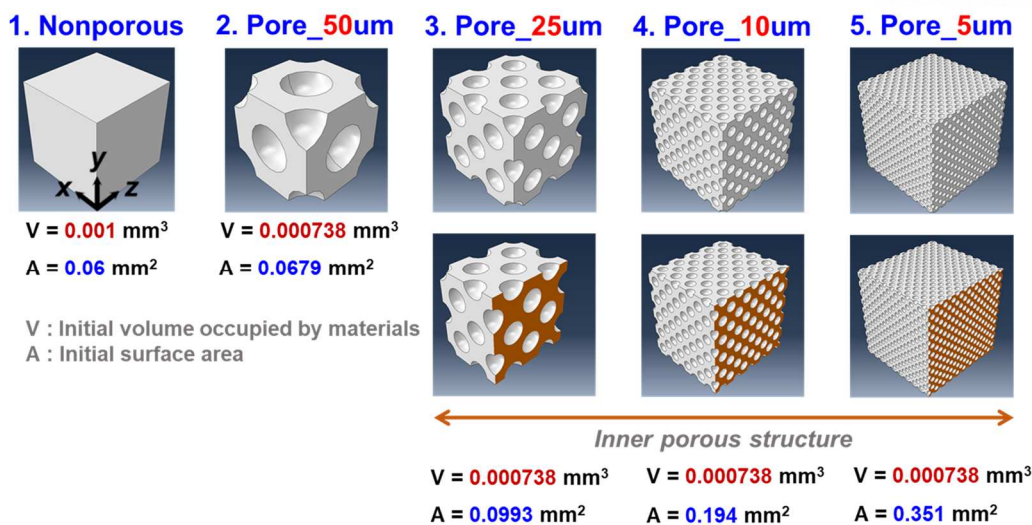


**Figure 3.3.11.** Simulated surface areas of porous mechanochromic composites with different pore sizes based on face-centered cubic (FCC) unit cell arrays. The porous structures are modelled according to average pore sizes of 50, 25, 10 and 5  $\mu\text{m}$  with the same porosity (26%) based on FCC unit cell arrays. Volume is determined as the total material volume, excluding the pore volume. Area is the total surface area of the porous structure.

Likewise, the porous structure with the smallest pore size amongst the samples possesses the highest PDMS/air surface area, resulting in a greater number of mechanochromic activation sites of concentrated stress near the interface (Figure 3.3.12). This produced a considerable enhancement in colour change and strain sensitivity. For the porous composites decorated with SNPs, additional stress concentration occurs in the pore region near the SNPs because of the load-bearing support provided by the hard SNPs at the inner surfaces of the soft pores. Furthermore, the maximum localised stress near the SNPs gradually increases with SNP size (Figure 3.3.13), thereby enhancing mechanochromic sensitivity. Based on the FEM results, we can conclude that both the amount of activation sites and the maximum stress localized around the pores and SNPs determine the overall mechanochromic sensing properties (relative colour intensity and strain sensitivity). Most material modifications that enhance the onset of mechanochromism also reduce extensibility, because mechanochromism is triggered by polymer chains approaching their maximum extension. In contrast, the hierarchical NP-MP architecture of the porous composite structure in this study simultaneously reduces the onset of mechanochromism and enhances the extensibility. This advance will allow us to introduce mechanochromism to devices which operate under a range of strain conditions, from very small to large amounts of deformation. As a proof of concept, we fabricated an e-skin based on the composite material and used it as a wearable motion sensor and dual-mode touch audio sensor. The e-skin enabled the detection of static/dynamic force without any external power source.



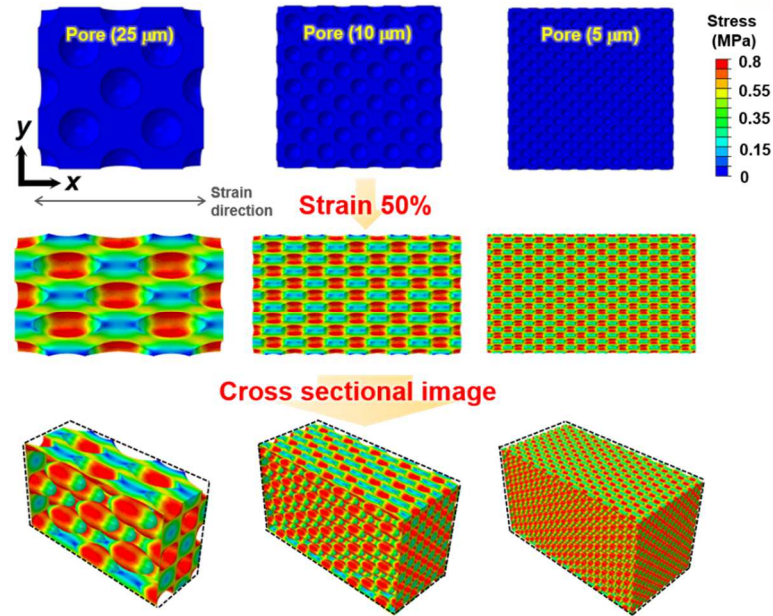


**Figure 3.3.12.** The finite element simulations of stress distributions of porous PDMS/SP composites with different pore sizes (25, 10 and 5  $\mu\text{m}$ ) placed under 50% tensile strain calculated numerically using Abaqus software. For simplicity, the elastic modulus is set to 1 MPa with the same porosity (26%) for all porous composites (see Figure 3.3.11 for the initial system configuration).

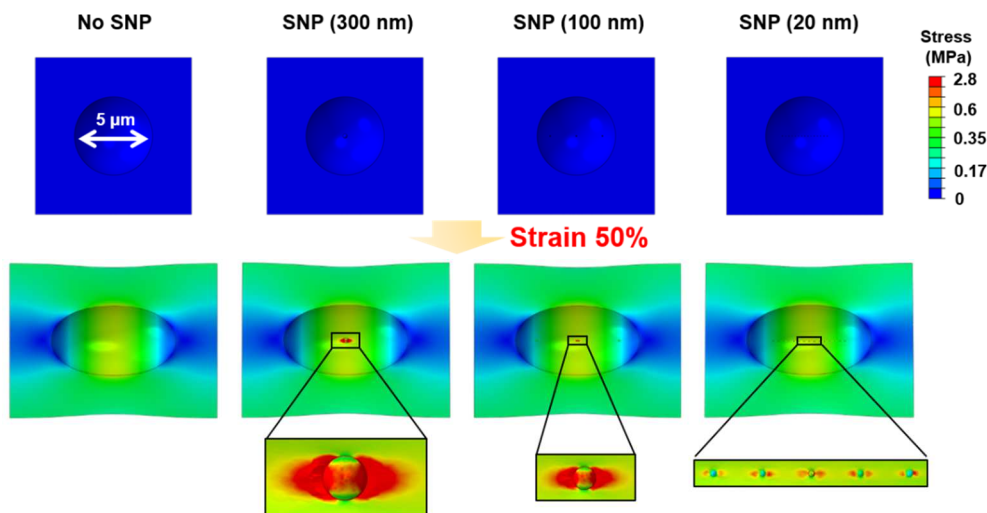


**Figure 3.3.13.** The finite element simulations of stress distribution of porous PDMS/SP composites (pore size = 5  $\mu\text{m}$ ) decorated with SNPs with different sizes (300, 100 and 20 nm) placed under 50% tensile strain calculated numerically using Abaqus software. For simplicity, to understand the role of the SNPs at the pore walls, the elastic modulus of the porous matrix is set to 0.24 MPa (consistent with the experimental data). The elastic modulus of the SNPs is set to a general value of 180 GPa for all sizes.

The hierarchical NP-MP architecture of the mechanochromic composites also enhances the mechanochromic sensitivity in response to normal force in addition to tensile strain. This property allows the composites to be applied in touch-sensitive mechanochromic e-skins. We evaluated the changes in the RGB color parameters of the composites in response to normal forces applied using a force gauge. Under a normal force of 6 N, the porous PDMS/SP/SNP composites exhibit more vivid mechanochromic color than the nonporous and porous structures. Compared to the nonporous and porous structures, the changes in the relative red intensities were larger for the hierarchical NP-MP structures, indicating a more vivid color change. The relative red intensity decreased from 0.42 to 0.24 in conjunction with decreasing pore size (Figure 3.3.14a). This phenomenon is attributed to the increase in the area of stress concentration with decreasing pore size (Figure 3.3.14b). Meanwhile, decorating the porous structures with SNPs further increases the dynamic color transition range to 85% over a wide range of force (1–12 N). Amongst the composites with different SNP sizes, the composite with the largest SNPs (300 nm) exhibits the largest color variation (85%) without saturation (Figure 3.3.15a). Decorating the pores with 300-nm SNPs further improves the pressure sensitivity, thus enabling detection at a minimum force of 1 N, six times lower than the minimum detection force of nonporous polymers (6 N). The improvement in mechanochromic sensitivity achieved by the addition of SNPs is attributed to the drastic increase in localized stress near the hard SNPs. The FEM calculations indicate that amongst the tested SNPs, the 300-nm SNPs exhibit the strongest localized stress in response to normal force (Figure 3.3.15b). The low detection limit (1 N or 1 MPa) represents a significant enhancement (~50 times increase) over previously reported mechanochromic polymers (50 and 375 MPa). The porous mechanochromic composites reported herein also provide a high lateral resolution for force sensing, enabling the mapping of local pressure distribution without the need for complex sensor array patterns.

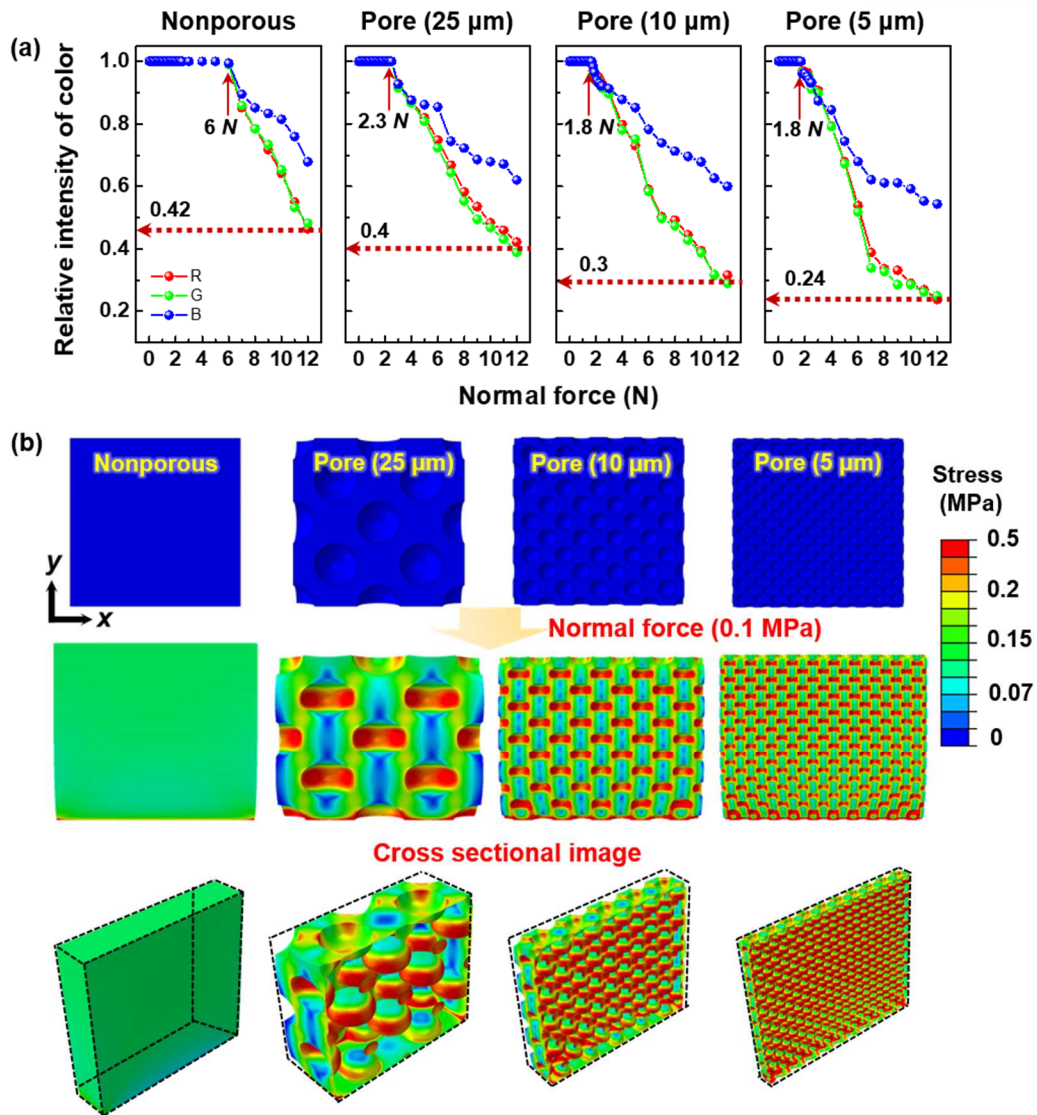


**Figure 3.3.14.** (a) Relative color changes of porous PDMS/SP composites with different pore sizes in response to applied normal pressure. (b) The finite element simulations of stress distributions in porous PDMS/SP composites with different pore sizes under applied normal pressure. The simulation conditions are identical to those in Figure 3.3.12.

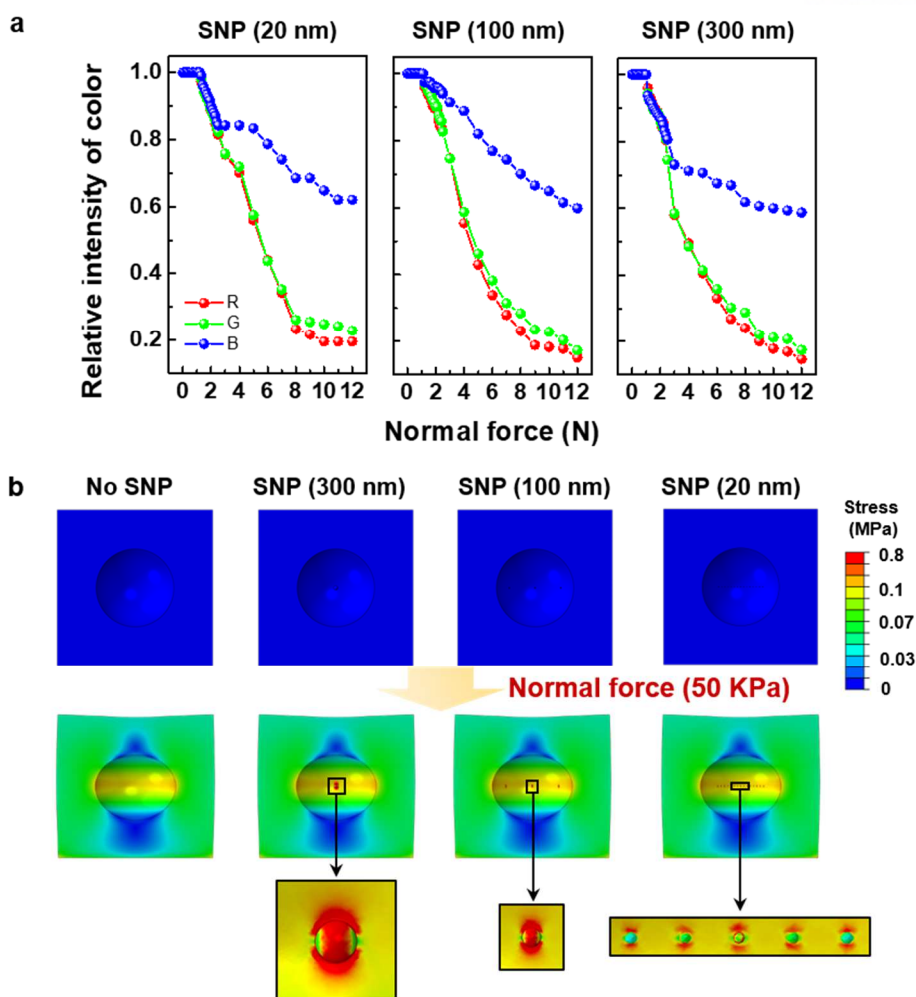


**Figure 3.3.15.** (a) Relative color intensities of porous PDMS/SP composites (pore size = 5  $\mu\text{m}$ ) decorated with SNPs of different sizes (20, 100, and 300 nm) as functions of vertical pressure. (b) The finite element simulations of stress distributions at the surfaces of pores in porous PDMS/SP composites with SNPs under applied pressure. The simulation conditions are identical to those in Figure 3.3.13.

In the future, this strategy could be extended to improve the stress-reporting capabilities of other mechanophores. Previous work has indicated that (i) the extent of mechanophore activation can be directly related to the first invariant of the local strain, independently of whether the strain is applied in a uniaxial or biaxial manner, and (ii) while the absolute magnitude of mechanophore activation depends on the mechanophore, the relative amount of mechanophore activation as a function of strain is constant across a range of strains in filled PDMS elastomers. The strain-focusing approach described here should therefore carry over to other mechanophores, and we anticipate that further work in this and similar composite materials will provide additional insight into the design of more active mechanochromic materials. Our hierarchical NP-MP framework is expected to allow the development of multifunctional and multiresponsive mechanochemical materials for user-interactive devices, smart robotics and wearable healthcare/diagnosis applications in future.

**Piezoresistive sensors:** Hierarchical and gradient structures in biological systems with unique mechanical properties have inspired innovations in materials design for construction and mechanical applications. Analogous to the control of stress transfer in gradient mechanical structures, the control of electron transfer in gradient electrical structures should enable the development of high-performance electronics. This paper demonstrates a high performance electronic skin (e-skin) via the simultaneous control of tactile stress transfer to an active sensing area, and the corresponding electrical current through the gradient structures, as shown in Figure 3.3.16. The flexible e-skin sensor has extraordinarily high piezoresistive sensitivity at low power and linearity over a broad pressure range, based on the conductivity-gradient multilayer on the stiffness-gradient interlocked microdome geometry.

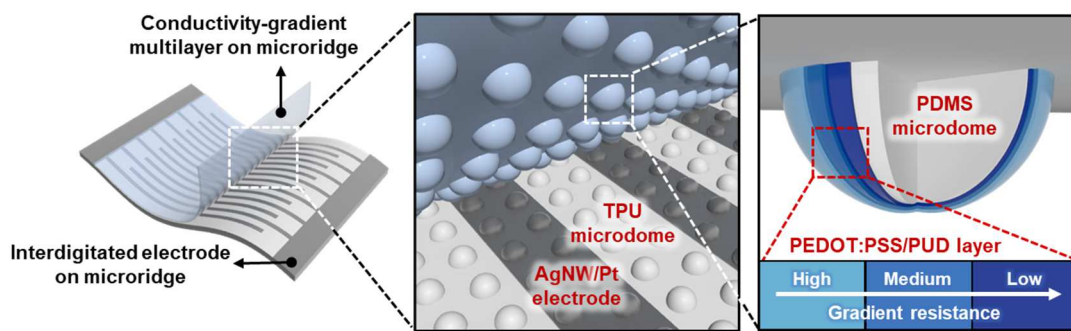


**Figure 3.3.16.** Structural characteristics of highly-sensitive piezoresistive sensors.

Specifically, in this work, we introduced the coplanar electrode design, because its piezoresistance variation highly depends on the change in contact resistance of surface microstructures compared with the sandwiched top and bottom electrodes design, thereby enabling giant piezoresistance variations from the insulator ( $\sim 10^9 \Omega$ ) to the conductor ( $\sim 10^2 \Omega$ ), according to the contact area and conductivity of the active material (see Figure 3.3.17). In addition, the conductivity of each layer in the PEDOT:PSS/PUD multi-layers on the PDMS microdomes is designed to gradually increase from the outer layers to the inner layers for the cascade activation of piezoresistive current pathways. Furthermore, the interlocked microdome structure enables effective stress concentrations at small contact spots between the microdomes, leading to the instantaneous and drastic increase in the pressure-induced contact area and the resulting decrease of piezoresistance. As one of the most important features on this work, the interlocked structures with stiffness-gradient can also be observed in the interlocked micro-ridge structures on the human skin. In the human skin, owing to the modulus difference between the interlocked epidermal and dermal layers, applied tactile stimuli are highly concentrated at the interface of the stiffness-gradient interlocked ridge structure and efficiently transferred to the underlying mechano-receptors, allowing highly sensitive tactile sensing functions. The design of the stiffness-gradient interlocked structure is important in enhancing the pressure-sensing performances by the

effective stress concentration effect, as shown in Figure 3.3.18. In addition, the use of TPU with a high Young's modulus enables stable working of the bottom interdigitated electrode.

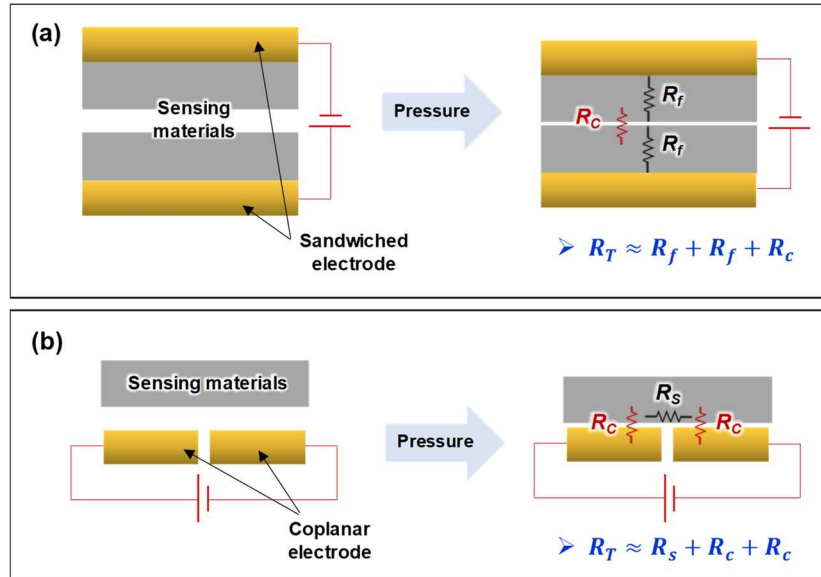


**Figure 3.3.17.** Comparison of pressure sensors with sandwiched electrode and coplanar electrode. (a) Working mechanism of the pressure sensor with sandwiched electrode. The total resistance ( $R_T$ ) depends on both contact resistance ( $R_c$ ) and bulk resistance ( $R_f$ ). (b) Pressure-sensing mechanism of the pressure sensor with coplanar electrode. The total resistance depends on sheet resistance ( $R_s$ ) and contact resistance, but mainly on contact resistance.

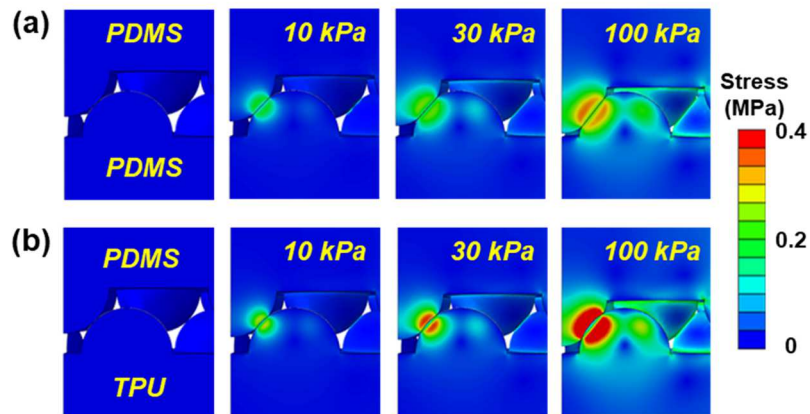


**Figure 3.3.18.** The finite element simulations of the local stress distribution for piezoelectric sensors with (a) top and bottom PDMS layers and (b) the stiffness-gradient interlocked structure with top PDMS layer and bottom TPU layer using Abaqus software. The simulated top and bottom layers were composed of PDMS or TPU materials corresponding to each condition, with interlocked microdome structures with a diameter of  $10 \mu\text{m}$  and a pitch of  $12 \mu\text{m}$  (i.e., unit cell of hexagonal arrays). The elastic modulus of PDMS and TPU materials were 1.98 MPa and 65 MPa, respectively, which were consistent with the experimental values.

Typically, multi-level mechanical structures are introduced in piezoresistive e-skins to enhance sensing performances over those based on planar bulk materials. However, improving sensing performances by engineering of multi-level mechanical structures still has severe limitations in enhancing the linear sensing capability and sensitivity. In contrast, engineering of gradient electrical structures in combination with gradient mechanical structures can significantly enhance the sensitivity and linearity of piezoresistive e-skins. Figure 3.3.19 schematically illustrates the piezoresistive sensing mechanism of the multi-layered sensor with gradient conductivity. In the conductivity-gradient multi-layers, the outermost PEDOT:PSS/PUD composite layer (third layer) with highest resistance is firstly activated under low initial pressure, inducing low current flows through the highly resistive layer (Figure 3.3.19a,  $I_3$ ). As the pressure is gradually increased, the electrical current pathway is steadily expanded into the inner second ( $I_2$ ) and first ( $I_1$ ) layers with lower resistances, owing to the pressure-induced increase in the contact area and decrease in the thickness of the elastic multi-layers (Figures 3.3.19b and 3.3.19c), leading to the gradual increase of current flows through the multi-layers. Therefore, ripples of cascading electrical activations are generated from outer to inner layers until reaching the saturation current by the innermost layer. Therefore, through the superposition of pressure-dependent electrical current ( $I_1$ ,  $I_2$ ,  $I_3$ ) of each layer in the multi-layers, the conductivity-gradient structure enables ultra-high pressure sensitivity by the large current differences between the initial and saturation currents, and linear pressure detection over a large pressure range by the gradual activation of current pathways from outer to inner layers with higher to lower resistances, respectively (Figure 3.3.19c).

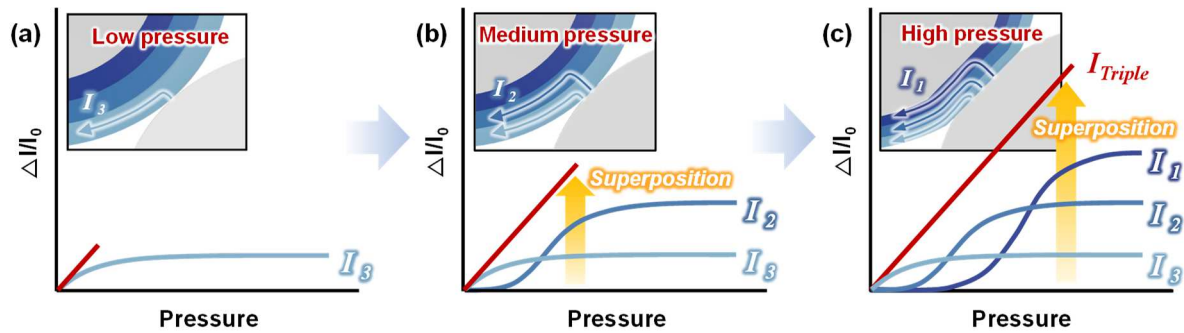


**Figure 3.3.19.** Schematic illustration and pressure-sensing trends of multi-layered e-skin under (a) low pressure range, (b) medium pressure range, and (c) high pressure range. The red line represents the relative current change of the triple-layered pressure sensor based on the superposition of pressure-dependent electrical current of each layer in multi-layers.

To demonstrate this sensing mechanism, we put forward theoretical and numerical analyses of the physical basis of the remarkably enhanced sensitivity and linearity over a broad range of pressure for the conductivity-gradient multi-layered sensors. To achieve a systematic numerical analysis for the

multi-layered sensors, we first describe the electrical behavior for each single layer in response to the applied pressure by introducing a simple, modified Boltzmann-type exponential function:

$$I = I_{\infty} + (I_0 - I_{\infty})e^{-(\beta\Delta P)^{\gamma}}. \quad (3.1.1)$$

Here,  $I_0$  denotes an initial electric current at very small applied pressure ( $\Delta P \approx 0$ ) and  $I_{\infty}$  is an asymptotical current in the limit of high pressure.  $\beta$  and  $\gamma$  represent the effective pressure sensitivity, especially in the low-to-intermediate pressure regime, and stretched exponential behavior in the intermediate-to-high pressure regime, respectively. Thus, both  $\beta$  and  $\gamma$  generally depend on the mechanical modulus and electrical conductivity of the layer, the layer geometry, the applied pressure type, and so on. This simple expression is found to be a reasonable description of the overall behavior of electric current in each single-layered sensor (300 k $\Omega$ /sq, 60 k $\Omega$ /sq, and 226  $\Omega$ /sq) when compared with the experimental results across the entire pressure range (Figure 3.3.20).

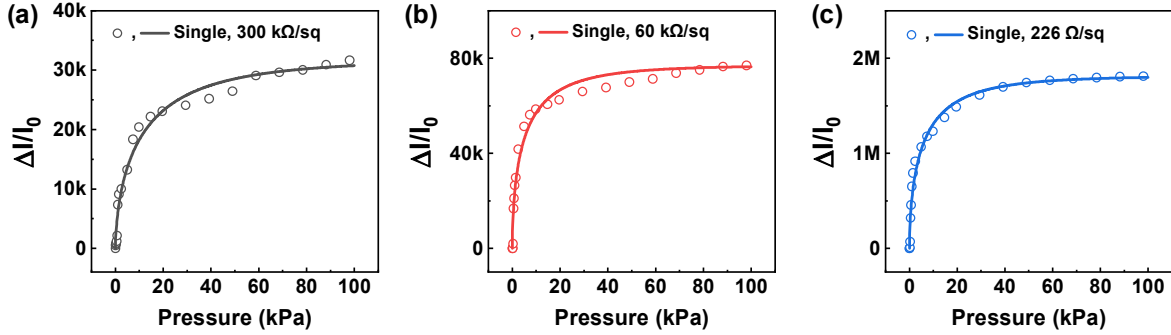


**Figure 3.3.20.** Experimental results (symbol) and numerical results (solid line) of the electric current for single-layered pressure sensors with different sheet resistance; (a) 300 k $\Omega$ /sq, (b) 60 k $\Omega$ /sq, and (c) 226  $\Omega$ /sq.

We now extend our analysis to multi-layered sensors. To simplify the numerical analysis while still capturing the essential physical features, we assume that each layer in the multi-layered sensors makes an individual contribution to the total current,  $I$ , in parallel; *e.g.*,  $I = I_1 + I_2 + I_3$  for a triple-layered sensor with  $I_1$ ,  $I_2$ , and  $I_3$  representing the electric current passing through the first (inner), second (middle), and third (outer) layer, respectively. Here, we supposed that the variations in  $I_1$ ,  $I_2$ , and  $I_3$  with the applied pressure effectively accommodate all the complex physical influences in association with the mechanical deformation of each layer, variable interfacial electrical resistance between adjacent layers, and so on. By considering that the surrounding outer layers offer additional electrical resistance by geometrically blocking the current flow to the inner layers, we propose the following expression for double-layered sensors:

$$I_{\text{double}} = I_{2,\text{single}} + f_2(\Delta P)I_{1,\text{single}} \quad \text{with} \quad 0 \leq f_2(\Delta P) < 1. \quad (3.1.2)$$



Here, the lower index represents the inner layer. Notice that we retain the original electrical behavior of each single layer in describing the overall electrical behavior of multi-layered sensors. Due to the various complex physical phenomena occurring in the multi-layered sensors in response to external pressure, the detailed functional form of  $f_2(\Delta P)$  is generally unknown. However, to understand the intrinsic features of multi-layered sensors, we consider a simpler situation. For instance, we suppose  $f_2(\Delta P) = H(\Delta P - \Delta P_0)$ , with the Heaviside step function,  $H$ , and the associated threshold pressure value,  $\Delta P_0$ . This form of  $f_2(\Delta P)$  physically represents a delayed conductive behavior of the inner first layer due to the outer second layer. A simple numerical result for the double-layered sensor based on equation 3.1.2 incorporating a single layer information is shown in Figure 3.3.21.

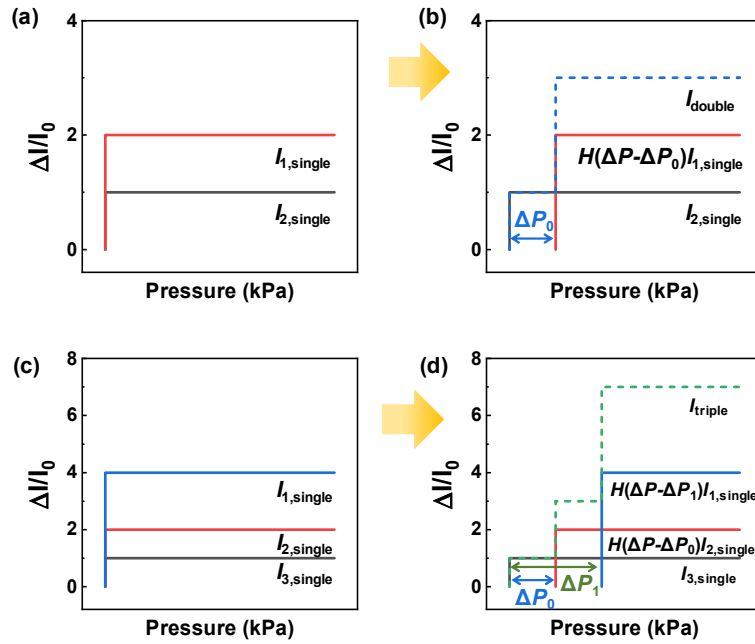


**Figure 3.3.21.** Simple numerical analysis of ideal electrical behaviors on (a,b) double-layered and (c,d) triple-layered sensors. The lower index ( $I_{1,\text{single}}$ ,  $I_{2,\text{single}}$ , and  $I_{3,\text{single}}$ ) represents the inner layer for both double- and triple-layered sensors. We adopt a form of the Heaviside step function,  $H(\Delta P - \Delta P_0)$ , with the associated threshold pressure,  $\Delta P_0$ , which is an ideal way to describe the delayed conductive behavior of the inner layer for multi-layered sensors. Note that the overall electrical behavior of the double ( $I_{\text{double}}$ ) and triple ( $I_{\text{triple}}$ ) layers are obtained *via* the linear superposition of each single layer as  $I_{\text{double}} = I_{2,\text{single}} + H(\Delta P - \Delta P_0)I_{1,\text{single}}$  and  $I_{\text{triple}} = I_{3,\text{single}} + H(\Delta P - \Delta P_0)I_{2,\text{single}} + H(\Delta P - \Delta P_1)I_{1,\text{single}}$ .

The adoption of the Heaviside step function  $H$  for  $f_2(\Delta P)$  is an ideal way to describe the delayed conductive behavior of inner layer for multi-layered sensors only for increasing the pressure

sensing range. Therefore, to realistically describe the high sensitivity and linearity over broad pressure ranges and account for complex physical phenomena involved in multi-layered sensors, a simple Heaviside step function is insufficient. If a more physical form of  $f_2(\Delta P) = [1 - e^{-(\beta_2 \Delta P)^{\gamma_2}}]$  that is consistent with the Boltzmann-type expression of equation 3.1.1 is adopted, the overall electrical behavior of the double-layered sensors can be described as:

$$I_{\text{double}} = I_{2,\text{single}} + [1 - e^{-(\beta_2 \Delta P)^{\gamma_2}}] I_{1,\text{single}} \quad (3.1.3)$$

The factor of  $f_2(\Delta P) = [1 - e^{-(\beta_2 \Delta P)^{\gamma_2}}]$  to impose single layer ( $I_{1,\text{single}}$ ) itself has the crucial role of increasing the linear sensing range over a large pressure range, even for single-layered sensors (Figure 3.3.22a). For double-layered sensors, through linear superposition from equation 3.1.3, pressure sensitivity and linearity additionally increase over an extended pressure range with the incorporation of each single-layer information (layers 1 and 2) (Figure 3.3.22b). Thus, the Boltzmann-type expression for  $f_2(\Delta P)$  provides a reasonable description of the overall electrical behavior in conjunction with the delayed conductive behavior of the inner layer for double-layered sensors.

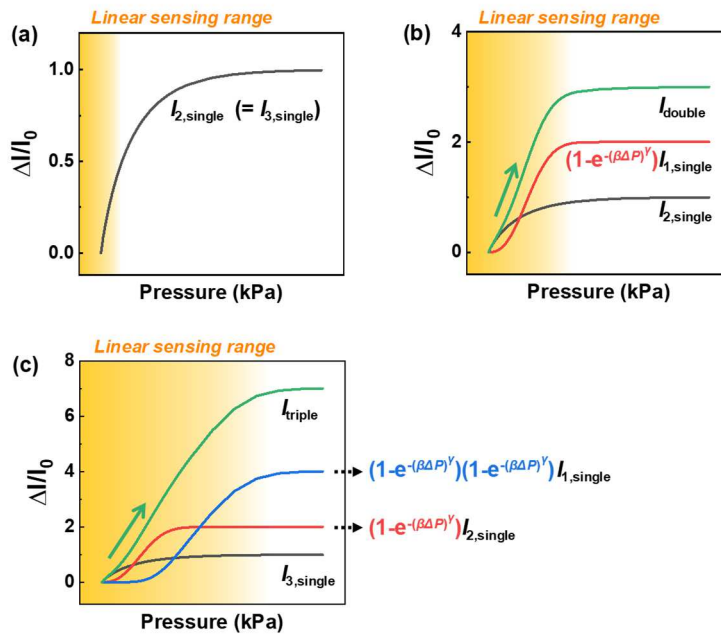


**Figure 3.3.22.** Numerical analysis of realistic electrical behaviors in (a) single-layered, (b) double-layered, and (c) triple-layered sensors. The lower index ( $I_{1,\text{single}}$ ,  $I_{2,\text{single}}$ , and  $I_{3,\text{single}}$ ) represents the inner layer for both double- and triple-layered sensors. We adopt a more physical form of the Boltzmann-type exponential function

$(1 - e^{-(\beta \Delta P)^\gamma})$  to describe the delayed conductive behavior of inner layer for multi-layered sensors. Note that the overall electrical behavior of double ( $I_{\text{double}}$ ) and triple ( $I_{\text{triple}}$ ) layers are obtained *via* the linear superposition of

each single layer as  $I_{\text{double}} = I_{2,\text{single}} + [1 - e^{-(\beta_2 \Delta P)^{\gamma_2}}] I_{1,\text{single}}$  and

$$I_{\text{triple}} = I_{3,\text{single}} + [1 - e^{-(\beta_3 \Delta P)^{\gamma_3}}] I_{2,\text{single}} + [1 - e^{-(\beta_3 \Delta P)^{\gamma_3}}] [1 - e^{-(\beta_2 \Delta P)^{\gamma_2}}] I_{1,\text{single}} \cdot$$

Based on the numerical analysis of a double layer, we further extend equation 3.1.2 to a triple-layered sensor:

$$I_{\text{triple}} = I_{3,\text{single}} + f_3(\Delta P)I_{2,\text{single}} + f_2(\Delta P)f_3(\Delta P)I_{1,\text{single}} \quad \text{with } 0 \leq f_2(\Delta P), f_3(\Delta P) < 1. \quad (3.1.4)$$

Note that we applied not only  $f_2(\Delta P)$  but also  $f_3(\Delta P)$  consistently to the innermost layer, considering the same effect [ $f_3(\Delta P)$ ] of the outermost layer on the first and second layers. Furthermore, as consistent with the Boltzmann-type expression of equation 3.1.1, adopting the forms of  $f_2(\Delta P) = [1 - e^{-(\beta_2 \Delta P)^2}]$  and  $f_3(\Delta P) = [1 - e^{-(\beta_3 \Delta P)^3}]$ , we have the following form of overall electrical behavior of the triple-layered sensors:

$$I_{\text{triple}} = I_{3,\text{single}} + [1 - e^{-(\beta_3 \Delta P)^3}]I_{2,\text{single}} + [1 - e^{-(\beta_2 \Delta P)^2}][1 - e^{-(\beta_3 \Delta P)^3}]I_{1,\text{single}}. \quad (3.1.5)$$

The numerical result for triple-layered sensors based on equation 3.1.5 is shown in Figure 3.3.22c, which is consistent with the physical aspects of the numerical analysis for the double layer that describes the delayed conductive behavior of the inner layer for multi-layered sensors. As a result, pressure sensitivity and linearity increase from single to triple layers over broad pressure ranges (Figure 3.3.22). We further note that all the numerical results based on equations 3.1.3 and 3.1.5 properly describe the general behavior of the electric current and agree well with the experimental results of double- and triple-layered sensors across the entire pressure range (Figure 3.3.23).

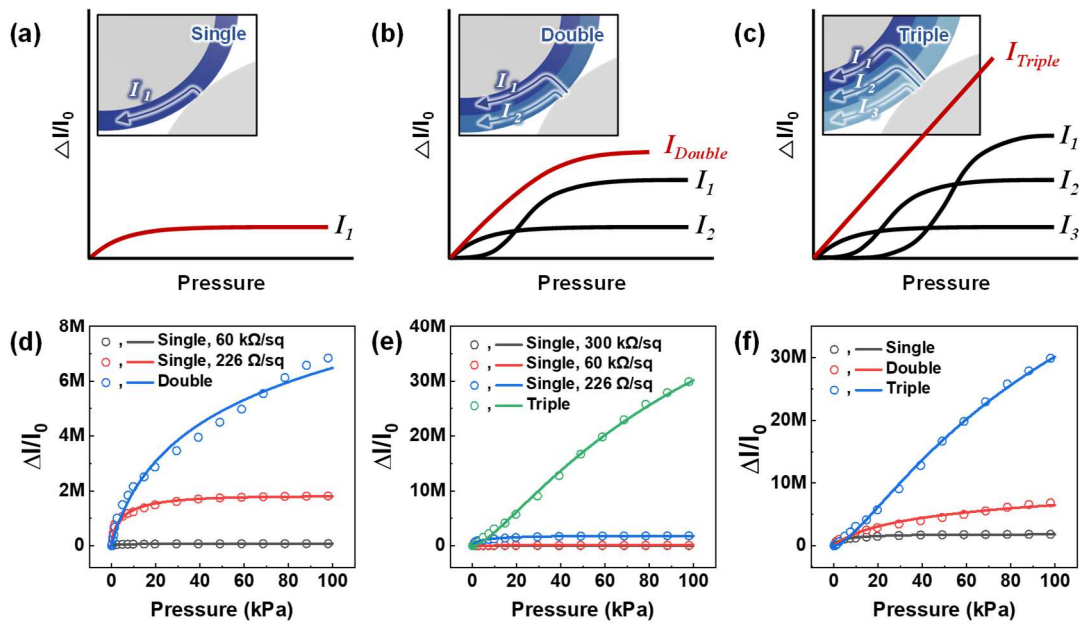


**Figure 3.3.23.** Schematic illustration and pressure-sensing trends of (a) single-layered sensor, (b) double-layered sensor, and (c) triple-layered sensor. (d) Experimental results (symbol) and numerical results (solid line) of the electric current for single layered sensors (60 kΩ/sq and 226 Ω/sq, respectively), and double-layered sensor (226 Ω/sq and 60 kΩ/sq). (e) Experimental results (symbol) and numerical results (solid line) of the electric current for single-layered sensors (300 kΩ/sq, 60 kΩ/sq and 226 Ω/sq, respectively), and triple-layered sensor (226 Ω/sq, 60 kΩ/sq, and 300 kΩ/sq). (f) Experimental results (symbol) and numerical results (solid line) of single-layered

sensor (226  $\Omega$ /sq), double-layered sensor (226  $\Omega$ /sq and 60 k $\Omega$ /sq), and triple-layered sensor (226  $\Omega$ /sq, 60 k $\Omega$ /sq, and 300 k $\Omega$ /sq). Here, the higher resistive layer represents the outer layer for multi-layered sensors.

This theoretical and numerical analysis was well-suited for other combinations of multilayers with different resistances (Figure 3.3.24) with actual experimental results, demonstrating the reliability of the proposed sensing mechanism.

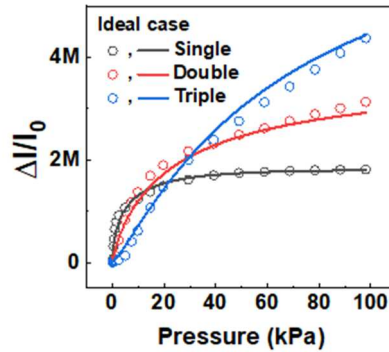


**Figure 3.3.24.** Experimental results (symbol) and numerical results (line) of the ideal model (226  $\Omega$ /sq, 2 k $\Omega$ /sq, and 20 k $\Omega$ /sq); single-layered sensor (226  $\Omega$ /sq), double-layered sensor (226  $\Omega$ /sq and 2 k $\Omega$ /sq), and triple-layered sensor (226  $\Omega$ /sq, 2 k $\Omega$ /sq, and 20 k $\Omega$ /sq). The numerical results of electrical behavior for the double and triple layers were obtained via equations 3.1.3 and 3.1.5.

Likewise, we demonstrated a multi-layered flexible pressure sensor with ultra-high sensitivity and linearity over a broad range of pressure, based on the design of interlocked microdome structures with the conductivity-gradient multilayers on stiffness-gradient interlocked microdomes and coplanar electrodes. The conductivity-gradient multilayers allowed us to control the saturation behavior of resistance change by the gradual activation of current pathway from outer to inner layers and the difference between initial and saturation resistances, thus ensuring the superior linearity and ultra-high sensitivity ( $3.8 \times 10^5 \text{ kPa}^{-1}$ ) for the pressure range of up to 100 kPa. In addition, the human skin-inspired stiffness-gradient interlocked structure exhibited effective stress concentration between the microdomes, enabling highly sensitive and stable functioning of the pressure sensors. Further, the multi-layered pressure sensor exhibited a rapid response time of 0.016 ms and a minimum detectable pressure level of 0.025 Pa. The applicability of the pressure sensors in various applications fields was successfully demonstrated, including sound sensor, weak gas pressure sensor, pressure mapping, and personal healthcare monitoring. We believe that the proposed multi-level gradient electrical and mechanical structures can be readily extended to other electronic material design as a general strategy for the precise regulation of electrical current and mechanical stress transfer. This will in turn usher in the next generation of electronics.

### 3.4 Conclusion

We modeled and demonstrated polymer nanocomposites to fabricate high performance sensor devices using the finite element method (FEM) simulations collaborated with experimental approach. Through a precise modeling in consideration to (particularly) mechanical properties of polymeric materials, we found the most optimized construction of the nanostructured composite materials with highly improved sensing performances (ultrahigh sensitivity, linear sensing capability, and broad sensing range). Finally, we demonstrated highly sensitive triboelectric, ferroelectric, mechanochromic, and piezoresistive sensors with a precise physical (fundamental) sensing mechanism to improve sensing ability through theoretical and numerical analyses.

For triboelectric sensors, the gradient stiffness between stiff epidermis and soft dermis with interlocked microdome structures in human skin induces effective stress transmission to underlying mechanoreceptors for enhanced tactile sensing. Inspired by skin structure and function, we fabricate hierarchical nanoporous and interlocked microdome-structured polymers with gradient stiffness for the spacer-free, ultrathin, and highly-sensitive triboelectric sensors (TESs). The skin-inspired hierarchical polymers with gradient elastic modulus enhance the compressibility and contact areal differences due to effective transmission of the external stress from stiff to soft layers, resulting in highly sensitive TESs capable of detecting human vital signs and voice. In addition, the microdomes in the interlocked polymers provide an effective variation of gap distance between interlocked layers without using the bulk spacer and thus facilitate the ultrathin and flexible design of TESs that could be worn on the body and detect a variety of pressing, bending, and twisting motions even in humid and underwater environments.

For ferroelectric sensors, we demonstrated a flexible ferroelectric sensor with high pressure sensitivity and linear response over an exceptionally broad pressure range. The suggested ferroelectric sensor is based on the rGO/PVDF ferroelectric composites with a multilayer interlocked microdome geometry. The contact area of the interlocked microdome structures rapidly increases from almost zero in the initial unloading state to an extremely high value in the high-pressure loading state, which can be attributed to the concentrated and amplified stress at a small spot between interlocked microdomes that greatly deforms the interlocked microdomes, resulting in the significant increase of the contact area. With increasing number of stacked layers, the contact area dramatically increases due to the increased number of contacted microdomes. The multilayer geometry can enhance the linearity of pressure sensing because the multilayer interlocked microdomes can distribute the applied stress to each stacked layer. As a result, pressure sensitivity and linearity increase with an increase in the number of layers in multilayer e-skins. We also investigated the effect of the rGO loading concentration on the pressure-sensing performances of multilayer e-skins.

For mechanochromic sensors, we demonstrated that a hierarchical NP-MP architecture in porous mechanochromic composites can enhance both mechanochromic strain/stress sensitivity and

stretchability. The experimentally determined structure–activity relationships and computational modelling results suggest the following general design principle: reducing pore size while increasing SNP size should enhance the mechanochromic sensitivity. To demonstrate this design principle, we analyzed the simulated localized stress numerically calculated by finite element simulations. All of the porous structures exhibit 1.6 times higher maximum localized stress, than that exhibited by the planar structure under a strain of 100%, which result matches with the experimental result that depicts a decrease in the critical strain (55%) for the porous structures as compared with the planar one (150%). Furthermore, the porous structure with the smaller pore size possesses a higher PDMS/air interface surface area, which can increase the mechanochromic activation sites of concentrated stress near the interface, resulting in a considerable increase in color contrast, strain sensitivity, and strain sensing range. Based on these results, it is worth noting that the number of activation sites for localized stress around the pore would be crucial for dependence of pore size on mechanochromic sensitivity, rather than maximum localized stress. For the porous mechanochromic composites having SNPs, the greatly reduced critical stress at strain values of 35%, 45%, and 45% corresponds to 0.08–0.14 MPa, which can be attributed to significant enhancement in maximum localized stress by up to 5.7 times near the SNPs. Further, the maximum localized stress near SNPs gradually increases with the size of SNPs, leading to significant reduction of critical stress (35%) for mechanochromic activation and thereby enhancing mechanochromic sensitivity under the same strain.

For piezoresistive sensors, we demonstrated a multi-layered flexible pressure sensor with ultra-high sensitivity and linearity over a broad range of pressure, based on the design of interlocked microdome structures with the conductivity-gradient multilayers on stiffness-gradient interlocked microdomes and coplanar electrodes. The conductivity-gradient multilayers allowed us to control the saturation behavior of resistance change by the gradual activation of current pathway from outer to inner layers and the difference between initial and saturation resistances, thus ensuring the superior linearity and ultra-high sensitivity ( $3.8 \times 10^5 \text{ kPa}^{-1}$ ) for the pressure range of up to 100 kPa. In addition, the human skin-inspired stiffness-gradient interlocked structure exhibited effective stress concentration between the microdomes, enabling highly sensitive and stable functioning of the pressure sensors. Further, the multi-layered pressure sensor exhibited a rapid response time of 0.016 ms and a minimum detectable pressure level of 0.025 Pa. The applicability of the pressure sensors in various applications fields was successfully demonstrated, including sound sensor, weak gas pressure sensor, pressure mapping, and personal healthcare monitoring. We believe that the proposed multi-level gradient electrical and mechanical structures can be readily extended to other electronic material design as a general strategy for the precise regulation of electrical current and mechanical stress transfer. This will in turn usher in the next generation of electronics.

### 3.5 References

1. Takei, K.; Takahashi, T.; Ho, J. C.; Ko, H.; Gillies, A. G.; Leu, P. W.; Fearing, R. S.; Javey, A. Nanowire Active-Matrix Circuitry for Low-Voltage Macroscale Artificial Skin. *Nat. Mater.* **2010**, *9*, 821-826.
2. Park, S.; Kim, H.; Vosgueritchian, M.; Cheon, S.; Kim, H.; Koo, J. H.; Kim, T. R.; Lee, S.; Schwartz, G.; Chang, H.; Bao, Z. A. Stretchable Energy-Harvesting Tactile Electronic Skin Capable of Differentiating Multiple Mechanical Stimuli Modes. *Adv. Mater.* **2014**, *26*, 7324-7332.
3. Shi, M. Y.; Zhang, J. X.; Chen, H. T.; Han, M. D.; Shankaregowda, S. A.; Su, Z. M.; Meng, B.; Cheng, X. L.; Zhang, H. X. Self-Powered Analogue Smart Skin. *ACS Nano* **2016**, *10*, 4083-4091.
4. Wang, C.; Hwang, D.; Yu, Z. B.; Takei, K.; Park, J.; Chen, T.; Ma, B. W.; Javey, A. User-Interactive Electronic Skin for Instantaneous Pressure Visualization. *Nat. Mater.* **2013**, *12*, 899-904.
5. Jeong, J. W.; Yeo, W. H.; Akhtar, A.; Norton, J. J. S.; Kwack, Y. J.; Li, S.; Jung, S. Y.; Su, Y. W.; Lee, W.; Xia, J.; Cheng, H. Y.; Huang, Y. G.; Choi, W. S.; Bretl, T.; Rogers, J. A. Materials and Optimized Designs for Human-Machine Interfaces via Epidermal Electronics. *Adv. Mater.* **2013**, *25*, 6839-6846.
6. Xu, S.; Zhang, Y. H.; Cho, J.; Lee, J.; Huang, X.; Jia, L.; Fan, J. A.; Su, Y. W.; Su, J.; Zhang, H. G.; Cheng, H. Y.; Lu, B. W.; Yu, C. J.; Chuang, C.; Kim, T. I.; Song, T.; Shigeta, K.; Kang, S.; Dagdeviren, C.; Petrov, I.; Braun, P. V.; Huang, Y. G.; Paik, U.; Rogers, J. A. Stretchable Batteries with Self-Similar Serpentine Interconnects and Integrated Wireless Recharging Systems. *Nat. Commun.* **2013**, *4*, 1543.
7. Hwang, B. U.; Lee, J. H.; Trung, T. Q.; Roh, E.; Kim, D. I.; Kim, S. W.; Lee, N. E. Transparent Stretchable Self-Powered Patchable Sensor Platform with Ultrasensitive Recognition of Human Activities. *ACS Nano* **2015**, *9*, 8801-8810.
8. Lee, Y. H.; Kim, J. S.; Noh, J.; Lee, I.; Kim, H. J.; Choi, S.; Seo, J.; Jeon, S.; Kim, T. S.; Lee, J. Y.; Choi, J. W. Wearable Textile Battery Rechargeable by Solar Energy. *Nano Lett.* **2013**, *13*, 5753-5761.
9. Pushparaj, V. L.; Shaijumon, M. M.; Kumar, A.; Murugesan, S.; Ci, L.; Vajtai, R.; Linhardt, R. J.; Nalamasu, O.; Ajayan, P. M. Flexible Energy Storage Devices Based on Nanocomposite Paper. *Proc. Natl. Acad. Sci. U. S. A.* **2007**, *104*, 13574-13577.
10. Xu, S.; Zhang, Y. H.; Jia, L.; Mathewson, K. E.; Jang, K. I.; Kim, J.; Fu, H. R.; Huang, X.; Chava, P.; Wang, R. H.; Bhole, S.; Wang, L. Z.; Na, Y. J.; Guan, Y.; Flavin, M.; Han, Z. S.; Huang, Y. G.; Rogers, J. A. Soft Microfluidic Assemblies of Sensors, Circuits, and Radios for the Skin. *Science* **2014**, *344*, 70-74.

11. Kim, D. H.; Lu, N. S.; Ma, R.; Kim, Y. S.; Kim, R. H.; Wang, S. D.; Wu, J.; Won, S. M.; Tao, H.; Islam, A.; Yu, K. J.; Kim, T. I.; Chowdhury, R.; Ying, M.; Xu, L. Z.; Li, M.; Chung, H. J.; Keum, H.; McCormick, M.; Liu, P.; Zhang, Y. W.; Omenetto, F. G.; Huang, Y. G.; Coleman, T.; Rogers, J. A. Epidermal Electronics. *Science* **2011**, *333*, 838-843.
12. Honda, W.; Harada, S.; Arie, T.; Akita, S.; Takei, K. Wearable, Human-Interactive, Health-Monitoring, Wireless Devices Fabricated by Macroscale Printing Techniques. *Adv. Funct. Mater.* **2014**, *24*, 3299-3304.
13. Scrosati, B. Nanomaterials: Paper Powers Battery Breakthrough. *Nat. Nanotechnol.* **2007**, *2*, 598-599.
14. Wang, Z. L.; Chen, J.; Lin, L. Progress in Triboelectric Nanogenerators as a New Energy Technology and Self-Powered Sensors. *Energy Environ. Sci.* **2015**, *8*, 2250-2282.
15. Wang, Z. L. Self-Powered Nanosensors and Nanosystems. *Adv. Mater.* **2012**, *24*, 280-285.
16. Hu, Y. F.; Lin, L.; Zhang, Y.; Wang, Z. L. Replacing a Battery by a Nanogenerator with 20 V Output. *Adv. Mater.* **2012**, *24*, 110-114.
17. Hansen, B. J.; Liu, Y.; Yang, R. S.; Wang, Z. L. Hybrid Nanogenerator for Concurrently Harvesting Biomechanical and Biochemical Energy. *ACS Nano* **2010**, *4*, 3647-3652.
18. Kim, S. J.; We, J. H.; Cho, B. J. A Wearable Thermoelectric Generator Fabricated on a Glass Fabric. *Energy Environ. Sci.* **2014**, *7*, 1959-1965.
19. Hu, Y. F.; Yang, J.; Niu, S. M.; Wu, W. Z.; Wang, Z. L. Hybridizing Triboelectrification and Electromagnetic Induction Effects for High-Efficient Mechanical Energy Harvesting. *ACS Nano* **2014**, *8*, 7442-7450.
20. Ha, M.; Park, J.; Lee, Y.; Ko, H. Triboelectric Generators and Sensors for Self-Powered Wearable Electronics. *ACS Nano* **2015**, *9*, 3421-3427.
21. Jiang, X.-Z.; Sun, Y.-J.; Fan, Z.; Zhang, T.-Y. Integrated Flexible, Waterproof, Transparent, and Self-Powered Tactile Sensing Panel. *ACS Nano* **2016**, *10*, 7696-7704.
22. Li, T.; Zou, J. D.; Xing, F.; Zhang, M.; Cao, X.; Wang, N.; Wang, Z. L. From Dual-Mode Triboelectric Nanogenerator to Smart Tactile Sensor: A Multiplexing Design. *ACS Nano* **2017**, *11*, 3950-3956.
23. Wang, S. H.; Lin, L.; Wang, Z. L. Nanoscale Triboelectric-Effect-Enabled Energy Conversion for Sustainably Powering Portable Electronics. *Nano Lett.* **2012**, *12*, 6339-6346.
24. Guo, H. Y.; Yeh, M. H.; Zi, Y. L.; Wen, Z.; Chen, J.; Lin, G. L.; Hu, C. G.; Wang, Z. L. Ultralight Cut-Paper-Based Self-Charging Power Unit for Self-Powered Portable Electronic and Medical Systems. *ACS Nano* **2017**, *11*, 4475-4482.
25. Wang, J.; Wu, C. S.; Dai, Y. J.; Zhao, Z. H.; Wang, A.; Zhang, T. J.; Wang, Z. L. Achieving Ultrahigh Triboelectric Charge Density for Efficient Energy Harvesting. *Nat. Commun.* **2017**, *8*, 88.



26. Dharmasena, R.; Jayawardena, K.; Mills, C. A.; Deane, J. H. B.; Anguita, J. V.; Dorey, R. A.; Silva, S. R. P. Triboelectric Nanogenerators: Providing a Fundamental Framework. *Energy Environ. Sci.* **2017**, *10*, 1801-1811.
27. Niu, S. M.; Wang, S. H.; Lin, L.; Liu, Y.; Zhou, Y. S.; Hu, Y. F.; Wang, Z. L. Theoretical Study of Contact-Mode Triboelectric Nanogenerators as an Effective Power Source. *Energy Environ. Sci.* **2013**, *6*, 3576-3583.
28. Yang, J.; Chen, J.; Su, Y. J.; Jing, Q. S.; Li, Z. L.; Yi, F.; Wen, X. N.; Wang, Z. N.; Wang, Z. L. Eardrum-Inspired Active Sensors for Self-Powered Cardiovascular System Characterization and Throat-Attached Anti-Interference Voice Recognition. *Adv. Mater.* **2015**, *27*, 1316-1326.
29. Jing, Q. S.; Xie, Y. N.; Zhu, G.; Han, R. P. S.; Wang, Z. L. Self-Powered Thin-Film Motion Vector Sensor. *Nat. Commun.* **2015**, *6*, 8031.
30. Niu, S. M.; Wang, Z. L. Theoretical Systems of Triboelectric Nanogenerators. *Nano Energy* **2015**, *14*, 161-192.
31. Gu, L.; Cui, N. Y.; Liu, J. M.; Zheng, Y. B.; Bai, S.; Qin, Y. Packaged Triboelectric Nanogenerator with High Endurability for Severe Environments. *Nanoscale* **2015**, *7*, 18049-18053.
32. Lee, K. Y.; Yoon, H. J.; Jiang, T.; Wen, X. N.; Seung, W.; Kim, S. W.; Wang, Z. L. Fully Packaged Self-Powered Triboelectric Pressure Sensor Using Hemispheres-Array. *Adv. Energy Mater.* **2016**, *6*, 1502566.
33. Nguyen, V.; Yang, R. S. Effect of Humidity and Pressure on the Triboelectric Nanogenerator. *Nano Energy* **2013**, *2*, 604-608.
34. Nemeth, E.; Albrecht, V.; Schubert, G.; Simon, F. Polymer Tribo-Electric Charging: Dependence on Thermodynamic Surface Properties and Relative Humidity. *J. Electrostat.* **2003**, *58*, 3-16.
35. Gillespie, P. G.; Walker, R. G. Molecular basis of mechanosensory transduction. *Nature* **2001**, *413*, 194.
36. Delmas, P.; Hao, J.; Rodat-Despoix, L. Molecular mechanisms of mechanotransduction in mammalian sensory neurons. *Nat. Rev. Neurosci.* **2011**, *12*, 139.
37. Hickenboth, C. R.; Moore, J. S.; White, S. R.; Sottos, N. R.; Baudry, J.; Wilson, S. R. Biasing reaction pathways with mechanical force. *Nature* **2007**, *446*, 423.
38. Caruso, M. M.; Davis, D. A.; Shen, Q.; Odom, S. A.; Sottos, N. R.; White, S. R.; Moore, J. S. Mechanically-induced chemical changes in polymeric materials. *Chem. Rev.* **2009**, *109*, 5755-5798.
39. Li, J.; Nagamani, C.; Moore, J. S. Polymer mechanochemistry: from destructive to productive. *Acc. Chem. Res.* **2015**, *48*, 2181-2190.
40. Davis, D. A.; Hamilton, A.; Yang, J.; Cremar, L. D.; Van Gough, D.; Potisek, S. L.; Ong, M. T.; Braun, P. V.; Martínez, T. J.; White, S. R. Force-induced activation of covalent bonds in mechanoresponsive polymeric materials. *Nature* **2009**, *459*, 68.

41. Chen, Y.; Spiering, A.; Karthikeyan, S.; Peters, G. W.; Meijer, E.; Sijbesma, R. P. Mechanically induced chemiluminescence from polymers incorporating a 1, 2-dioxetane unit in the main chain *Nat. Chem.* **2012**, *4*, 559.
42. Piermattei, A.; Karthikeyan, S.; Sijbesma, R. P. Activating catalysts with mechanical force. *Nat. Chem.* **2009**, *1*, 133-137.
43. Diesendruck, C. E.; Steinberg, B. D.; Sugai, N.; Silberstein, M. N.; Sottos, N. R.; White, S. R.; Braun, P. V.; Moore, J. S. Proton-coupled mechanochemical transduction: a mechanogenerated acid. *J. Am. Chem. Soc.* **2012**, *134*, 12446-12449.
44. Lenhardt, J. M.; Ong, M. T.; Choe, R.; Evenhuis, C. R.; Martinez, T. J.; Craig, S. L. Trapping a diradical transition state by mechanochemical polymer extension. *Science*, **2010**, *329*, 1057-1060.
45. Larsen, M. B.; Boydston, A. J. Successive mechanochemical activation and small molecule release in an elastomeric material. *J. Am. Chem. Soc.* **2014**, *136*, 1276-1279.
46. Hong, G.; Zhang, H.; Lin, Y.; Chen, Y.; Xu, Y.; Weng, W.; Xia, H. Mechanoresponsive healable metallosupramolecular polymers. *Macromolecules*, **2013**, *46*, 8649-8656.
47. Lee, C. K.; Davis, D. A.; White, S. R.; Moore, J. S.; Sottos, N. R.; Braun, P. V. Force-induced redistribution of a chemical equilibrium. *J. Am. Chem. Soc.* **2010**, *132*, 16107-16111.
48. Imato, K.; Kanehara, T.; Ohishi, T.; Nishihara, M.; Yajima, H.; Ito, M.; Takahara, A.; Otsuka, H. Mechanochromic dynamic covalent elastomers: quantitative stress evaluation and autonomous recovery. *ACS Macro Lett.* **2015**, *4*, 1307-1311.
49. Chen, H.; Yang, F.; Chen, Q.; Zheng, J. A novel design of multi-mechanoresponsive and mechanically strong hydrogels. *Adv. Mater.* **2017**, *29*, 1606900.
50. Rifaie-Graham, O.; Apebende, E. A.; Bast, L. K.; Bruns, N. Self-reporting fiber-reinforced composites that mimic the ability of biological materials to sense and report damage. *Adv. Mater.* **2018**, *30*, 1705483.
51. Li, Z. a.; Toivola, R.; Ding, F.; Yang, J.; Lai, P. N.; Howie, T.; Georgeson, G.; Jang, S. H.; Li, X.; Flinn, B. D. Highly sensitive built-in strain sensors for polymer composites: Fluorescence turn-on response through mechanochemical activation. *Adv. Mater.* **2016**, *28*, 6592-6597.
52. Kryger, M. J.; Munaretto, A. M.; Moore, J. S. Structure–mechanochemical activity relationships for cyclobutane mechanophores. *J. Am. Chem. Soc.* **2011**, *133*, 18992-18998.
53. Beiermann, B. A.; Kramer, S. L.; May, P. A.; Moore, J. S.; White, S. R.; Sottos, N. R. The effect of polymer chain alignment and relaxation on force-induced chemical reactions in an elastomer. *Adv. Funct. Mater.* **2014**, *24*, 1529-1537.
54. Beiermann, B. A.; Davis, D. A.; Kramer, S. L.; Moore, J. S.; Sottos, N. R.; White, S. R. Environmental effects on mechanochemical activation of spiropyran in linear PMMA. *J. Mater. Chem.* **2011**, *21*, 8443-8447.

55. Chen, Y.; Zhang, H.; Fang, X.; Lin, Y.; Xu, Y.; Weng, W. Mechanical activation of mechanophore enhanced by strong hydrogen bonding interactions. *ACS Macro Lett.* **2014**, *3*, 141-145.
56. Jiang, S.; Zhang, L.; Xie, T.; Lin, Y.; Zhang, H.; Xu, Y.; Weng, W.; Dai, L. Mechanoresponsive PS-PnBA-PS triblock copolymers via covalently embedding mechanophore. *ACS Macro Lett.* **2013**, *2*, 705-709.
57. Yan, H.; Yang, F.; Pan, D.; Lin, Y.; Hohman, J. N.; Solis-Ibarra, D.; Li, F. H.; Dahl, J. E.; Carlson R. M.; Tkachenko, B. A. Sterically controlled mechanochemistry under hydrostatic pressure. *Nature* **2018**, *554*, 505.
58. Zhang, H.; Chen, Y.; Lin, Y.; Fang, X.; Xu, Y.; Ruan, Y.; Weng, W. Spiropyran as a mechanochromic probe in dual cross-linked elastomers. *Macromolecules* **2014**, *47*, 6783-6790.
59. Gossweiler, G. R.; Hewage, G. B.; Soriano, G.; Wang, Q.; Welshofer, G. W.; Zhao, X.; Craig, S. L. Mechanochemical activation of covalent bonds in polymers with full and repeatable macroscopic shape recovery. *ACS Macro Lett.* **2014**, *3*, 216-219.
60. Filonenko, G. A.; Lugger, J. A.; Liu, C.; van Heeswijk, E. P.; Hendrix, M. M.; Weber, M.; Müller, C.; Hensen, E. J.; Sijbesma, R. P.; Pidko, E. A. Tracking Local Mechanical Impact in Heterogeneous Polymers with Direct Optical Imaging. *Angew. Chem.* **2018**, *130*, 16623-16628.
61. Sagara, Y.; Karman, M.; Verde-Sesto, E.; Matsuo, K.; Kim, Y.; Tamaoki, N.; Weder, C. Rotaxanes as mechanochromic fluorescent force transducers in polymers. *J. Am. Chem. Soc.* **2018**, *140*, 1584-1587.
62. Park, J.; Kim, M.; Lee, Y.; Lee, H. S.; Ko, H. Fingertip skin-inspired microstructured ferroelectric skins discriminate static/dynamic pressure and temperature stimuli. *Sci. Adv.* **2015**, *1*, e1500661.
63. Lee, Y.; Park, J.; Cho, S.; Shin, Y. E.; Lee, H.; Kim, J.; Myoung, J.; Cho, S.; Kang, S.; Baig, C.; Ko, H. Flexible Ferroelectric Sensors with Ultrahigh Pressure Sensitivity and Linear Response over Exceptionally Broad Pressure Range. *ACS Nano* **2018**, *12*, 4045-4054.
64. Ha, M.; Lim, S.; Cho, S.; Lee, Y.; Na, S.; Baig, C.; Ko, H. Skin-inspired hierarchical polymer architectures with gradient stiffness for spacer-free, ultrathin, and highly sensitive triboelectric sensors. *ACS Nano* **2018**, *12*, 3964-3974.
65. Park, J.; Lee, Y.; Ha, M.; Cho, S.; Ko, H., Micro/Nanostructured Surfaces for Self-Powered and Multifunctional Electronic Skins. *J. Mater. Chem. B* **2016**, *4*, 2999-3018.
66. Hua, Q.; Sun, J.; Liu, H.; Bao, R.; Yu, R.; Zhai, J.; Pan, C.; Wang, Z. L., Skin-Inspired Highly Stretchable and Conformable Matrix Networks for Multifunctional Sensing. *Nat. Commun.* **2018**, *9*, 1-11.
67. Rus, D.; Tolley, M. T., Design, Fabrication and Control of Soft Robots. *Nature* **2015**, *521*, 467-475.

68. Larson, C.; Peele, B.; Li, S.; Robinson, S.; Totaro, M.; Beccai, L.; Mazzolai, B.; Shepherd, R., Highly Stretchable Electroluminescent Skin for Optical Signaling and Tactile Sensing. *Science* **2016**, *351*, 1071-1074.
69. Ge, J.; Wang, X.; Drack, M.; Volkov, O.; Liang, M.; Bermúdez, G. S. C.; Illing, R.; Wang, C.; Zhou, S.; Fassbender, J., A Bimodal Soft Electronic Skin for Tactile and Touchless Interaction in Real Time. *Nat. Commun.* **2019**, *10*, 1-10.
70. Lee, W. W.; Tan, Y. J.; Yao, H.; Li, S.; See, H. H.; Hon, M.; Ng, K. A.; Xiong, B.; Ho, J. S.; Tee, B. C., A Neuro-Inspired Artificial Peripheral Nervous System for Scalable Electronic Skins. *Sci. Robotic.* **2019**, *4*, eaax2198.
71. Koo, J. H.; Jeong, S.; Shim, H. J.; Son, D.; Kim, J.; Kim, D. C.; Choi, S.; Hong, J.-I.; Kim, D.-H., Wearable Electrocardiogram Monitor Using Carbon Nanotube Electronics and Color-Tunable Organic Light-Emitting Diodes. *ACS Nano* **2017**, *11*, 10032-10041.
72. Lee, Y.; Park, J.; Choe, A.; Cho, S.; Kim, J.; Ko, H., Mimicking Human and Biological Skins for Multifunctional Skin Electronics. *Adv. Funct. Mater.* **2020**, *30*, 1904523.
73. Kim, J.; Lee, M.; Shim, H. J.; Ghaffari, R.; Cho, H. R.; Son, D.; Jung, Y. H.; Soh, M.; Choi, C.; Jung, S., Stretchable Silicon Nanoribbon Electronics for Skin Prosthesis. *Nat. Commun.* **2014**, *5*, 1-11.
74. Trung, T. Q.; Ramasundaram, S.; Hwang, B. U.; Lee, N. E., An All-Elastomeric Transparent and Stretchable Temperature Sensor for Body-Attachable Wearable Electronics. *Adv. Mater.* **2016**, *28*, 502-509.
75. Park, J.; Kim, M.; Lee, Y.; Lee, H. S.; Ko, H., Fingertip Skin-Inspired Microstructured Ferroelectric Skins Discriminate Static/Dynamic Pressure and Temperature Stimuli. *Sci. Adv.* **2015**, *1*, e1500661.
76. Wu, Z.; Ding, W.; Dai, Y.; Dong, K.; Wu, C.; Zhang, L.; Lin, Z.; Cheng, J.; Wang, Z. L., Self-Powered Multifunctional Motion Sensor Enabled by Magnetic-Regulated Triboelectric Nanogenerator. *ACS Nano* **2018**, *12*, 5726-5733.
77. Nie, B.; Li, R.; Cao, J.; Brandt, J. D.; Pan, T., Flexible Transparent Iontronic Film for Interfacial Capacitive Pressure Sensing. *Adv. Mater.* **2015**, *27*, 6055-6062.
78. Park, J.; Lee, Y.; Hong, J.; Lee, Y.; Ha, M.; Jung, Y.; Lim, H.; Kim, S. Y.; Ko, H., Tactile-Direction-Sensitive and Stretchable Electronic Skins Based on Human-Skin-Inspired Interlocked Microstructures. *ACS Nano* **2014**, *8*, 12020-12029.
79. Wang, X.; Dong, L.; Zhang, H.; Yu, R.; Pan, C.; Wang, Z. L., Recent Progress in Electronic Skin. *Adv. Sci.* **2015**, *2*, 1500169.
80. Lin, Y.; Chen, J.; Tavakoli, M. M.; Gao, Y.; Zhu, Y.; Zhang, D.; Kam, M.; He, Z.; Fan, Z., Printable Fabrication of a Fully Integrated and Self-Powered Sensor System on Plastic Substrates. *Adv. Mater.* **2019**, *31*, 1804285.

81. Park, J.; Lee, Y.; Hong, J.; Ha, M.; Jung, Y.-D.; Lim, H.; Kim, S. Y.; Ko, H., Giant Tunneling Piezoresistance of Composite Elastomers with Interlocked Microdome Arrays for Ultrasensitive and Multimodal Electronic Skins. *ACS Nano* **2014**, *8*, 4689-4697.
82. Park, J.; Kim, J.; Hong, J.; Lee, H.; Lee, Y.; Cho, S.; Kim, S.-W.; Kim, J. J.; Kim, S. Y.; Ko, H., Tailoring Force Sensitivity and Selectivity by Microstructure Engineering of Multidirectional Electronic Skins. *NPG Asia Mater.* **2018**, *10*, 163-176.
83. Jung, S.; Kim, J. H.; Kim, J.; Choi, S.; Lee, J.; Park, I.; Hyeon, T.; Kim, D. H., Reverse-Micelle-Induced Porous Pressure-Sensitive Rubber for Wearable Human–Machine Interfaces. *Adv. Mater.* **2014**, *26*, 4825-4830.
84. Lee, D.; Lee, H.; Jeong, Y.; Ahn, Y.; Nam, G.; Lee, Y., Highly Sensitive, Transparent, and Durable Pressure Sensors Based on Sea-Urchin Shaped Metal Nanoparticles. *Adv. Mater.* **2016**, *28*, 9364-9369.
85. Jang, K.-I.; Han, S. Y.; Xu, S.; Mathewson, K. E.; Zhang, Y.; Jeong, J.-W.; Kim, G.-T.; Webb, R. C.; Lee, J. W.; Dawidczyk, T. J., Rugged and Breathable Forms of Stretchable Electronics with Adherent Composite Substrates for Transcutaneous Monitoring. *Nat. Commun.* **2014**, *5*, 1-10.
86. Boutry, C. M.; Negre, M.; Jorda, M.; Vardoulis, O.; Chortos, A.; Khatib, O.; Bao, Z., A Hierarchically Patterned, Bioinspired E-Skin Able to Detect the Direction of Applied Pressure for Robotics. *Sci. Robotic.* **2018**, *3*, eaau6914.
87. Shuai, X.; Zhu, P.; Zeng, W.; Hu, Y.; Liang, X.; Zhang, Y.; Sun, R.; Wong, C.-p., Highly Sensitive Flexible Pressure Sensor Based on Silver Nanowires-Embedded Polydimethylsiloxane Electrode with Microarray Structure. *ACS Appl. Mater. Interfaces* **2017**, *9*, 26314-26324.
88. Choong, C. L.; Shim, M. B.; Lee, B. S.; Jeon, S.; Ko, D. S.; Kang, T. H.; Bae, J.; Lee, S. H.; Byun, K. E.; Im, J., Highly Stretchable Resistive Pressure Sensors Using a Conductive Elastomeric Composite on a Micropyramid Array. *Adv. Mater.* **2014**, *26*, 3451-3458.
89. Guo, Y.; Guo, Z.; Zhong, M.; Wan, P.; Zhang, W.; Zhang, L., A Flexible Wearable Pressure Sensor with Bioinspired Microcrack and Interlocking for Full-Range Human–Machine Interfacing. *Small* **2018**, *14*, 1803018.
90. Pu, J.-H.; Zha, X.-J.; Tang, L.-S.; Bai, L.; Bao, R.-Y.; Liu, Z.-Y.; Yang, M.-B.; Yang, W., Human Skin-Inspired Electronic Sensor Skin with Electromagnetic Interference Shielding for the Sensation and Protection of Wearable Electronics. *ACS Appl. Mater. Interfaces* **2018**, *10*, 40880-40889.
91. Li, H.; Wu, K.; Xu, Z.; Wang, Z.; Meng, Y.; Li, L., Ultrahigh-Sensitivity Piezoresistive Pressure Sensors for Detection of Tiny Pressure. *ACS Appl. Mater. Interfaces* **2018**, *10*, 20826-20834.
92. Gong, S.; Schwalb, W.; Wang, Y.; Chen, Y.; Tang, Y.; Si, J.; Shirinzadeh, B.; Cheng, W., A Wearable and Highly Sensitive Pressure Sensor with Ultrathin Gold Nanowires. *Nat. Commun.* **2014**, *5*, 1-8.

93. Liu, W.; Liu, N.; Yue, Y.; Rao, J.; Luo, C.; Zhang, H.; Yang, C.; Su, J.; Liu, Z.; Gao, Y., A Flexible and Highly Sensitive Pressure Sensor Based on Elastic Carbon Foam. *J. Mater. Chem. C* **2018**, *6*, 1451-1458.
94. Bae, G. Y.; Pak, S. W.; Kim, D.; Lee, G.; Kim, D. H.; Chung, Y.; Cho, K., Linearly and Gighly Pressure-Sensitive Electronic Skin Based on a Bioinspired Hierarchical Structural Array. *Adv. Mater.* **2016**, *28*, 5300-5306.
95. Luo, N.; Huang, Y.; Liu, J.; Chen, S. C.; Wong, C. P.; Zhao, N., Hollow-Structured Graphene–Silicone-Composite-Based Piezoresistive Sensors: Decoupled Property Tuning and Bending Reliability. *Adv. Mater.* **2017**, *29*, 1702675.
96. Lee, Y.; Park, J.; Cho, S.; Shin, Y.-E.; Lee, H.; Kim, J.; Myoung, J.; Cho, S.; Kang, S.; Baig, C., Flexible Ferroelectric Sensors with Ultrahigh Pressure Sensitivity and Linear Response over Exceptionally Broad Pressure Range. *ACS Nano* **2018**, *12*, 4045-4054.

## IV. Summary

Here, we first present comprehensive analysis on the shear rheology of polymers for various molecular architectures (linear, ring, and short-chain branched) in the bulk and confined systems using atomistic NEMD simulations. In comparison to bulk polymeric system, the interfacial chain dynamics near the boundary solid walls in the confined system are interesting. Detailed molecular-level analysis of the individual chain motions for various molecular architectures are carried out to characterize the intrinsic molecular mechanisms for interfacial chains in three characteristic flow regimes (weak, intermediate, and strong) regarding to the interfacial slip behavior (i.e., degree of slip).

Through a comprehensive analysis using the atomistic NEMD simulations, the nonlinear rheological properties for linear PE melts (reflecting substantial deformation of polymer chains under intermediate-to-strong flow fields) were closely examined with respect to the following molecular characteristics: (i) chain orientation, (ii) stretching, (iii) disentanglement, (iv) intermolecular collision, and (v) end-over-end tumbling dynamics. Here, properties (i)–(iii) conform to the well-known polymer kinetic theory.<sup>1,2</sup> Through a detailed analysis of the variations in the molecular characteristics in response to the applied shear rate, we propose scaling expressions for the shear viscosity  $\eta$  and the first normal stress coefficient  $\Psi_1$  for unentangled and entangled linear PE systems with respect to those molecular variables. Comparing the  $Wi$  dependence of the structural parameters (defined for the whole chain backbone and/or entanglement strand) and rheological properties, we examine the scaling of those properties with respect to the structural parameters. Specifically, in the intermediate flow regime, we find scaling relationships for the viscosity  $\eta$  and the first normal stress difference  $\Psi_1$  with respect to the well-known fundamental molecular characteristics in polymer rheology such as the chain orientation, chain stretch, and interchain entanglement: (i)  $\eta \sim \theta^{\alpha_1} R^2$  and  $\Psi_1 \sim \theta^{\alpha_2} R^2$  with  $\alpha_1 = (1.5\text{--}1.7)$  and  $\alpha_2 = (3.2\text{--}3.6)$  for unentangled melts and (ii)  $\eta \sim \theta_{\text{es}}^{\alpha_1} Z^{\gamma_1} d_{\text{es}}^2$  and  $\Psi_1 \sim \theta_{\text{es}}^{\alpha_2} Z^{\gamma_2} d_{\text{es}}^2$  with  $\gamma_1 = (3.8\text{--}4.0)$  and  $\gamma_2 = (2.1\text{--}2.4)$  for entangled melts. Here,  $\theta$  ( $\theta_{\text{es}}$ ),  $R$ ,  $Z$ , and  $d_{\text{es}}$  are the average chain orientation angle (that of entanglement strand), the mean chain end-to-end distance, the average number of interchain entanglements, and the average length of an entanglement strand, respectively. While the C<sub>400</sub> and C<sub>600</sub> PE melts employed in this study are rather short and only mildly entangled systems, we believe that the basic features of the scaling expressions deduced for those chains remain valid for longer, strongly entangled chains within statistical uncertainties. Nevertheless, considering the rheological influence of entanglement segments near the chain ends (e.g., the effect of the contour length fluctuations in the tube theory<sup>1</sup>), which is particularly important for rather weakly entangled melt systems, the scaling exponent for the  $Z$ -dependence reported here may change slightly and approach gradually an asymptotic value as the chain length increases to highly entangled polymer melts. Furthermore, our proposed scaling relationships may be adapted to entangled branched polymers with additional scaling component of the

arm orientation and stretch at the junction points along the chain backbone whose scaling behavior is to be the same as that of entangled linear polymers. Under moderately strong flow, those relationships may serve as a supplement (or substitute) for SOR which has a rigid molecular basis under slow flow. In the strong flow regime, the above scaling expressions become invalid and another empirical rheological scaling is found in terms of the characteristic rotational time  $\tau_{\text{rot}}$  as the representative dynamic variable to accommodate intermolecular collisional effects: (iii)  $\eta \sim \tau_{\text{rot}}^{\delta_1}$  and  $\Psi_1 \sim \tau_{\text{rot}}^{\delta_2}$  with  $\delta_1 = (0.5-0.6)$  and  $\delta_2 = (1.8-2.0)$  for both unentangled and entangled systems. The proposed scaling relationships in this study well described  $\eta$  and  $\Psi_1$  obtained from the NEMD simulations under intermediate flow, thereby allowing us to correlate  $\eta$  and  $\Psi_1$  with the molecular variables ( $\theta$ ,  $R$ ,  $Z$ , and  $d_{\text{es}}$ ), in particular the scalar orientational variable  $\theta$  in the experimental sense (of correlating rheological and structural data) explained earlier. Thus, those relationships are believed to serve as a supplement (or substitute) for the modified SOR under the intermediate flow.

Additionally, we carried out a comprehensive study on the intrinsic structural characteristics of ring polymers under shear flow with both dilute and melt conditions. Our analysis began with the advanced viewpoint that ring polymers intrinsically possess two-dimensional surface characteristics because of their closed-loop geometry, which is in contrast with the one-dimensional line characteristics of linear polymers. Based on this view, we introduced several representative physical measures that could effectively describe the structural and dynamical characteristics of ring polymers, such as the total and projected surface areas and the average normal vector  $\mathbf{n}_{\text{avg}}$  of the ring surface, which corresponds with the chain end-to-end vector  $\mathbf{R}_{\text{ete}}$  of a linear polymer. Knowing the variation of these surface measures in response to the applied flow was found to be very informative for analyzing the characteristic molecular dynamics mechanisms of ring chains. An efficient numerical scheme was also developed that allowed us to effectively describe the complex curved surface formed by flexible ring chains. Applying this algorithm, we could accurately measure the overall surface shape and total or projected areas. The obtained surface information was found to be very useful for analyzing the characteristic dynamic mechanisms of ring polymers under shear flow. This scheme can be further applied to extract the intrinsic geometrical characteristics for various ring-type polymers (e.g., tadpole-like polymers) and ring/linear blend systems. Furthermore, the numerical algorithm can be used to directly quantify the degree of penetration between different ring chains, thereby enabling a systematic analysis of the dynamical role of interchain penetration for ring melt systems; this has been an important (and rather controversial) rheological issue in the last decades.

Finally, we performed a comprehensive analysis of the interfacial structural and dynamical behavior of confined polymer melt systems possessing various molecular architectures (linear, ring, SCB linear, and SCB ring) under shear flow using atomistic NEMD simulations. We placed a particular



focus on the combined rheological influence of the closed-loop ring geometry and short-chain branching on the general structure and dynamics of the interfacial chains. In doing so, we examined the degree of interfacial slip, the underlying characteristic molecular mechanisms, and the detailed chain conformations for interfacial chains with respect to their molecular architectures. In general, the interfacial linear and ring polymers exhibit three distinct characteristic regimes for the degree of slip ( $d_s$ ) with respect to the applied shear rate: an increasing, decreasing, and increasing behavior of  $d_s$  in the weak, intermediate, and strong flow regimes, respectively. In contrast, the interfacial SCB linear and SCB ring polymers display almost constant behavior of  $d_s$  throughout the weak and intermediate flow regimes followed by rapidly increasing behavior of  $d_s$  in the strong flow regime. To elucidate the interfacial slip behavior, it is very informative to analyze the fundamental molecular mechanisms with respect to the three representative (weak, intermediate, and strong) flow regimes. In the weak flow regime, all of the interfacial polymers (linear, ring, SCB linear, and SCB ring) undergo  $z$ -to- $x$  chain rotation from the neutral direction to the flow direction, which effectively reduces the dynamic wall friction against chain movement along the flow direction. However, in comparison with its linear analogue, the ring polymer possesses a relatively longer chain dimension in the neutral direction owing to its intrinsic closed-loop geometry, which enhances the dynamic friction of the interfacial ring chains moving against the wall in the flow direction. In the case of the interfacial SCB polymers, whereas the main chain backbone becomes gradually aligned to the flow direction with increasing flow strength (thus decreasing the dynamic wall friction), the short branches tend to be oriented more perpendicular (i.e., aligned in the neutral direction) than parallel to the backbone (thus increasing the dynamic wall friction) in conjunction with their intrinsically fast random motions that are practically unaffected by the imposed flow fields. These two contrasting factors cancel each other out to result in almost constant in the weak flow regime for the interfacial SCB polymers. Furthermore, owing to its relatively larger chain dimension in the neutral direction associated with the ring topology, the SCB ring polymer exhibits the lowest degree of slip among all of the polymers. In respect to the overall chain dimension, the closed-loop ring topology tends to enhance  $G_{zz}$  but diminish both  $G_{xx}$  and  $G_{yy}$ , while short-chain branching tends to enhance both  $G_{yy}$  and  $G_{zz}$  but diminish  $G_{xx}$ .

Based on fundamental studies for polymers, we additionally modeled and designed polymer nanocomposites to fabricate versatile sensor devices using FEM simulations collaborated with experimental approach. Through a precise modeling in consideration to (particularly) mechanical properties, we found the most optimized construction of the nanostructured composite materials with highly improved sensing performances (ultrahigh sensitivity, linear sensing capability, and broad sensing range). Finally, we demonstrated highly sensitive triboelectric, ferroelectric, mechanochromic, and piezoresistive sensors with precise physical (fundamental) mechanism to improve sensing ability.

## Acknowledgements

I appreciate to all supports and encouragements that I received during my Ph. D. program.

박사 학위 과정 동안 받은 많은 도움과 격려에 진심으로 감사드립니다.

우선, 박사 학위 과정 동안 좋은 연구를 많이 할 수 있게 지도해주신 백충기 지도교수님께 감사합니다. 연구실 인턴 시절때부터 관서 수업을 통해 연구에 필요한 기초 배경지식을 터득하는데 많은 도움을 주셨으며, 이를 바탕으로 박사 학위 동안 기초 및 응용과학에 대한 연구를 성공적으로 수행할 수 있었습니다. 또한, 실험 연구실과의 공동 연구를 성공적으로 수행할 수 있게 지도해주신 고헌협 교수님께 감사합니다. 늘 저의 연구에 열정적으로 관심을 가져 주시고, 다양한 관점에서 생각할 수 있게 도와주신 김소연 교수님께 감사합니다. 저의 박사 학위 심사에 흔쾌히 응해주시고, 좋은 연구자로서 앞으로 나아갈 방향에 대한 많은 조언을 해주신 이지석 교수님께 감사합니다. 많은 공동 연구를 함께 고민해주시고, 인생에 대한 많은 조언 및 격려를 해주신 김준모 교수님께 감사합니다. 박사 학위 과정 동안 받은 많은 조언과 격려를 바탕으로, 앞으로도 더 좋은 연구를 많이 할 수 있도록 노력하겠습니다. 다시 한번 더 감사합니다.

함께 연구실 생활을 하며 서로에게 힘이 되어 주었던 이태희 박사님, 정소담 박사님, 윤정하 박사님, 노은정 박사님, 하미란 박사님, 정승흠 박사님, 김진성 박사님, 강욱중 박사님, 하태용 학생에게 감사합니다. 실험과 시뮬레이션 간의 공동 연구를 성공적으로 함께 수행한 박종화 박사님, 이영오 박사님, 하민정 박사님께도 감사를 전하고 싶습니다. 이승진 박사님, 이태경 박사님, 오종원 박사님, 오세혁 박사님의 도움에도 감사합니다.

대학 시절때부터 동고동락하며 기쁠 때나 슬플 때나 함께한 김신, 박민우, 정해동, 박내현, 우민수, 윤기훈, 김대왕, 김태우, 김준한, 임동천, 오종원, 변성준, 박범수, 김익현, 최종관, 김남익, 한태호, 강성호, 이상정, 임근택에게 감사합니다. 또한, 20 년지기 고향 친구들인 이원준, 이동규, 남정수, 이익래, 황창희에게도 감사의 인사를 전하고 싶습니다.

마지막으로, 박사 과정을 성공적으로 마칠 수 있게 물심양면으로 도와주시고 든든한 기둥이 되어주신 사랑하는 부모님, 형에게 감사합니다. 또한, 항상 좋은 말씀과 격려를 해주신 할아버지, 외할머니, 외할아버지께 감사하며, 하늘에 계신 할머니께도 이 소식이 전달되길 바랍니다. 많은 분들이 베풀어 주신 은혜에 다시 한번 더 깊이 감사드립니다.

## List of Publications

1. Lee, Y.<sup>†</sup>; Myoung, J.<sup>†</sup>; **Cho, S.<sup>†</sup>**; Park, J.; Kim, J.; Lee, H.; Lee, Y.; Lee, S.; Baig, C.\*; Ko, H.\*  
Bioinspired Gradient Conductivity and Stiffness for Ultrasensitive Electronic Skins. *ACS Nano* **2021**, *15*, 1795-1804.
2. Jeong, S. H.<sup>†</sup>; **Cho, S.<sup>†</sup>**; Ha, T. Y.; Roh, E. J.; Baig, C.\* Structural and Dynamical Characteristics of Short-Chain Branched Ring Polymer Melts at Interface under Shear Flow. *Polymers* **2020**, *12*, 3068.
3. Jeong, S. H.<sup>†</sup>; **Cho, S.<sup>†</sup>**; Roh, E. J.<sup>†</sup>; Ha, T. Y.<sup>†</sup>; Kim, J. M.<sup>†</sup>; Baig, C.\* Intrinsic Surface Characteristics and Dynamic Mechanisms of Ring Polymers in Solution and Melt under Shear Flow. *Macromolecules* **2020**, *53*, 10051-10060.
4. **Cho, S.<sup>†</sup>**; Kim, J. M.<sup>†</sup>; Baig, C.\* Scaling Characteristics of Rotational Dynamics and Rheology of Linear Polymer Melts in Shear Flow. *Macromolecules* **2020**, *53*, 3030-3041.
5. Park, J.<sup>†</sup>; Lee, Y.<sup>†</sup>; Barbee, M. H.<sup>†</sup>; **Cho, S.<sup>†</sup>**; Cho, S.; Shanker, R.; Kim, J.; Myoung, J.; Kim, M. P.; Baig, C.\*; Craig, S. L.\*; Ko, H.\* A Hierarchical Nanoparticle-in-Micropore Architecture for Enhanced Mechanosensitivity and Stretchability in Mechanochromic Electronic Skins. *Advanced Materials* **2019**, *31*, 1808148.
6. Jeong, S.; **Cho, S.**; Kim, J. M.; Baig, C.\* Interfacial Molecular Structure and Dynamics of Confined Ring Polymer Melts under Shear Flow. *Macromolecules* **2018**, *51*, 4670-4677.
7. Lee, Y.; Park, J.; **Cho, S.**; Shin, Y.-E.; Lee, H.; Kim, J.; Myoung, J.; Cho, S.; Kang, S.; Baig, C.; Ko, H.\* Flexible Ferroelectric Sensors with Ultrahigh Pressure Sensitivity and Linear Response over Exceptionally Broad Pressure Range. *ACS Nano* **2018**, *12*, 4045-4054.
8. Ha, M.<sup>†</sup>; Lim, S.<sup>†</sup>; **Cho, S.<sup>†</sup>**; Lee, Y.; Na, S.; Baig, C.\*; Ko, H.\* Skin-Inspired Hierarchical Polymer Architectures with Gradient Stiffness for Spacer-Free, Ultrathin, and Highly Sensitive Triboelectric Sensors. *ACS Nano* **2018**, *12*, 3964-3974.
9. Jeong, S. H.<sup>†</sup>; Kim, J. M.<sup>†</sup>; **Cho, S.**; Baig, C.\* Effect of short-chain branching on interfacial polymer structure and dynamics under shear flow. *Soft Matter* **2017**, *13*, 8644-8650.
10. **Cho, S.**; Jeong, S.; Kim, J. M.\*; Baig, C.\* Molecular dynamics for linear polymer melts in bulk and confined systems under shear flow. *Scientific Reports* **2017**, 9004.
11. Jeong, S.; **Cho, S.**; Kim, J. M.; Baig, C.\* Molecular mechanisms of interfacial slip for polymer melts under shear flow. *Journal of Rheology* **2017**, *61*, 253-264.